Low-dimensional silicon-germanium heterostructures for quantum spintronics

Raisei Mizokuchi

Communauté
UNIVERSITÉ Grenoble Alpes

THÈSE

Pour obtenir le grade de

DOCTEUR DE LA COMMUNAUTÉ UNIVERSITÉ GRENOBLE ALPES

Spécialité : NANOPHYSIQUE

Arrêté ministériel : 25 mai 2016

Présentée par

Raisei MIZOKUCHI

Thèse dirigée par **Silvano DE FRANCESCHI**, CEA

préparée au sein du **Laboratoire PHotonique, ELectronique et Ingéniérie QuantiqueS**
dans **l'École Doctorale Physique**

Hétérostructures de silicium-germanium à dimensionnalité réduite pour la spintronique quantique

Low-dimensional silicon-germanium heterostructures for quantum spintronics

Thèse soutenue publiquement le **5 juin 2018**,
devant le jury composé de :

Madame JULIA MEYER
PROFESSEUR, UNIVERSITE GRENOBLE ALPES, Examinateur
Monsieur MAKSYM MYRONOV
PROFESSEUR ASSOCIE, UNIVERSITE DE WARWICK - GRANDE BRETAGNE, Examinateur
Monsieur FERDINAND KUEMMETH
PROFESSEUR ASSOCIE, UNIVERSITE DE COPENHAGUE - DANEMARK, Rapporteur
Monsieur FLORIS ZWANENBURG
PROFESSEUR ASSOCIE, UNIVERSITE DE TWENTE - PAYS-BAS, Rapporteur
Monsieur CHRISTOPHER BÄUERLE
DIRECTEUR DE RECHERCHE, CNRS DELEGATION ALPES, Président

Acknowledgements

First of all, I would like to thank Silvano De Franceschi for supervising my PhD thesis. He always guided me to the correct direction by providing ideas for device fabrication, device structures and measurements. I am grateful also for his patience and for his help to improve my communication skills.

I would like to thank Romain Maurand as well. He taught me new things on sample fabrication which I did not know from my previous experience during my bachelor and master researches in Japan. The device fabrication techniques I used could not be developed without his help. Moreover, he taught me measurement methods, cryogenic techniques, file management, and many useful tricks.

I would like to thank Maksym Myronov for providing Ge/SiGe heterostructures and for useful discussions.

Throughout my PhD I received valuable help from Jean-Luc Thomassin, Frederic Gustavo, Thomas Charvolin, Marlene Terrier, Christophe Lemonias and other technical staff at the PTA cleanroom, where I spent a considerable part of my research efforts. I am especially grateful to Jean-Luc who taught me how to use a lot of equipement in the cleanroom.

I want to thank some the theorists at INAC with whom I've had enlightening discussions: Yann-Michel Niquet, Zaiping Zeng, and Julia Meyer.

I would like to thank Simon Deleonibus and Shunri Oda for their guidance. Without their advice, I would have not considered doing a PhD in France and I would have missed the opportunity to work on this valuable project. And I thank Jérôme Planes for following my developments, providing constant support and advice.

I feel grateful to all the colleagues from the lab for creating an enjoyable research environment and helping me whenever I needed (especially Juan-Carlos Estrada Saldaña, Heorhii Bohuslavskyi, Patrick Torresani, Dante Colao Zanuz, Florian Vigneau, Alessandro Crippa, Jean-Pierre Cleuziou, Eduardo Lee, Marc Sanquer, Georg Knebel, Daniel Braithwaite, Iulian Matei, Dai Aoki, Shingo Araki, Christophe Marcenat, François Lefloch,

Xavier Jehl, Jean-Pascal Brison, and Max Hofheinz)

Last but not least, I thank my family for supporting me during the years.

Résumé

L'intégration à large échelles de bits quantiques (qubits) nécessite le développpement de systèmes quantiques à deux niveaux à l'état solide comme par example des spins électroniques confinés dans des boîtes quantiques ou des fermions de Majorana dans des nanofils semiconducteurs. Les trous confinés à une ou deux dimensions dans des hétérostructures à base de germanium sont de bons candidats pour de tels qubits parce qu'ils offrent i) une forte interaction spin-orbite (SOI) conduisant à des facteurs de Landé relativement grands, ii) un couplage hyperfin réduit laissant entrevoir un long de temps de cohérence de spin et iii) des masses efficaces relativement faibles favorisant le confinement quantique. Au cours de cette thèse, j'ai étudié le transport de trous dans des systèmes unidimensionnels et bidimensionnels faits à partir d'hétérostructures $Ge/Si_{0.2}Ge_{0.8}$ à contrainte compressive. Une partie importante de mon travail de recherche a été consacrée au développement de techniques de fabrication pour ces dispositifs semi-conducteurs. J'ai débuté par la fabrication de dispositifs de type "barre de Hall" à partir d'hétérostructures Ge/SiGe non dopées. J'ai étudié deux types d'hétérostructures contenants un puits quantique de Ge contraint: l'une où le puits de Ge est à la surface de la structure donc facilement accessible aux contacts métalliques, et l'autre où le puits est enterré à 70 nm sous la surface permettant d'avoir une mobilité élevée. Les propriétés électroniques du gaz de trou bidimensionnel confiné dans le puits de Ge ont été étudiées à travers des mesures de magnéto-transport jusqu'à 0,3 K. Pour le puits enterré, mes mesures ont révélé un caractère dominant de trou lourd, ce qui est attendu dans le cas d'une contrainte compressive en combinaison avec un confinement bidimensionnel. Les dispositifs avec un puits de Ge superficiel ont montré un transport diffusif et un effet d'anti-localisation faible, ce qui est dû à l'interférence quantique de differents chemins de diffusion en présence du SOI. Le fait que le puits de Ge soit situé à la surface permet des champs électriques perpendiculaires relativement grands et, par conséquent, un plus fort SOI de type Rashba. J'ai été en mesure d'estimer l'énergie caractéristique du SOI en obtenant

une valeur d'environ 1 meV. Pour la réalisation de nano-dispositifs quantiques, j'ai utilisé des hétérostructures avec un puits de Ge enterré où la mobilité des trous se rapproche de 2×10^5 cm^2/Vs. En utilisant la lithographie par faisceau d'électrons, des grilles métalliques à l'échelle nanometrique ont été définies sur la surface de l'échantillon afin de créer des constrictions unidimensionnelles dans le gaz de trous bidimensionnel. J'ai ainsi réussi à observer la quantification de la conductance dans des fils quantiques d'une longueur allant jusqu'à ~ 600 nm. Dans ces fils, j'ai étudié l'effet Zeeman sur les sous-bandes unidimensionnelles. J'ai trouvé des grands facteurs g pour le champ magnétique perpendiculaire, et des petits facteurs g dans le plan. Cette forte anisotropie indique un caractère de trou lourd prédominant, ce qui est attendu dans le cas d'un confinement dominant dans la direction perpendiculaire. Les grands facteurs g et le caractère unidimensionnel balistique sont des propriétés favorables à la réalisation de fermions de Majorana. Enfin, j'ai commencé à explorer le potentiel des hétérostructures à base de Ge pour la réalisation de dispositifs à points quantiques, en visant des applications en calcul quantique à base de spin. Au cours des derniers mois, j'ai pu observer des signes évidents de transport à un seul trou, posant ainsi les bases pour des études plus approfondies sur les points quantiques des trous.

Abstract

Aiming towards largely integrated quantum bits (qubits) requires the development of solid-state, two-level quantum systems, such as spins in quantum dots or Majorana fermions in one-dimensional wires. Holes confined in low-dimensional, germanium-based heterostructures are good candidates for such qubits because they offer i) large spin-orbit interaction (SOI), leading to conveniently large g factors, ii) reduced hyperfine coupling, which is important for long spin coherence, and iii) relatively low effective masses, favoring quantum confinement. In this thesis, I have investigated hole transport in one- and two-dimensional systems made from compressively strained Ge/$Si_{0.2}Ge_{0.8}$ heterostructures. An important part of my research work has been devoted to developing the recipes for device fabrication. I have started from the fabrication of gated Hall bar devices from nominally undoped Ge/SiGe heterostructures. I have studied two types of the heterostructures embedding a strained Ge quantum well: one where the Ge well is at the surface, hence easily accessible to metal contacts, and one where it is buried 70 nm below the surface, a configuration resulting in higher hole mobility. The electronic properties of the two-dimensional hole gas confined to the Ge well were studied by means of magneto-transport measurements down to 0.3 K. My measurements revealed a dominant heavy-hole character, which is expected from the presence of a compressive strain in combination with two-dimensional confinement. The surface-Ge devices showed diffusive transport and a weak anti-localization effect, which is due to SOI in combination with quantum interference. The fact that the Ge quantum well is located at the surface allows for relatively large perpendicular electric fields and hence enhanced Rashba-type SOI. I was able to estimate a spin splitting of around 1 meV. For the realization of quantum nano-devices, I used the heterostructure with a buried Ge well where the hole mobility approaches 2×10^5 cm^2/Vs. Using e-beam lithography, sub-micron metal gates were defined on sample surface in order to create one-dimensional constrictions in the two-dimensional hole gas. I succeeded in observing conductance quantization in hole quantum

wires with a length up to ~ 600 nm. In these wires I investigated the Zeeman splitting of the one-dimensional subbands, finding large perpendicular g-factors as opposed to small in-plane g-factors. This strong anisotropy indicates a prevailing heavy-hole character, which is expected in the case of a dominant confinement in the perpendicular direction. The large g factors and the ballistic one-dimensional character are favorable properties for the realization of Majorana fermions. Finally, I have begun to explore the potential of Ge-based heterostructures for the realization of quantum-dot devices, having in mind applications in spin-based quantum computing. During the last months, I was able to observe clear evidence of single-hole transport, laying the ground for more in-depth studies of hole quantum dots.

Contents

Chapter 1

Introduction

1.1 Quantum computation

It has been half a century since Moore's law started stimulating the development of transistor technology [1]. Even now, the law is still applicable but apparently getting to the end because quantum mechanics become influential as the transistor size becomes close to several atoms. On the other hand, researchers have been exploring alternative computing paradigms. One candidate is the (universal) quantum computer (QC) exploiting the quantum superposition and entanglement of two-level quantum systems [2], usually referred to as quantum bits or qubits. Each qubit consists of two states ($|0\rangle$ and $|1\rangle$), like a bit in ordinary computers, but quantum mechanics allows for any arbitrary coherent superposition the two states, resulting in a much larger and continuous set of possible states. This, together with the possibility of creating correlated (i.e. entangled) multi-qubit states, enables the QC to solve certain classes of problems exponentially faster than a classical computer [3, 4]. In the last few decades, many quantum systems have been proposed to make qubits: cold atoms, photons, superconducting circuits, semiconductor quantum dots, etc. The "quantum processors" realized so far contain at most a few tens of qubits and they have been used to run rudimental quantum algorithms. In order to attain the computational power necessary for solving non-trivial problems, a QC requires a much larger number of integrated qubits (according to the most recent estimates from Microsoft researchers, the factorization of numbers as large as those employed in cryptography would require billions of qubits).

1.2 Spin qubits in quantum dots

Among all qubit systems investigated so far, semiconductor spin qubits based on silicon are considered among the most competitive candidates, especially because of their scalability potential. A nano-size semiconductor block (10 nm $\sim$ 100 nm), usually referred to as quantum dot (QD), can confine one or more electrons or holes which can encode a qubit in their spin degree of freedom. Together with the scalability proper to solid-state systems, semiconductor QDs are small enough to allow billions of them to be fabricated on the same chip. In the case of silicon-based QDs, the high level of control and maturity of silicon technology can be leveraged in the up-scaling challenge.

The spin state of a QD, while relatively decoupled from the environment, can still be manipulated with the aid of an AC magnetic or electric field (Fig. 1.1, top left). Whereas the first spin qubit exploited the AC

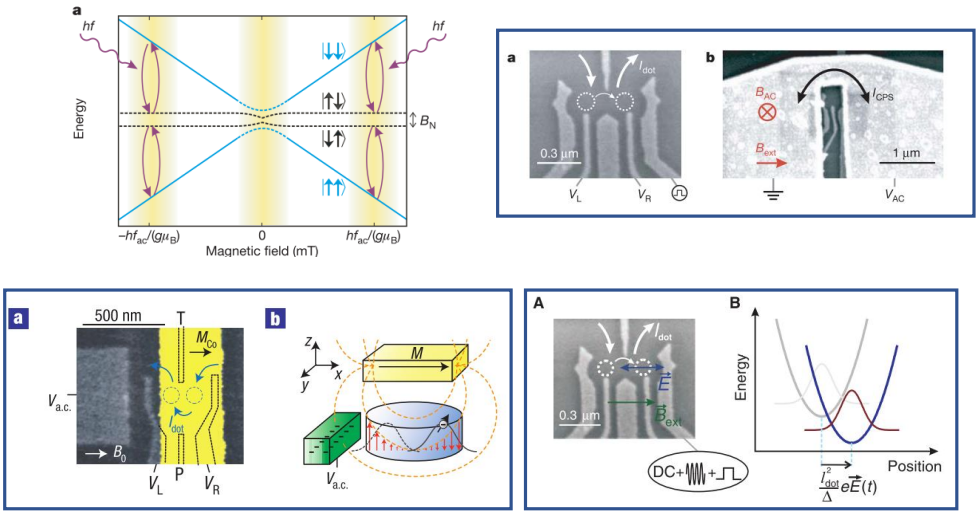

Figure 1.1: Schematic and different mechanisms for spin resonance. (Left top) Energy diagram of two spin states in a double QD as a function of magnetic field. The singlet and triplet states with $S_z = 0$ are splitted into the two antiparallel states by nuclear field, B_N. When a RF signal, hf_{ac}, matches the Zeeman splitting, $g\mu_B B$, spin resonance occurs. (Right top) Coplanar strip line, (Left bottom) micromagnet and (Right bottom) spin-orbit interaction are used for the spin resonance. The figures are from Ref. [5–7].

magnetic field generated by on-chip coplanar stripline (Fig. 1.1, top right) [5], the use of electric-field manipulation presents practical advantages in terms of scalability and manipulation speed. It requires the presence of a sizable spin-orbit coupling, which can be intrinsic to the material (Fig. 1.1, bottom right) [6] or artificially engineered with the aid of locally fabricated micromagnets generating a magnetic-field gradient (Fig. 1.1, bottom right) [7]. The relatively small energy difference between the spin eigenstates of a qubit (typically below 100 μeV) makes it possible to drive qubit rotations with AC signals in the GHz range. Controlled spin rotations are achieved by applying resonant microwave pulses. The pulse length τ_{op} required to flip a spin qubit (i.e. to perform a π rotation on the Bloch sphere) depends on the Rabi frequency, and hence on the underlying driving mechanism. Typically, τ_{op} ranges between $\sim$1 and $\sim$100 MHz. This time scale, which gives a measure of the average qubit operation time, should be compared with the qubit coherence time T_2^*.

Another aspect to be considered for quantum computing is gate operations between two qubits. For spin-based quantum computing, two-qubit operation via exchange interaction had been proposed by Loss and DiVicenzo [8] and was performed by Petta *et al.* [9]. The operation speed can exceed that of a single qubit gate. Some qubit encodings utilize the fast operation for single qubit gates: singlet-triplet qubit [9] and exchange-only qubit [10, 11]. Each qubit requires a multiple QD structure more complicated than that of a spin qubit.

To detect the parity of a spin qubit, a spin-to-charge conversion technique is needed owing to the weak coupling of spins with their environment. There are two famous ways for the conversion [12, 13]. Ono *et al.* found that the Pauli exclusion principle blocks current between two coupled QDs when one electron stays at each QD and has the same spin, which is referred to as Pauli spin blockade (Fig. 1.2, left) [12]. The blockade can be lifted when one of the spins is rotated by spin resonance. On the other hand, Elzerman *et al.* developed a spin detection technique by utilizing Zeeman energy splitting (Fig. 1.2, right) [13]. Applying a fixed magnetic field to a quantum dot with a reservoir, a voltage pulse can shift spin doublet levels so that only the excited spin is above the Fermi level of the reservoir and tunnels out. In both cases, a charge sensor based on a nanostructure is useful because of its high sensitivity. Dispersive readout with RF signal applied to reservoir or gate [14, 15] is another way to sense the charge transition, which does not require additional structures only for the detection. In common with quantum state detection, the detection should be repeated to exactly acquire the state since the polarity of a spin is obtained stochastically, depending on the spin superposition.

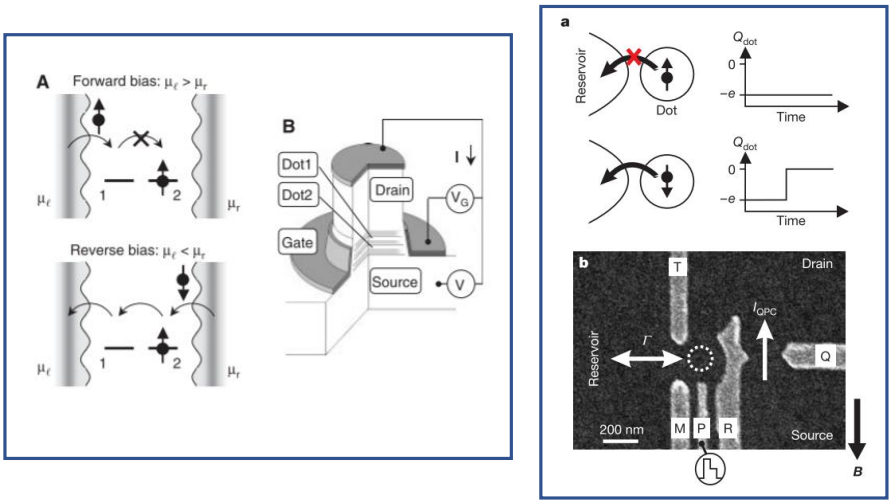

Figure 1.2: Spin-to-charge conversion techniques. (Left) Current blockade effect depending on spin states in a double QD. When two charges, each in a different QD, have the same spin direction, the charge transition from (1,1) to (0,2) is prohibited because of the Pauli exclusion principle. Therefore, the effect is referred to as Pauli spin blocade. (Right) Spin-dependent tunneling to a reservoir. Only the excited spin can tunnel out when the Fermi level of the reservoir is located between the two spin levels in a single QD. The figures are from Ref. [12, 13].

Those pioneering researches utilized quantum dot devices based on n-type GaAs/AlGaAs heterostructures which provide desirable environments with low impurity concentration and low carrier effective mass. Both advantages have been supporting researches on charge and spin transport. However, GaAs has a critical disadvantage such that nuclear spins of Ga and As make a fast decoherence of spins in quantum dots via hyperfine interactions ($T_2^* \sim 10$ ns for electrons in III-V semiconductor heterostructures [9]). Spin refocusing techniques such as the Hahn echo method can suppress the effect of the interactions, revealing the potential of the coherence time of spin qubits (> 1 μs) [9]. To solve this problem intrinsically, other materials without nuclear spins are attracting. It is known that almost all isotopes in group-IV semiconductors do not possess nuclear spins. It motivates researches on QDs made from C [16], Si [17] and Ge [18]. Especially, n-type silicon QDs have been intensively studied to demonstrate long-lived spin coherence ($T_2^* \sim 1$ μs for electrons confined in natural Si [19, 20]). In

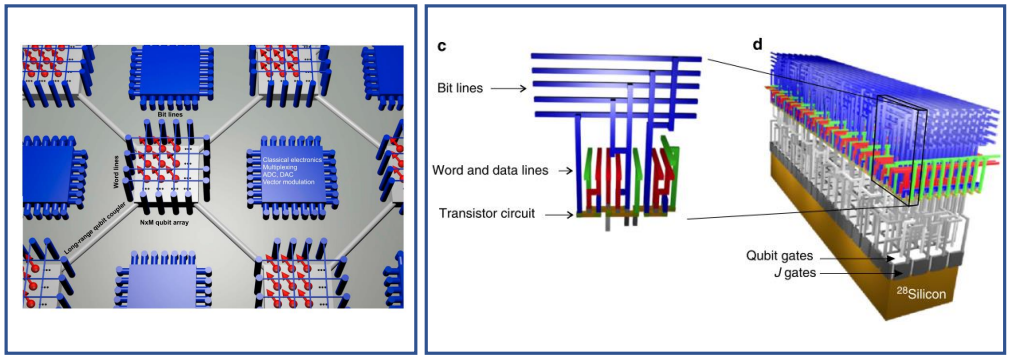

Figure 1.3: Qubit integration scheme for quantum processor. (Left) Dense qubit arrays are connected by long-range qubit couplers, which make space for classical electronics at the same layer with qubits. (Right) 3-D gate architecture for a dense qubit array. The figures are from Ref. [23, 24].

silicon, T_2^* can be further extended by replacing natural Si with isotopically purified Si containing almost solely the spinless ^{28}Si isotope. The relevant figure of merit of a qubit is the ratio between T_2^* (or the Hann-echo T_2) and the characteristic operation time, i.e. $Q = T_2^*/\tau_{op}$. For the silicon spin qubits, $Q \sim 1000$ has been recently reported [21]. Obtaining even higher Q values would be very useful in the prospect of implementing quantum error correction codes which requires a high qubit fidelity ($\gtrapprox 99\%$) [22]. Also in this respect, the group-IV semiconductors with a small amount of nuclear spins are favored for qubits since nuclear field is one of the cause that reduces the fidelity.

In addition to the large Q factor, the n-type Si QD devices have demonstrated high fidelity [20, 25, 21], two-qubit gate [26–28] and coupling of spin qubit with photons in a superconducting cavity for qubit connection at distance [29, 30] which are major ingredients to construct quantum computing systems in large scale [31, 23] (Fig. 1.3 (a)). Still, some obstacles may prevent the realization of QC based on Si QD structure. For example, micromagnet structure for electron spin resonance may not be suitable for 3-D gate architecture such as one discussed in Ref. [24] (Fig. 1.3 (b)). Large effective mass in silicon requires very narrow width of metal gates (for example, 7-nm wire width at minimum is required in Ref. [24]).

1.3 Holes in SiGe-based nanostructures

Because of their inherently strong spin-orbit coupling, holes could provide the way to further reduce τ_{op} while hopefully preserving a long coherence time. Over the recent years, this idea has stimulated a considerable experimental effort on the development of hole-confinement quantum dot devices in Si- and Ge-based nanostructures.

Holes in p-type SiGe-based heterostructures are promising candidates not only for qubits but also for quantum spintronic applications in general, such as spin-valve, or spin- transistor devices [32, 33]. Natural Ge is predominantly constituted of isotopes with zero nuclear spin and holes are less coupled to nuclear spins due to the p-wave symmetry of their Bloch states [34]. Simutaneously, a strong spin-orbit interaction (SOI) enabling electrically-driven hole-spin manipulation has been demonstrated [18]. Until now, most of the experimental work has been carried out on bottom-up SiGe nanostructures: SiGe self-assembled nanocrystals [35, 36], Ge hut wires [37], and Ge/Si core/shell nanowires (Ge/Si NWs) [38–41]. In the prospect of quantum spintronics applications, encouraging spin dephasing and spin coherence times were reported [42–44].

In addition, p-type Ge nanowires were recently proposed as a promising platform for the realization of one-dimensional topological superconductors hosting Majorana fermion (MF) edge modes [45, 46]. MFs are particles (or, more in general, quasiparticles) equal to their own anti-particle. They carry no energy, no charge, and no spin. They always come in pairs. A pair of them is expected to exist at the two edges of a one-dimensional wire in a superconducting topological state [47]. The realization of such an exotic state of matter requires different key ingredients: strong SOI, superconducting proximity effect, and a sufficiently strong magnetic field [48, 45, 49]. Owing to their non-local character, MFs could be used for the realization of topologically protected qubits. Most of the experimental works in this direction have so-far relied on III-V nanowires [50]. The potential of Ge nanostructures for MF devices has been explored by several research groups following different approaches. One-dimensional transport [38, 39], strong SOI [51] and superconducting proximity effect[40, 41] were reported. Yet the way to MF devices remains long due to the challenging requirement to combine these ingredients all together in the same device. In the prospect of realizing scalable MF devices, top-down nanostructures, as opposed to bottom-up ones, appear as a more promising option. Starting from a Ge/SiGe quantum-well (QW) heterostructure confining a high-mobility two-dimensional hole gas, networks of Majorana wires could be defined by means of metal gates patterned on the surface. High quality

p-type Ge/SiGe are today routinely grown showing very high mobilities ($1.3 \times 10^6\,\mathrm{cm}^2/\mathrm{Vs}$) [52], strong SOI (spin splitting energy $\Delta_{SO} \sim 1$ meV) [53, 54] and large out-of-plane g-factors (> 10) [55]. Moreover, the heavy holes of a strained Ge quantum well show a rather small in-plane effective mass [53], which should facilitate the realization of top-down confined devices such as quantum point contacts (QPC), one-dimensional (1D) wires or QDs [56–58].

1.4 This thesis

In my PhD work, I have investigated hole transport in two types of heterostructures having an undoped strained Ge QW grown on relaxed $Si_{0.2}Ge_{0.8}$: one where the Ge QW is located at the surface, and one where it is buried 70 nm below the surface. Both heterostructures are grown by the Maksym Myronov's group at the Warwick university. At the beginning, I devoted most of my research efforts to the development of device fabrication recipes. I started with the realization of gated Hall bar devices in order to study the basic transport properties of the two-dimensional hole gas. Having the Ge QW at the surface is advantageous with respect to the fabrication of metal contacts, and in terms of efficient gating. On the other hand, the buried QW offers a much higher mobility. Eventually, I concentrated my work on this second option. I was able to demonstrate ballistic one-dimensional hole transport and to acquire some first data on single-hole tunneling in QD-type structures.

This thesis consists of seven chapters. Following this chapter (Chapter 1 "**Introduction**"), I shall describe the band theory for hole systems based on the Luttinger Hamiltonian, and shall introduce the notion of heavy and light holes (Chapter 2 "**Band structure in p-type semiconductor**"). In particular, I will demonstrate that a dominant heavy-hole character is expected in strained QWs such as those investigated in my thesis. The lowest-energy hole subbands have a relatively small in-plane effective mass, $k-$cubic spin orbit interaction, anisotropic g-factor. Next, hole transport through low-dimensional structures is discussed (Chapter 3 "**Charge transport in low-dimensional systems**"). The discussion encompasses charge transport in two-, one-, and zero-dimensional systems, with and without spin effects. In the three following chapters, measurement results for low-dimensional hole systems made from Ge heterostructures are presented. The fabrication techniques I used are briefly explained in each experimental chapter while the detailed processing recipes are given in Appendix A. Chapter 4 "**Weak anti-localization in Ge-surface heterostructure**" focuses

on the weak anti-localization effect in two-dimensional magneto-transport, which is brought about by spin-orbit interaction in combination with quantum interference. It is shown that the SOI k-cubic terms have a dominant role. Chapter 5 "**One-dimensional wire in buried Ge/SiGe heterostructure**" reports conductance quantization and g-factor spectroscopy in one-dimensional wires define in a hole two-dimensional gas by means of surface gates. Chapter 6 "**Single quantum dot in buried Ge/SiGe heterostructure**" is devoted to single-hole transport in hole quantum dots. Several gate-defined quantum dot structures are presented and compared. Finally, research perspectives towards Majorana fermions and spin qubits are given in the last chapter (Chapter 7 "**Conclusion**").

Chapter 2

Band structure in p-type semiconductor

2.1 Introduction

Holes and electrons have different electronic properties. Holes are generally characterized by a strong SOI, pronounced g-factor anisotropy, and anisotropic effective masses. There properties can be related to the theory of invariants, which makes the Hamiltonian depend on the crystal structure and symmetry of the semiconductor and on the symmetry of the atomic orbitals. The Luttinger Hamiltonian accouns for orbital and intrinsic angular momenta of holes in the valence band; the p-like character of the orbitals, combined with spin, results in a total angular momentum J=3/2. This Hamiltonian is simple but useful to describe hole properties in cubic semiconductors with large band gap and spin-orbit split-off energy like Ge. In this chapter, at first, we derive the energy dispersion of a band from one-electron Hamiltonian and then briefly explain how symmetry can help in simplifying the Hamiltonian. Next, based on the Hamiltonian for valence band called Luttinger Hamiltonian, energy dispersion, RSOI and g factor for the first HH subband in a QW are deduced.

This chapter is mainly based on the books of Yu *et al*. [59] and Winkler [60].

2.2 Bulk semiconductor

2.2.1 $\boldsymbol{k}\cdot\boldsymbol{p}$ theory

Considering a semiconductor with periodic crystal structure, the potential induced at each atomic site is also periodic $V_0(\boldsymbol{r}) = V_0(\boldsymbol{r}+\boldsymbol{R})$ and so is the wave function $\psi(\boldsymbol{r}) = \psi(\boldsymbol{r}+\boldsymbol{R})$. From Bloch theorem, the wave function is described by $\psi(\boldsymbol{r}) = e^{i\boldsymbol{k}\cdot\boldsymbol{r}}u_{n\boldsymbol{k}}(\boldsymbol{r})$ where $\boldsymbol{k}$ is the wave vector and $u_{n\boldsymbol{k}}(\boldsymbol{r})$ is a function with the periodicity of the crystal. When spin is ignored, by use of this wave function one obtains

$$H_0 e^{i\boldsymbol{k}\cdot\boldsymbol{r}}u_{n\boldsymbol{k}}(\boldsymbol{r}) = \left[\frac{\boldsymbol{p}^2}{2m_0} + V_0(\boldsymbol{r})\right] e^{i\boldsymbol{k}\cdot\boldsymbol{r}}u_{n\boldsymbol{k}}(\boldsymbol{r}) = E_{n\boldsymbol{k}}e^{i\boldsymbol{k}\cdot\boldsymbol{r}}u_{n\boldsymbol{k}}(\boldsymbol{r}) \tag{2.1}$$

$$\left[\frac{\boldsymbol{p}^2}{2m_0} + V_0 + \frac{\hbar^2\boldsymbol{k}^2}{2m_0} + \frac{\hbar\boldsymbol{k}\cdot\boldsymbol{p}}{m_0}\right] u_{n\boldsymbol{k}} = E_{n\boldsymbol{k}}u_{n\boldsymbol{k}}. \tag{2.2}$$

Especially, at $\boldsymbol{k} = \boldsymbol{0}$,

$$\left[\frac{\boldsymbol{p}^2}{2m_0} + V_0\right] u_{n\boldsymbol{0}} = E_{n\boldsymbol{0}}u_{n\boldsymbol{0}}. \tag{2.3}$$

A complete and orthogonal set of basis $u_{n\boldsymbol{0}}$ obtained by solving Eq. 2.3 allows one to expand $u_{n\boldsymbol{k}}$ and $E_{n\boldsymbol{k}}$ by means of standard (non-degenerate) perturbation theory, treating $k = |\boldsymbol{k}|$ as a perturbation,

$$u_{n\boldsymbol{k}} = u_{n\boldsymbol{0}} + \frac{\hbar}{m_0}\sum_{n'\neq n}\frac{\langle u_{n\boldsymbol{0}}|\boldsymbol{k}\cdot\boldsymbol{p}|u_{n'\boldsymbol{0}}\rangle}{E_{n\boldsymbol{0}} - E_{n'\boldsymbol{0}}}u_{n'\boldsymbol{0}} \tag{2.4}$$

and, remaining that

$$E_{n\boldsymbol{k}} = E_{n\boldsymbol{0}} + \frac{\hbar^2\boldsymbol{k}^2}{2m_0} + \frac{\hbar^2}{m_0^2}\sum_{n'\neq n}\frac{|\langle u_{n\boldsymbol{0}}|\boldsymbol{k}\cdot\boldsymbol{p}|u_{n'\boldsymbol{0}}\rangle|^2}{E_{n\boldsymbol{0}} - E_{n'\boldsymbol{0}}} = E_{n\boldsymbol{0}} + \frac{\hbar^2\boldsymbol{k}^2}{2m^*} \tag{2.5}$$

where

$$m^* = m_0\left[1 + \frac{1}{m_0\boldsymbol{k}^2}\sum_{n'\neq n}\frac{|\langle u_{n\boldsymbol{0}}|\boldsymbol{k}\cdot\boldsymbol{p}|u_{n'\boldsymbol{0}}\rangle|^2}{E_{n\boldsymbol{0}} - E_{n'\boldsymbol{0}}}\right]^{-1}$$

and m^* is called effective mass. More general form of the perturbation can be derived by use of canonical transform [61, 62]:

$$\begin{aligned}\langle u_{n\boldsymbol{0}}|\bar{H}|u_{n'\boldsymbol{0}}\rangle &\approx \langle u_{n\boldsymbol{0}}|H|u_{n'\boldsymbol{0}}\rangle + \frac{1}{2}\langle u_{n\boldsymbol{0}}|\left[H_{kp},S\right]|u_{n'\boldsymbol{0}}\rangle \\ &= E_{n\boldsymbol{0}}\delta_{nn'} + \frac{\hbar^2\boldsymbol{k}^2}{2m_0} \\ &+ \frac{\hbar^2}{2m_0^2}\sum_{n''}\left[\frac{\boldsymbol{k}\cdot\boldsymbol{p}_{nn''}\boldsymbol{k}\cdot\boldsymbol{p}_{n''n'}}{E_{n'\boldsymbol{0}}-E_{n''\boldsymbol{0}}} + \frac{\boldsymbol{k}\cdot\boldsymbol{p}_{nn''}\boldsymbol{k}\cdot\boldsymbol{p}_{n''n'}}{E_{n\boldsymbol{0}}-E_{n''\boldsymbol{0}}}\right] \end{aligned} \tag{2.6}$$

where $H = H_0 + \hbar^2\boldsymbol{k}^2/2m_0$, $H_{kp} = \hbar\boldsymbol{k}\cdot\boldsymbol{p}/2m_0$, $\boldsymbol{p}_{nn'} = \langle u_{n\boldsymbol{0}}|\boldsymbol{p}|u_{n'\boldsymbol{0}}\rangle$ and $\delta_{nn'}$ is the Kronecker delta. $\bar{H}$ is canonical transformation of $H + H_{kp}$, $\bar{H} = e^{-S}\left[H + H_{kp}\right]e^{S}$. $\bar{H}$ has the same eigenvalues as $H + H_{kp}$ but with canonical-transformed wave functions and therefore the diagonal terms have the same value as Eq. 2.5 with $p_{nn} = 0$. By choosing S to satisfy $H_{kp} + [H_0, S] = 0$, Eq. 2.6 is derived.

Spin degree is taken into the account by adding (bulk) spin-orbit interaction and Zeeman energy into Eq. 2.1:

$$\begin{aligned} H_0 \quad &\Rightarrow \quad H_0 + \tfrac{\hbar}{4m_0^2c^2}\boldsymbol{p}\cdot\boldsymbol{\sigma}\times(\nabla V_0) + \frac{1}{2}g_0\boldsymbol{\sigma}\cdot\boldsymbol{B} \\ \boldsymbol{p} \quad &\Rightarrow \quad \boldsymbol{p} + e\boldsymbol{A} \end{aligned} \tag{2.7}$$

where $g_0 = 2$ and e are the g factor and the charge of a free electron, respectively, $\boldsymbol{\sigma}$ is the vector of Pauli matrices, $\boldsymbol{B}$ is magnetic field and $\boldsymbol{A}$ is vector potential. From the definition of $\hbar\boldsymbol{k} = -i\hbar\nabla + e\boldsymbol{A}$ and $\boldsymbol{B} = \nabla\times\boldsymbol{A}$, one obtains that $\boldsymbol{k}\times\boldsymbol{k} = -ie\boldsymbol{B}/\hbar$. Through this relation, a Zeeman-like energy appears in off-diagonal terms and the g factor of a band can be perturbatively modified by other bands.

Also, external fields can be treated by the $\boldsymbol{k}\cdot\boldsymbol{p}$ theory [60]. When the external fields vary slowly compared to $u_{n\boldsymbol{0}}(\boldsymbol{r})$, the wave function in the external field $\Psi(\boldsymbol{r})$ is expanded on the basis of $u_{n\boldsymbol{0}}(\boldsymbol{r})$ with a non-periodic amplitude depending on position and spin $\psi_{n,\sigma}(\boldsymbol{r})$ (envelop function approximation):

$$\Psi(\boldsymbol{r}) = \sum_{n,\sigma}\psi_{n,\sigma}(\boldsymbol{r})u_{n\boldsymbol{0}}(\boldsymbol{r})|\sigma\rangle \tag{2.8}$$

where $|\sigma\rangle$ is the spin eigenstate. Similarly to the derivation above, one can obtain simultaneous infinite differential equations like Eq. 2.2 but for $\psi_{n,\sigma}$ [60]. Perturbation theory (Löwdin perturbation [60, 63]) can convert the infinite differential equations into finite equations. As a result, for example, a nondegenerate, isotropic parabolic band can have the effective mass Hamiltonian:

$$H_{eff}\psi_{n,\sigma} = E_{n,\sigma}\psi_{n,\sigma}$$

$$H_{eff} = \frac{(-i\hbar\nabla + e\boldsymbol{A})^2}{2m_n^*} + V(\boldsymbol{r}) + \frac{1}{2}g_n^*\mu_B\boldsymbol{\sigma}\cdot\boldsymbol{B} \tag{2.9}$$

where m_n^* and g_n^* are the effective mass and g factor of n^{th} band, respectively, $V(\boldsymbol{r})$ is the external potential, and $\boldsymbol{B}$ is the external magnetic field. Thanks to this envelop function approximation, in many cases one can solve a eigenvalue problem without knowing the atomic-scale details of the wavefunction.

However, ignoring the microscopic details of the wavefunction is not always allowed. For example, carrier spins can couple with nuclear spins via hyperfine interactions depending on the overlap of the electronic wavefunction with the nuclei. Figure 2.1 shows the wavefunction of an electron (hole) modulated by s- (p-) orbital atomic states and confined in an InGaAs QD. In Ref. [64], it is demonstrated that the coherence time of hole spin states is significantly longer than the one of electron spins. This follows from a reduced hyperfine interaction, due to the vanishing overlap between p-orbital states and the nuclei.

2.2.2 Theory of invariants

In the previous section, the $\boldsymbol{k}\cdot\boldsymbol{p}$ Hamiltonian was obtained in a general form. The symmetry properties of the semiconductor crystal translate into special symmetries in the Hamiltonian. In particular symmetry can introduce important simplifications. For example, $|\langle u_{n\boldsymbol{0}}|\boldsymbol{p}|u_{n'\boldsymbol{0}}\rangle|$ depends on the symmetry of $u_{n\boldsymbol{0}}$ and $u_{n'\boldsymbol{0}}$. When both are even or odd functions, since $\boldsymbol{p}$ inverts the even/odd parity of $u_{n'\boldsymbol{0}}$, the value vanishes after the integral. In the (extended) Kane Hamiltonian [60], the orbitals around the band gap (bonding p-like orbitals for the valence band and anti-bonding s-like and p-like orbitals for the conduction band) are considered together with spins. As a result, the Hamiltonian is expressed by 14×14 matrix, where many terms vanish owing to the symmetries of the bands.

Moreover, one can anticipate the structure of the Hamiltonian from symmetry considerations using the so-called theory of invariants. The idea is that parts of the Hamiltonian are classified by invariants under transformations of a given symmetry group. In the following, we shall consider the crystal structure of zincblende (*e.g.*, ZnS and GaAs) and diamond (*e.g.*,

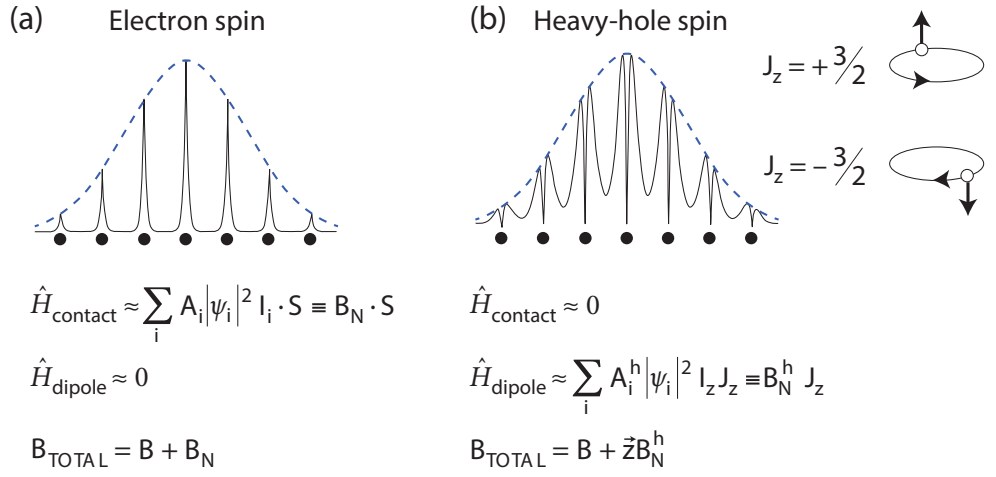

Figure 2.1: The probability density of (a) electron spin and (b) HH spin confined in a InGaAs quantum dot (black solid line). Electron spin is constructed from s-orbital state at each atom while HH spin, from p orbitals (dots indicate atoms). The probabilities are modulated by envelope function due to mesoscopic confinement potential (blue dashed line). The contact (dipole) term of hyperfine interaction $\hat{H}_{contact}$ ($\hat{H}_{dipole}$) couples the angular momentum of electron S and hole J with the nuclear spin I_i (A_i is coupling coefficient with i^{th} atom and ψ_i is the electron wave function at site i). Reflecting the difference in orbital, $\hat{H}_{contact}$ ($\hat{H}_{dipole}$) has different effects on electron and HH spins, resulting in fictitious magnetic fields $\boldsymbol{B}_N$. In Ref. [64], it is shown that $|\langle A_{h,z}\rangle / \langle A_e\rangle| = 10\%$ and even in a III-V semiconductor quantum dot coherence time can be significantly long: $T_2^* > (460 \pm 80) ns$. Figure is taken from Ref. [65].

Si and Ge), which have different symmetries. Since zinc-blende semiconductors are composed of two atoms, the inversion symmetry is broken. On the contrary the inversion symmetry exists in diamond semiconductors [59]. From the view point of group theory, it is known that zincblende and diamond crystal structures belong to the tetrahedral group T_d and the octahedral group O_h, respectively. This results in a differet form of the corresponding Hamiltonians as shown below. Based on symmetry, the Hamiltonian H of a generic bulk semiconductor can be separated into three components [60]:

$$H = H_{spher} + H_{cube} + H_{tetra} \tag{2.10}$$

where the H_{spher}, H_{cube}, and H_{tetra} terms are invariant under transformations of the spherical rotation group $\mathcal{R}$, O_h and T_d, respectively. According to hierarchical relation $\mathcal{R} \supset O_h \supset T_d$, H_{spher} represents the largest component in the Hamiltonian. Therefore, to a first approximation one could retain only this component (i.e. $H \approx H_{spher}$) and ignore the other terms. This is the so-called spherical approximation. In group-IV semiconductors, the cubic term cannot be ignored while it is not important for in semiconductors of the III-V group. Including H_{cube} is known as the cubic approximation.

2.2.3 Luttinger Hamiltonian

From the theory of invariants, Luttinger [66] deduced the Hamiltonian for a valence band composed of HH band ($|J, J_z\rangle = |3/2, \pm 3/2\rangle$) and LH band ($|J, J_z\rangle = |3/2, \pm 1/2\rangle$). This Hamiltonian is valid when the semiconductor has a large band gap E_g and a large spin-orbit split-off energy Δ_{SO} such that conduction band and split-off band are treated as small perturbations. Without magnetic field the Hamiltonian reads

$$H_L = \frac{\hbar^2}{2m_0}\left[(\gamma_1 + \frac{5}{2}\gamma_2)\boldsymbol{k}^2 - 2\gamma_2(k_x^2 J_x^2 + c.p.) - 4\gamma_3(\{k_x k_y\}\{J_x J_y\} + c.p.)\right] \tag{2.11}$$

where $\boldsymbol{J}$ and J_i are the total angular momentum operator for $J = 3/2$ and its projection alone the i direction ($i = x, y$ or z); $\gamma_1, \gamma_2, \gamma_3$ are the Luttinger parameters and $\{AB\} = (AB + BA)/2$.

As explained in the previous section, this Hamiltonian can be decomposed into terms corresponding to different symmetries. Baldereschi and Lipari [67] demonstrated that (spherical approximation):

$$H_L^s = \frac{\hbar^2}{2m_0}\left[(\gamma_1 + \frac{5}{2}\tilde{\gamma_2})\boldsymbol{k}^2 - 2\tilde{\gamma_2}(\boldsymbol{k}\cdot\boldsymbol{J})^2\right] + H_{cube}$$

where $\tilde{\gamma_2} = (2\gamma_2 + 3\gamma_3)/5$. Without H_{cube}, the energy dispersion is symmetric:

$$E_{LH/HH}(\boldsymbol{k}) = \frac{\hbar^2}{2m_0}(\gamma_1 \pm \tilde{\gamma_2})\boldsymbol{k}^2. \tag{2.12}$$

Owing to the fact that $H_{cube} \propto (\gamma_3 - \gamma_2)$, a parameter $\eta = (\gamma_3 - \gamma_2)/\tilde{\gamma_2}$ can measure the contribution of cubic symmetry. In semiconductors with

large Δ_{SO}, η is small and therefore H_{cube} is often ignored [68], see Table 2.1. From the table, it is clear that Ge and III-V semiconductors have small η (while in Si η is so large that H_{cube} cannot be ignored). Nevertheless, we consider the effects of the cubic term in this thesis because they can affect the Rashba SOI and the in-plane g factor of HH at high orders in the perturbation theory.

In the Luttinger Hamiltonian, the effect of the conduction band and the spin-orbit split-off band is taken into account as perturbation. When one needs more accurate calculations, the Kane Hamiltonian, which can include even higher conduction bands, can be used. However, this is not our case because Ge has a large E_g and Δ_{SO} (see Table 2.1). In the next section, we shall employ the Luttinger Hamiltonian to derive the main properts of the lowest energy hole subbands in a two-dimensional QW.

Table 2.1: List of band structure parameters for conventional semiconductors: band gap E_g ((i) denotes indirect band gap), spin-orbit split-off gap Δ_{SO} and Luttinger parameters, $\gamma_1, \gamma_2, \gamma_3, \kappa$ and q. All of the parameters are taken from Ref. [60] except for band gap for Ge and Si [69]

	Ge	Si	GaAs	InAs	InSb
E_g (meV)	740(i)	1170(i)	1519	418	237
Δ_{SO} (meV)	296	44.1	341	380	810
γ_1	13.38	4.285	6.85	20.40	37.10
γ_2	4.24	0.339	2.10	8.30	16.50
γ_3	5.69	1.446	2.90	9.10	17.70
κ	3.41	-0.42	1.20	7.60	15.60
q	0.06	0.01	0.01	0.39	0.39

2.3 Heavy holes in two dimensional system

2.3.1 Two-dimensional system

By applying Löwdin perturbation, the 2D Hamiltonian of first HH subband H_{HH1} can be obtained. Following Marcellina *et al.* [70], we demonstrate it in this section. We shall start from re-writing the Luttinger Hamiltonian (Eq. 2.11) in an explicit matrix notation:

$$H_L = \begin{pmatrix} H_{hh} & H_{hl} \\ H_{hl}^{\dagger} & H_{ll} \end{pmatrix} = \frac{\hbar^2}{2m_0} \begin{pmatrix} P+Q & 0 & L & M \\ 0 & P+Q & M^* & -L^* \\ L^* & M & P-Q & 0 \\ M^* & -L & 0 & P-Q \end{pmatrix} \tag{2.13}$$

where

$$\begin{gathered} P = \gamma_1(k^2 + k_z^2), Q = -\gamma_2(2k_z^2 - k^2), \\ L = -2\sqrt{3}\gamma_3 k_- k_z, M = -\sqrt{3}(\overline{\gamma}k_-^2 - \zeta k_+^2), \\ \tilde{\gamma} = \frac{\gamma_3 + \gamma_2}{2}, \zeta = \frac{\gamma_3 - \gamma_2}{2} \\ k^2 = k_x^2 + k_y^2, k_\pm = k_x \pm i k_y \end{gathered} \tag{2.14}$$

and the basis are $\{|3/2, +3/2\rangle, |3/2, -3/2\rangle, |3/2, +1/2\rangle, |3/2, -1/2\rangle\}$.

The off-diagonal terms H_{hl}, $H_{hl}^{\dagger}$ can be treated as perturbations. Before starting the perturbation calculation, we focus on the diagonal terms H_{hh} and H_{ll}:

$$H_{hh} = \frac{\hbar^2}{2m_0}(P+Q) = \frac{\hbar^2}{2m_0}\left[(\gamma_1 + \gamma_2)k^2 + (\gamma_1 - 2\gamma_2)k_z^2\right] \tag{2.15}$$

$$H_{ll} = \frac{\hbar^2}{2m_0}(P-Q) = \frac{\hbar^2}{2m_0}\left[(\gamma_1 - \gamma_2)k^2 + (\gamma_1 + 2\gamma_2)k_z^2\right]. \tag{2.16}$$

It is clearly seen that the out-of-plane effective mass (*i.e.*, along z direction) of heavy holes ($m_\perp^h = m_0/(\gamma_1 - 2\gamma_2)$) is heavier than one of light holes ($m_\perp^l = m_0/(\gamma_1 + 2\gamma_2)$) while the relation is opposite for the in-plane effective masses: $m_{/\!/}^h = m_0/(\gamma_1 + \gamma_2)$, $m_{/\!/}^l = m_0/(\gamma_1 - \gamma_2)$. The difference in $m_\perp$ results in a HH-LH splitting in the 2DHG. In other words, as seen in the z component of the Luttinger Hamiltonian under spherical approximation,

$$(H_L)_z = \frac{\hbar^2}{2m_0}\left[(\gamma_1 + \frac{5}{2}\tilde{\gamma_2})k_z^2 - 2\tilde{\gamma_2}(k_z \cdot m_j)^2\right], \tag{2.17}$$

where $m_j = \pm 3/2$ or $\pm 1/2$ is the z component of total angular momentum, the HH-LH degeneracy at $k = 0$ can be lifted by [001] confinement and then HH becomes the ground state. This applies to the case of heterostructures grown along the [001] direction, such as those used for the experiments in this PhD work. Therefore we shall consider here only the [001] QW confinement .

In a QW heterostructure of in the presence of out-of-plane electric fields leading to hole confinement in the vertical direction, HH and LH bands are quantized into HH and LH two-dimensional subbands, respectively: $|H_n\sigma_h\rangle$ and $|L_m\sigma_l\rangle$ where n and m are subband index for HH and LH subbands, respectively, and $\sigma =\uparrow$ ($J_z = +3/2$ or $+1/2$) or $\downarrow$ ($J_z = -3/2$ or $-1/2$). In order to obtain the energy dispersion of the first HH subband, after quantization in z direction under the envelop function approximation, Löwdin perturbation ignoring higher energy levels like the other HH or LH subbands. Treating HH-LH coupling H_{hl} by Löwdin perturbation, the leading-order (second-order) diagonal terms are

$$\begin{aligned}
&\langle H_1\uparrow|H^{(2)}|H_1\uparrow\rangle \\
&= \frac{1}{2}\sum_{m,\sigma_l}\langle H_1\uparrow|H_{lh}|L_m\sigma_l\rangle\langle L_m\sigma_l|H_{hl}|H_1\uparrow\rangle\left[\frac{1}{E_1^h-E_m^l}+\frac{1}{E_1^h-E_m^l}\right] \\
&= \frac{\hbar^4}{4m_0^2}\sum_m\frac{|\langle L_m\uparrow|L|H_1\uparrow\rangle|^2+|\langle H_1\uparrow|M|L_m\downarrow\rangle|^2}{E_1^h-E_m^l} \\
&= \langle H_1\downarrow|H^{(2)}|H_1\downarrow\rangle
\end{aligned} \tag{2.18}$$

where E_i^A is the unperturbated energy of A (=h (HH) or l (LH)) with subband index i. Without perturbation, here are no spin-dependent terms in H_{hh} and H_{ll} and hence the spin label for the energy is cut out.

In fact, we can know the k dependence also from the theory of invariants. O_h symmetry, the symmetry of the diamond structure, is lifted by quantum confinement along growth direction (*e.g.*, [001] direction), leading to a lower symmetry, *e.g.*, C_{4v} in the QW [60]. One obtains the spin-independent diagonal term (here, only the diagonal term in HH1 subspace is focused on. The off-diagonal term is discussed below):

$$H_{HH1} = Ak^2 - Bk^4 - d(k_+^2 - k_-^2)^2. \tag{2.19}$$

By inserting the L and M into Eq. 2.14, one can obtain the prefactors A, B and d:

$$\begin{aligned}
A &= \frac{\hbar^2}{2m_0}\left\{\gamma_1+\gamma_2+\frac{6\hbar^2\gamma_3^2}{m_0}\sum_m\frac{|\langle H_1|k_z|L_m\rangle|^2}{E_1^h-E_m^l}\right\} \\
B &= -\frac{3}{4}\frac{\hbar^4}{m_0^2}(\tilde{\gamma}-\zeta)^2\sum_m\frac{|\langle H_1|L_m\rangle|^2}{E_1^h-E_m^l} \\
d &= \frac{3}{4}\frac{\hbar^4}{m_0^2}\tilde{\gamma}\zeta\sum_m\frac{|\langle H_1|L_m\rangle|^2}{E_1^h-E_m^l}.
\end{aligned}$$

Here, we treated k_z as an operator while k_x and k_y are kept as numbers. The first term in Eq. 2.19 describes the parabolic term and when one ignores the high-order terms in k, the effective mass is obtained:

$$m^* = \left(\frac{1}{\hbar k} \frac{dE(k)}{d(\hbar k)} \right)^{-1} = m_0 \left\{ \gamma_1 + \gamma_2 + \frac{6\hbar^2 \gamma_3^2}{m_0} \sum_m \frac{|\langle H_1 | k_z | L_m \rangle|^2}{E_1^h - E_m^l} \right\}^{-1}. \tag{2.20}$$

This equation indicates that HH-LH mixing reduces the effective mass. If high-order terms are taken into account, the effective mass depends also on the absolute value and the direction of $\boldsymbol{k}$.

There is another effect to be considered: strain. Here, the strain is based on the difference in the lattice parameters of Si and Ge. In our heterostructures, the Ge QW is grown on a thick and relaxed $Si_{0.2}Ge_{0.8}$ layer, which causes a compressive biaxial strain in the QW. In this case, the compressive strain contributes only to diagonal terms of the Hamiltonian and it enhances the energy spacing between heavy holes, light holes and split-off holes (see Fig. 2.2) [71, 62].

The explanation in this section is based on Ref. [35, 70, 60].

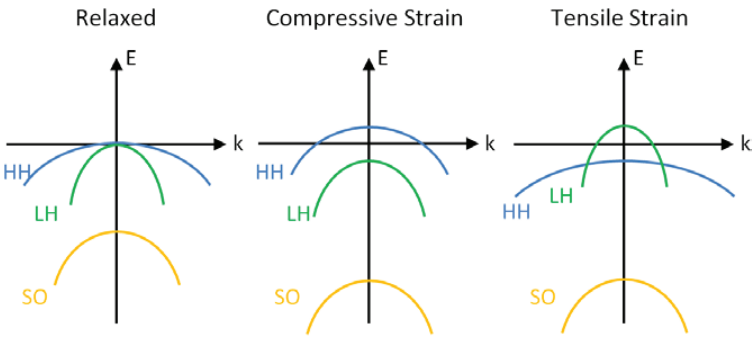

Figure 2.2: Schematic energy dispersion of valence band: HH, LH, and SO (split-off hole). Without strain (left), HH and LH are degenerate at $\boldsymbol{k} = \boldsymbol{0}$ and SO is separated by Δ_{SO}. Strain lifts the degeneracy between HH and LH bands, but the precise effect depends on the nature of the strain (tensile vs compressive strain). This figure is taken from Ref. [72].

2.3.2 Rashba spin orbit interaction (RSOI)

RSOI is important from the point of view of applications in spintronics. RSOI couples spin, momentum and electric field and thereby the direction

of the spin can be controlled by an electric field. From the theory of invariants, the SOI is supposed to be due to lacking of inversion symmetry. Here, crystal electric fields destroy the macroscopic symmetry (Structure Inversion Asymmetry, SIA). This happens in compound materials made from two elements (such as GaAs), lacking bulk inversion asymmetry (BIA), resulting in a SOI so-called Dresselhaus SOI. In a Ge QW, the bulk inversion symmetry is preserved and, therefore, only the Rashba term is relevant (in fact, the inversion symmetry may be broken at the interface of the QW [73], but this scenario is difficult to model and quantitatively evaluate and it will not be considered in this thesis).

For the lowest HH subband in a 2DHG, the same as Eq. 2.18, the off-diagonal terms are obtained:

$$\begin{aligned}
&\langle H_1\uparrow|H^{(2)}|H_1\downarrow\rangle \\
&= \frac{1}{2}\sum_{m,\sigma_l}\langle H_1\uparrow|H_{lh}|L_m\sigma_l\rangle\langle L_m\sigma_l|H_{hl}|H_1\downarrow\rangle\left[\frac{1}{E_1^h-E_m^l}+\frac{1}{E_1^h-E_m^l}\right] \\
&= \frac{\hbar^4}{4m_0^2}\sum_m\left[\frac{\langle H_1\uparrow|L^*|L_m\uparrow\rangle\langle L_m\uparrow|M^*|H_1\downarrow\rangle}{E_1^h-E_m^l}\right. \\
&\qquad\left.+\frac{\langle H_1\uparrow|M^*|L_m\downarrow\rangle\langle L_m\downarrow|(-L^*)|H_1\downarrow\rangle}{E_1^h-E_m^l}\right] \\
&= \langle H_1\downarrow|H^{(2)}|H_1\uparrow\rangle^*. \qquad (2.21)
\end{aligned}$$

The off-diagonal terms read

$$H_{RSOI}^{HH1} = i\alpha_{R2}(k_+^3\sigma_- - k_-^3\sigma_+) + i\alpha_{R3}(k_+\sigma_+ - k_-\sigma_-)k^2 \qquad (2.22)$$

where

$$\begin{aligned}
\alpha_{R2} &= -\frac{3}{2}\frac{\hbar^4}{m_0^2}\gamma_3\tilde{\gamma}\sum_m\frac{\langle H_1|L_m\rangle\langle L_m|k_z|H_1\rangle-\langle H_1|k_z|L_m\rangle\langle L_m|H_1\rangle}{E_1^h-E_m^l} \\
\alpha_{R3} &= \frac{3}{2}\frac{\hbar^4}{m_0^2}\gamma_3\zeta\sum_m\frac{\langle H_1|L_m\rangle\langle L_m|k_z|H_1\rangle-\langle H_1|k_z|L_m\rangle\langle L_m|H_1\rangle}{E_1^h-E_m^l}.
\end{aligned}$$

Eq. 2.22 is also predicted from the theory of invariants [70].

The electric field is included in the wave functions of HHs and LHs and therefore the dependence is not obvious in the factors α_{R2} and α_{R3}.

There is another approach to obtain RSOI for the first HH subband. RSOI for the bulk valence band with $J = 3/2$ under electric fields $\boldsymbol{E} = E_z\hat{z}$ can be derived from the Kane Hamiltonian [60]:

$$H_{RSOI}^{bulk} = \alpha E_z \begin{pmatrix} 0 & \frac{i\sqrt{3}}{2}k_- & 0 & 0 \\ -\frac{i\sqrt{3}}{2}k_+ & 0 & ik_- & 0 \\ 0 & -ik_+ & 0 & \frac{i\sqrt{3}}{2}k_- \\ 0 & 0 & -\frac{i\sqrt{3}}{2}k_+ & 0 \end{pmatrix} \tag{2.23}$$

where the basis are $\{|3/2,+3/2\rangle, |3/2,+1/2\rangle, |3/2,-1/2\rangle, |3/2,-3/2\rangle\}$ and weak RSOI terms are ignored. Obviously, HH spins do not mix up through H_{RSOI}^{bulk} to the first order. However, RSOI derived from high-order perturbation is still possible. By treating E_z and the off-diagonal H_{hl} by perturbation theory with the RSOI Hamiltonian of Eq. 2.23 [74], one obtains

$$H_{RSOI}^{HH1} = i\alpha_{c1}E_z(\{k_+, k_-^2\}\sigma_- - \{k_+^2, k_-\}\sigma_+) + i\alpha_{c2}E_z(k_+^3\sigma_- - k_-^3\sigma_+) \tag{2.24}$$

where

$$\begin{aligned} \alpha_{c1} &= \frac{2e\hbar^4}{m_0^2}\gamma_3\zeta D_1^h,\ \alpha_{c2} = \frac{2e\hbar^4}{m_0^2}\gamma_3\tilde{\gamma}D_1^h, \\ D_\alpha^h &= \frac{3i}{4}\sum_{\beta\neq\alpha}\Bigg[\frac{\langle H_\alpha|z|H_\beta\rangle\langle L_\beta|(-i\partial_z)|H_\alpha\rangle - \langle H_\alpha|(-i\partial_z)|L_\beta\rangle\langle H_\beta|z|H_\alpha\rangle}{\Delta_{\alpha\beta}^{hh}\Delta_{\alpha\beta}^{hl}} \\ &\quad - \frac{\langle H_\alpha|z|H_\beta\rangle\langle H_\beta|(-i\partial_z)|L_\alpha\rangle - \langle L_\alpha|(-i\partial_z)|H_\beta\rangle\langle H_\beta|z|H_\alpha\rangle}{\Delta_{\alpha\beta}^{hh}\Delta_{\alpha\alpha}^{hl}} \\ &\quad + \frac{\langle L_\alpha|z|L_\beta\rangle\langle L_\beta|(-i\partial_z)|H_\alpha\rangle - \langle H_\alpha|(-i\partial_z)|L_\beta\rangle\langle L_\beta|z|H_\alpha\rangle}{\Delta_{\alpha\alpha}^{hl}\Delta_{\alpha\beta}^{hl}}\Bigg] \end{aligned}$$

and α and β are subband indexes.

Comparing the two approaches, we reach the conclusion that the most appropriate approximation (i.e. the perturbation order) depends on the difference symmetry of the QW. In triangular QWs, the first approach, where RSOI is determined up to second-order perturbation ($\propto \Delta_{hl}^{-1}$), is adequate. In symmetric QWs, however, the second approach, where RSOI is determined up to third-order perturbation ($\propto \Delta_{hl}^{-2}$) [70], is more appropriate. Interestingly, in the case of HH states, RSOI is always dominated by k-cubic terms rather than k-linear terms. This contrasts with the case of electrons and LHs, for which k-linear terms provide the most important contribution. The cubic nature of the RSOI can be seen also in the direction of the associated effective magnetic field as shown in Fig. 2.3.

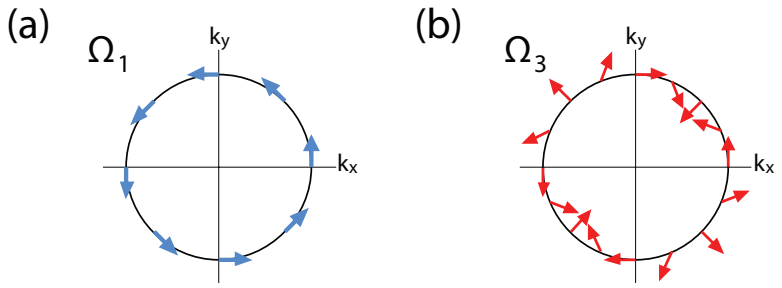

Figure 2.3: The direction of the effective magnetic field for (a) k-linear RSOI and (b) k-cubic RSOI in reciprocal space (blue/red arrows). Moving along a circle in k-space, the field direction reverses one time in (a) and three times in (b). This Fig. is reproduced from Ref. [75].

2.3.3 g factor anisotropy

Zeeman energy can be deduced by Kane Hamiltonian under magnetic field $\boldsymbol{B}$:

$$\begin{aligned} H_z &= \frac{1}{2}\mu_B \boldsymbol{g}\cdot\boldsymbol{B} = \frac{1}{2}\mu_B(4\kappa\boldsymbol{J}+4q\boldsymbol{\mathcal{J}})\cdot\boldsymbol{B} \\ &= \frac{1}{2}\mu_B\left[\begin{pmatrix} 6\kappa B_z & 2\sqrt{3}\kappa B_- & 0 & 0 \\ 2\sqrt{3}\kappa B_+ & 2\kappa B_z & 4\kappa B_- & 0 \\ 0 & 4\kappa B_+ & -2\kappa B_z & 2\sqrt{3}\kappa B_- \\ 0 & 0 & 2\sqrt{3}\kappa B_+ & -6\kappa B_z \end{pmatrix}\right. \\ &\quad \left. + \begin{pmatrix} \frac{27}{2}qB_z & \frac{7\sqrt{3}}{2}qB_- & 0 & 3qB_+ \\ \frac{7\sqrt{3}}{2}qB_+ & \frac{1}{2}qB_z & 10qB_- & 0 \\ 0 & 10qB_+ & -\frac{1}{2}qB_z & \frac{7\sqrt{3}}{2}qB_- \\ 3qB_- & 0 & \frac{7\sqrt{3}}{2}qB_+ & -\frac{27}{2}qB_z \end{pmatrix}\right] \end{aligned} \tag{2.25}$$

where the basis are $\{|3/2,+3/2\rangle, |3/2,+1/2\rangle, |3/2,-1/2\rangle, |3/2,-3/2\rangle\}$, $\boldsymbol{g}$ is g tensor, κ and q are the Luttinger parameters and $\boldsymbol{\mathcal{J}} = (J_x^3, J_y^3, J_z^3)$. The prefactor q is typically two orders of magnitude smaller than κ and therefore we shall neglect it hereafter.

There are no off-diagonal terms in the HH subspace, $\{|H\uparrow\rangle, |H\downarrow\rangle\}$, meaning that in-plane magnetic field cannot couple to HH spins directly, i.e. $g_{/\!/} \approx 0$. On the other hand, the spin response of HHs to an out-of-plane field is determined by a g factor $g_\perp = 6\kappa$, which is much larger than the g factor of a base electron $g_0 = 2$ (see Table 2.1). This anisotropy comes from the

fact that orbital and spin degrees cannot have different quantization axis. Once the quantization axis is fixed by vertical confinement, the quantization axis for the spin of the HH is also fixed to be parallel to the growth direction and hence $g_\perp$ of HH is large while $g_{/\!/}$ is small [60, 76].

One can estimate the out-of-plane g factor of the first HH subband $g_\perp^{HH1}$ following a procedure analogous to the one discussed in the previous section, keeping in mind that $\boldsymbol{k} \times \boldsymbol{k} = -ie\boldsymbol{B}/\hbar$. According to Ref. [77, 78], $g_\perp$ of the first HH subband is

$$g_\perp^{HH1} = 6\kappa + \frac{12\hbar^2\gamma_3^2}{m_0} \sum_m \frac{|\langle H_1|k_z|L_m\rangle|^2}{E_1^h - E_m^l}. \tag{2.26}$$

Just as for the effective mass, HH-LH mixing reduces $g_\perp$.

The perturbation theory predicts that finite $g_{/\!/}$ depends on higher order of k or B. According to Ref. [76], one term of $g_{/\!/}$ depends on $k_{/\!/}$:

$$g_{/\!/}^{HH1} \propto \frac{k_{/\!/}^2}{E_1^h - E_1^l}. \tag{2.27}$$

In the analogy with RSOI, cubic term ($\propto B_{/\!/}^3$) can also appear in Zeeman term but, according to Ref. [60], it can be negligible because the term is expected to have small influence in narrow QW. In addition, kinetic terms can also originate the in-plane Zeeman effect through the relation $\hbar\boldsymbol{k} = -i\hbar\nabla - e\boldsymbol{A}$ [68].

2.4 Conclusion

In conclusion, we have shown how in Ge QW the low in-plane effective mass, cubic nature of RSOI, and strong g factor anisotropy of the first HH subband can be deduced from the Luttinger Hamiltonian. We have also shown how in addition to quantum confinement, the presence of compressive strain, as in the GeSi/Ge/SiGe heterostructures experimentally studied here, enhances the HH-LH splitting, thereby reducing LH-HH mixing and leading to a lowest subband with a dominant HH character.

Besides showing a relatively strong RSOI and large out-of-plane g factors, Ge has the additional property of containing a small natural abundance of isotopes with finite nuclear spin (see Table 2.2). In view of spin-qubit applications, this represents a clear advantage over III-V semiconductors. In addition, Ge/SiGe heterostructures can have 100 meV of HH-LH splitting due to a large compressive strain [75], enabling almost pure HH states.

Table 2.2: Natural isotopes, spin and natural abundance for most commonly used elements in spintronic [79].

Element	Isotope	Nuclear spin	Natural abundance (%)
Germanium	^{70}Ge	0	20.84
	^{72}Ge	0	27.54
	^{73}Ge	9/2+	7.73
	^{74}Ge	0	36.28
	^{76}Ge	0	7.61
Silicon	^{28}Si	0	92.22
	^{29}Si	1/2+	4.69
	^{30}Si	0	3.09
Gallium	^{69}Ga	3/2-	60.108
	^{71}Ga	3/2-	39.892
Indium	^{113}In	9/2+	4.29
	^{115}In	9/2+	95.71
Arsenic	^{75}As	3/2-	100
Antimony	^{121}Sb	5/2+	57.21
	^{123}Sb	7/2+	42.79

Chapter 3

Charge transport in low-dimensional systems

3.1 Introduction

Quantum confinement in semiconductor heterostructures leads to energy quantization and the formation two-dimensional energy subbands. Subband formation becomes prominent when the energy spacing among the subbands is larger than thermal energy broadening. Electronic transport at low temperature is a practical way to acquire information on the electronic properties of the subbands.

Heterostructures confining a two-dimensional (2D) electronic system can be grown, for example, using chemical vapor deposition (CVD) techniques. Homogeneous nanometer-thick layers of high quality can be grown this way. When a nanometer-scale semiconductor layer (e.g., made of Ge) is sandwiched between semiconductors (e.g. SiGe) with a larger energy gap, confining quantum well is formed and its electronic states become quantized along the growth direction. In this system, electronic motion is free in the x-y plane, and, depending of the lateral length scale, it can be ballistic or diffusive. By favoring the formation quantum-Hall edge states with suppressed back scattering, a strong out-of-plane magnetic field can help creating ballistic channels. In the absence of a magnetic field, lateral energy confinement (say along the y direction) can be achieved with the aid external electric fields. This way, a one-dimensional (1D) ballistic channel (along x) can be formed. One approach to apply confining electric fields consists in using metal gate structures deposited on the surface of the heterostructure. This approach is highly versatile and it can also be used to to create zero-dimensional (0D) systems, usually referred to as quantum dots.

By properly designing the surface gate electrodes, the two-dimensional electronic system confined in the QW can be locally depleted in order to obtain quantum circuits consisting of functional elements with different dimensionality (2D, 1D, and 0D) integrated all together. The quantum circuits thus formed can be addressed by means of transport measurements. To this aim, source and drain contacts are connected to the low-dimensional electronic gas (multi-terminal devices with complex geometries can as well be realized). Typically, the source-drain current through the quantum system is measured, *e.g.*, as a function of source-drain bias voltage and gate voltages. In addition, an external magnetic field can be applied to affect orbital motion and/or induce spin polarization. In this chapter, we provide an introduction to quantum transport in low-dimensional (2D, 1D and 0D) systems.

3.1.1 Quantum confinement and energy discretization

As an introduction to low-dimensional systems, let us start by deriving the carrier density $n_d = N_d/(L)^d$, where N_d is the total number of states in a d-dimensional system with a length L and $d = 1, 2, 3$ is the dimensionality (for simplicity, the length for each dimension are defined to be same). At zero temperature, all the states below Fermi energy $E_F = \hbar^2 k_F^2/2m$ are occupied and therefore n_d can be derived by considering, in reciprocal space, the length (d=1), area (d=2) or volume (d=3) and the approximated density of states $(\pi/L)^{-d}$,

$$n_d = \frac{N_d}{(L)^d} \sim \frac{2}{(L)^d} \int\limits_{0 \leq |\boldsymbol{k_d}| \leq |\boldsymbol{k_d^F}|} \frac{dk^d}{2^d(\frac{\pi}{L})^d} = \frac{|\boldsymbol{k_d^F}|^d}{d\pi} \tag{3.1}$$

where $\boldsymbol{k_F^d}$ is Fermi wave number in the d dimension. The factor of 2 in front of the integral is due to spin degeneracy and the one in the integral is due to double-counting of states for $\pm k$. The 2D density $n_2 = k_F^2/2\pi$ is often used to estimate k_F (Ch. 4).

The detailed properties of low-dimensional structures reflect the symmetry of the confinement potential. The shape of the potential well is important in determining the energy level spacing and the spatial distribution of the confined wavefunctions. For example, as discussed in the previous chapter, Rashba SOI depends on the electric field, i.e. on the spatial derivative of the QW potential. The potential profile along z also determines the HH-LH mixing. Often the QW confinement can be casted into one of the

following three categories, depending on the shape of the confining potential along z: rectangular, parabolic, or triangular QWs. The corresponding Hamiltonians read:

$$H_{QW} = -\frac{\hbar^2}{2m}\frac{\partial^2}{\partial z^2} + V(z) \tag{3.2}$$

$$V(z) = \begin{cases} V_0\left[u(z-\frac{W}{2}) - u(-z-\frac{W}{2})\right] & \text{(Rectangular QW)}, \\ \frac{m\omega^2 z^2}{2} & \text{(Parabolic QW)}, \\ eEzu(z)\ ;\ x>0 & \text{(Triangular QW)} \end{cases}$$

where m is the effective mass of the carrier, W is the width of the rectangular QW, ω is an angular frequency given by the curvature of the parabolic quantum well, e is the electron charge, E is the electric field, $\hbar$ is the reduced Planck constant, $u(x)$ is the Heaviside step function and V_0 is the height of the QW. Often $V_0 \to \infty$ represents a good approximation for deep QWs, provided one considers only the first few subbands. Therefore, the n^{th} subband energy E_n is

$$E_n = \begin{cases} \frac{\hbar^2}{2m}(\frac{\pi n}{L})^2 & \text{(Infinite rectangular QW)}, \\ \hbar\omega(n+\frac{1}{2}) & \text{(Parabolic QW)}, \\ -(\frac{e^2E^2\hbar^2}{2m})^{\frac{1}{3}}a_n & \text{(Triangular QW)} \end{cases} \tag{3.3}$$

where $a_n \sim -1/4 * [3\pi(8n-1)]^{2/3}$. Here, only triangular QW breaks the inversion symmetry of the system, which results in Rashba SOI.

In order to observe low-dimensional transport, the thermal energy $E_{th} \sim k_BT$, where k_B is Boltzmann constant and T is temperature, must be much smaller than the subband energy spacings. That is the reason why low effective mass favors quantum confinement (we note that in parabolic QW $\omega = \sqrt{\kappa/m}$, where κ is the force constant of the harmonic oscillator set by the electrostatic parabolic potential).

3.2 Magneto-transport in 2D quantum well

3.2.1 Classical Drude model and Hall effect

Hereafter, we shall derive fundamental theory for hole transport in low-dimensional systems (only hole transport is considered here since all our

devices discussed in this thesis are p-type). We consider that the sample temperature is low enough for holes to be regarded as a degenerate hole gas, meaning that only hole states at Fermi energy contribute to transport while hole states below the Fermi energy do not because they are always occupied.

At first, classical diffusive transport in 2D is described. In diffusive transport, holes are scattered during their motion due to different scattering sources, *e.g.*, impurities, phonons, other holes, etc. [80]. Hole diffusion can be parameterized by the scattering time τ_{tr}, the average time between scattering events. When electric field $\boldsymbol{E}$ and magnetic field $\boldsymbol{B}$ are applied to the system, the equation of motion for holes can be described using the Drude model:

$$\boldsymbol{F} = e(\boldsymbol{E} + \boldsymbol{v_{dr}} \times \boldsymbol{B}) - m\boldsymbol{v_{dr}}/\tau_{tr} \tag{3.4}$$

where $\boldsymbol{F}$ is the (average) force that a hole feels, $\boldsymbol{v_{dr}}$ is the drift velocity of the holes. In equilibrium, $\boldsymbol{F} = 0$, the holes will have constant $\boldsymbol{v_{dr}}$ and therefore, without $\boldsymbol{B}$,

$$\boldsymbol{v_{dr}} = \frac{e\tau_{tr}}{m}\boldsymbol{E} \equiv \mu\boldsymbol{E} \tag{3.5}$$

where $\mu = e\tau_{tr}/m$ is called (carrier) mobility. Substituting sheet current density $\boldsymbol{j} = en_s\boldsymbol{v_{dr}}$, mobility μ and out-of-plane magnetic field $\boldsymbol{B} = (0, 0, B_z)$ yields

$$\begin{pmatrix} E_x \\ E_y \end{pmatrix} = \begin{pmatrix} \rho_0 & -\frac{B_z}{en_s} \\ \frac{B_z}{en_s} & \rho_0 \end{pmatrix} \begin{pmatrix} j_x \\ j_y \end{pmatrix} \equiv \begin{pmatrix} \rho_{xx} & \rho_{xy} \\ -\rho_{xy} & \rho_{yy} \end{pmatrix} \begin{pmatrix} j_x \\ j_y \end{pmatrix} = \boldsymbol{\rho} \begin{pmatrix} j_x \\ j_y \end{pmatrix} \tag{3.6}$$

where $\rho_0 = (en_s\mu)^{-1}$ and $\boldsymbol{\rho}$ is sheet resistivity. Generally, the sheet conductivity is

$$\boldsymbol{\sigma} = \begin{pmatrix} \sigma_{xx} & -\sigma_{xy} \\ \sigma_{xy} & \sigma_{yy} \end{pmatrix} = \begin{pmatrix} \rho_{xx} & \rho_{xy} \\ -\rho_{xy} & \rho_{yy} \end{pmatrix}^{-1} \tag{3.7}$$

$$\sigma_{xx} = \frac{\rho_{xx}}{\rho_{xx}^2 + \rho_{xy}^2},\ \sigma_{xy} = -\frac{\rho_{xy}}{\rho_{xx}^2 + \rho_{xy}^2}. \tag{3.8}$$

and therefore,

$$\sigma_{xx} = \frac{\sigma_0}{1 + \mu^2 B_z^2},\ \sigma_{xy} = -\frac{\sigma_0 \mu B_z}{1 + \mu^2 B_z^2}. \tag{3.9}$$

where $\sigma_0 = en_s\mu$.

The Eq. 3.6 is useful to estimate the 2D density. Hall-bar devices such as the one shown in Fig. 3.1 (a) are often used to characterize two-dimensional transport. When current through the Hall bar $I_x \equiv I_{ds}$ is applied, longitudinal and transverse voltages $V_x \equiv V_{ch}$ and $V_y \equiv V_H$ yield the longitudinal resistance R_{xx} and Hall resistance R_{xy}, respectively, i.e.:

$$R_{xx} = \frac{V_{ch}}{I_{ds}} = \frac{E_x L}{j_x W} = \rho_0 \frac{L}{W},\ R_{xy} = \frac{V_H}{I_{ds}} = \frac{E_y W}{j_x W} = -\frac{B_z}{en_s} \tag{3.10}$$

where L and W are the channel length (in x direction) and the channel width (in y direction), respectively. By measuring V_H as a function of a relatively small B_z, one can obtain the sheet carrier density n_s from the slope of R_{xy} (Fig. 3.1 (c) at low B_z).

3.2.2 Shubnikov de Haas effect and Quantum Hall effect

What if the magnetic field is strong enough that the path of a hole makes a circle? According to quantum physics, quantized energy levels so-called Landau levels (LLs) are formed at high magnetic fields. In a simple description, the circular path without scattering ($l_{tr} = v_F\tau_{tr} \gg 2\pi v_F/\omega_c$, where l_{tr} is the mean free path, $v_F = \hbar k_F/m$ is Fermi velocity, and $\omega_c = eB_z/m$ is cyclotron frequency) requires the periodic boundary condition, making energy discrete. In this case, the (spin-less) 2D Hamiltonian H_{LL} under out-of-plane field B_z is, by use of Landau gauge $\boldsymbol{A} = (-B_z y, 0, 0)$,

$$H_{LL} = \frac{\left[(p_x + eB_z y)^2 + p_y^2\right]}{2m} = \frac{p_y^2}{2m} + \frac{m\omega_c^2 (y + y_0)^2}{2} \tag{3.11}$$

where $y_0 = \hbar k_x/eB_z = k_x l_B^2$. The H_{LL} has the same form as the Hamiltonian of a harmonic oscillator, leading to $E_{LL} = \hbar\omega_c(n + \frac{1}{2})$ where n is LL index. Here, we define the length scale of the channel in x direction to be L, yielding $k_x = m*2\pi/L$ for the periodic boundary condition (m is an integer number.). Therefore, in the channel, the state with a k_x in a LL (excluding the spin degeneracy) occupies a surface $\Delta(k_x l_B^2)*L = (2\pi/L)*l_B^2*L = 2\pi l_B^2$. In other words, the density of each LL equals $n_B = (2\pi l_B^2)^{-1}$. LLs below the Fermi energy E_F are filled so that the carrier density n_s is equal to the integer multiple of n_B: $n_s = \nu * n_B$. Hence, the number ν, so-called filling factor, indicates how many LLs are filled.

Charge transport in the quantum Hall regime occurs through edge channels formed by LLs crossing the Fermi energy[81, 80] (Fig. 3.1 (a) white

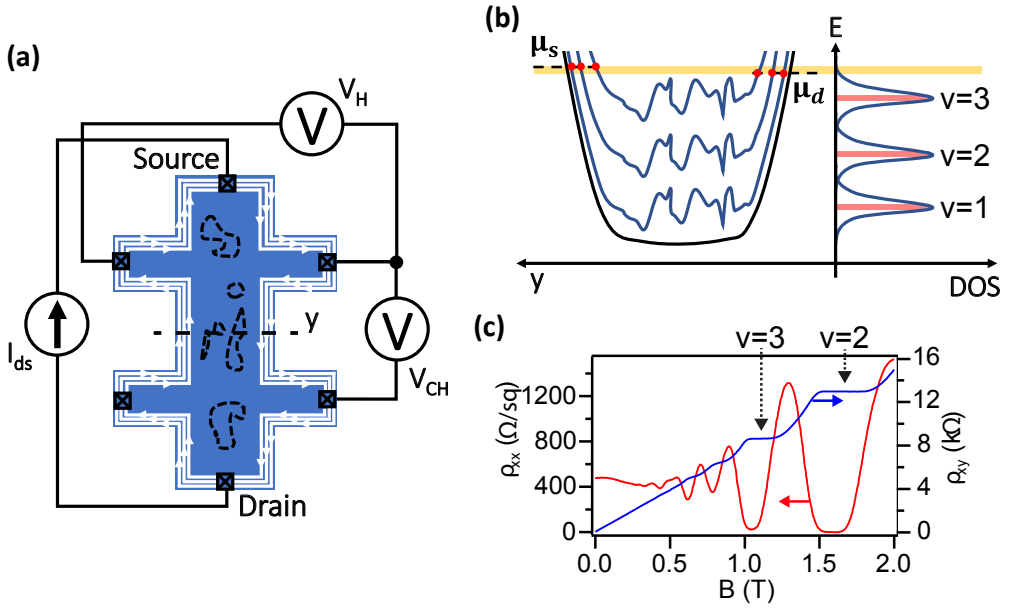

Figure 3.1: (a) Schematic of a Hall bar structure. This Hall bar structure has six ohmic contacts. Current I_{ds} flows from the source to the drain. In so-called Hall measurement, I_{ds}, transverse voltage V_H and longitudinal voltage V_{ch} are measured as a function of magnetic field. White lines indicates edge channels due to Landau levels (LLs). (b) The energies of the LLs in the transversal cross-section of the channel (dashed line in (a)). Each LL, with index ν, gives a peak in density of states (DOS) with extended states (colorized in red) separated by localized states. The latter are formed by potential fluctuations, *e.g.*, due to impurities or inhomogeneities in the QW thickness. Carriers can be captured there and move along close trajectories as schematically depicted by black dashed lines in (a). (c) In the linear regime (small applied bias voltage, i.e. $\mu_d \approx \mu_s$) the longitudinal resistivity ρ_{xx} exhibits oscillations as a function of an applied perpendicular magnetic field (red trace): ρ_{xx} has minima whenever a LL crosses the Fermi energy, and maxima when the Fermi energy lies in the region of localized states between adjacent LLs (the energy spacing between LLs increases with B_z). Quantized Hall resistance is observed in transverse resistivity (ρ_{xy} at high magnetic field (blue line). Simultaneously, ρ_{xx} tends to vanish. These are characteristic signatures of the Quantum Hall effect, and they denote the formation of ballistic edge channels. The data is taken from measurements of the Hall bar device described in Ch. 5.

lines). In fact, at the edges of the channel, the confinement potential raises

causing an upward bending of the LLs as shown in Fig. 3.1 (b). Holes flowing through an edge state cannot be back scattered since on the same side of the Hall bar all edge states move in the same direction (chirality of the edge states). In the absence of backscattering, transport is dissipationless. In such as case, each edge mode behaves as a ballistic one-dimensional channel with a conductance of the e^2/h (see next section). The voltage drop associated with this finite quantized conductance occurs at the the contacts, such that $V_{ch} \approx 0$ (hence $\rho_{xx} \approx 0$). The quantized conductance of the edge states emerges as a quantization of the transverse Hall resistance, which requires taking into account the edge states on the other side of the Hall bar, which flow in the reversed direction. In fact, the transverse voltage V_H measures the difference in the electrochemical potentials of the opposite edge modes, which are defined by the source and drain contacts, respectively. Therefore $V_H = V_{ds}$ and $R_{xy} = h/\nu e^2$. This effect is the characteristic manifestation of the quantum Hall effect (QHE) (Fig. 3.1 (c) blue line at high magnetic fields).

More generally, the carriers in LLs move perpendicularly to the gradient of the potential including charge impurities. Holes are captured in energy minima making closed loops (see closed dashed lines in Fig. 3.1 (a)) when the Fermi energy lies well between adjacent LLs (Fig. 3.1 (b)). On the other hand, at relatively small magnetic fields, the loops tend to be rather delocalized which facilitates hole scattering from one loop to another. When the Fermi energy approaches a LL (red lines in Fig. 3.1 (b)), transport paths going from one edge to the other become accessible owing to the enlarging contour of the loops and a finite resistivity due to dissipative diffusive paths can be observed. As a result, the longitudinal resistivity ρ_{xx} oscillates in magnetic field, a phenomenon known as Shubnikov-de Haas (SdH) oscillations (see Fig. 3.1 (c) ρ_{xx} (red line)). The SdH peaks correspond to the the Fermi energy crossing the LLs. Therefore one can estimate the carrier density from the frequency of the SdH oscillations in reciprocal magnetic field.

3.2.3 Weak anti-localization effect

SdH oscillations dominate transport at moderate magnetic fields. Close to zero magnetic field, other quantum effects can become prominent. One of them is a phenomenon known as weak anti-localization (WAL), which is a quantum interference effect occurring in the diffusive transport regime. When charge carriers diffusive from point a to b, they can follow many different paths, associated with different sequences of scattering events. Each path has a complex amplitude A, whose squared modulus corresponds to

the probability that the carrier takes that particular path. The number and extension of all the possible paths is limited by the phase coherence relaxation time τ_ϕ, that is the average time between phase-relaxation events. For simplicity, we assume that there are only two paths and therefore the total probability P_{ab} of going from a to b is

$$P_{ab} = |A_1 + A_2|^2 = |A_1|^2 + |A_1|^2 + 2|A_1||A_2|\cos(\phi_1 - \phi_2) \tag{3.12}$$

where A_i is the amplitude for path i ($i = 1, 2$), and ϕ_i is the phase of A_i. On the right hand side of Eq. 3.12, the first two terms are the same as the classical probability of going from a to b through path 1 or through path 2. The last term accounts for the quantum interference between the two paths. When the number of paths increases, the interference terms cancel out because each path can have an arbitrary phase. However, in a closed loop (where a and b coincide), two time-reversed paths can have exactly the same phase. This case is exemplified In Fig. 3.2 (a), where a possible diffusive path with the shape of a closed loop is shown. An electron (or a hole) can go through the path clockwise or anti-clockwise (red and blue lines). The two time-reversed paths have the same phase, which maximizes their interference. This effect, called weak localization (WL), translates into an increased probability of coming back to the starting point, i.e. of remaining localized. WL provides a quantum correction to Drude conductivity $\Delta\sigma_{xx}$ (Fig. 3.2 (b)). The WL effect is destroyed by an out-of-plane magnetic field which breaks time reversal symmetry introducing a trajectory-dependent dephasing. As a result, the WL effect manifests itself as a zero-bias magnetoresistance peak.

RSOI can also break WL. RSOI is responsible for an effective magnetic field which depends on the wavevector and the local electric fields all along a given path. In the case of two self-interfering paths as in Fig. 3.2 (a), the spin rotation induced by RSOI will be opposite for clockwise and anti-clockwise trajectories, thereby resulting in a destructive interference and hence a conductivity peak at zero magnetic field (like in the case of WL, a finite magnetic field breaks WAL). Usually, the magnetic field required to break WAL is smaller than the one causing the suppression of WL. Therefore the quantum correction to conductivity displays a zero-field WAL peak within a wider dip due to WL, also centered at zero magnetic field (Fig. 3.2 (c)).

Iordanski *et al.* [82] derived the conductivity correction for the 2D system with the k-linear and k-cubic SOI (without Zeeman effect), which enabled us to extract important parameters for spintronic devices: phase re-

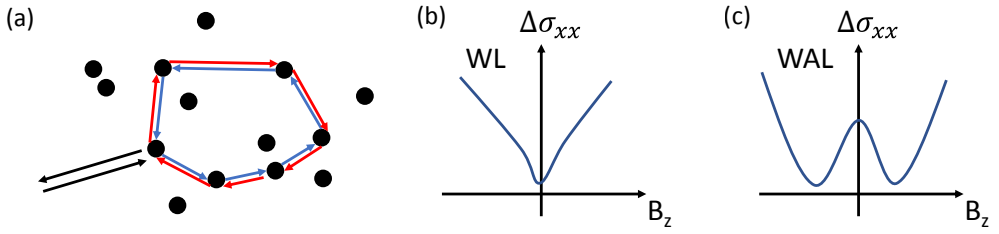

Figure 3.2: (a) Scattering centers (black dots) and two time-reversed paths forming a closed loop (starting from the black arrow, passing through clockwise (red) or anticlockwise (blue) path and going out along the other black arrow). (b) Two paths interfere with each other constructively because of no phase difference, resulting in the reduction of longitudinal conductivity of the system (weak localization, WL). Out-of-plane magnetic field B_z makes a phase difference between the time-reversed paths and destroys the WL, recovering the conductivity. (c) A phase difference due to SOI can also break the WL (weak anti-localization, WAL). The SOI effect can also be broken by B_z when, simply speaking, the cyclotron motion becomes much smaller than spin relaxation length due to the SOI. Usually, this SOI effect is broken by smaller magnetic fields than the ones breaking WL. Therefore a WAL conductivity peak appears around $B_z = 0$ inside a WL conductivity minimum. .

laxation time, spin relaxation time due to SOI, and spin splitting energy at zero field (Ch. 4).

3.3 Ballistic transport through a 1D wire

3.3.1 Conductance quantization

In a 2D electron (or hole) gas, 1D quantum confinement can be obtained by applying voltages to two split gates on the surface of the heterostructure. When the channel width is comparable to the Fermi wavelength $\lambda_F = 2\pi/k_F$, the electronic states get quantized forming a 1D conduction channel. In the case of ballistic 1D transport, the conductance is quantized in units of e^2/h, the so-called quantum of conductance. We explain this using a simple model. We assume that drain and source contacts are connected to the 1D channel, and we neglect interactions and spin effects, except for spin degeneracy. We also assume that the channel has a single quadratic energy dispersion. The current through the channel is obtained by integrating the current density $j = evn$

$$I_{1D} = \int_{n_s^F}^{n_d^F} ev(n_l) dn_l \tag{3.13}$$

where v is the velocity of holes and $n_{d/s}^F$ is the hole density at Fermi energy in the drain (source), $\mu_{d/s}$. The states below the lower Fermi energy are always occupied and therefore only the states between the Fermi levels of the source and drain contacts contribute to I_{1D}.

Remembering the relation that $n_{1D} = k/\pi$ (Eq. 3.1) and using the relation for the group velocity of a particle $v = \hbar k/m$, we obtain that

$$I_{1D} = \int_{k_s^F}^{k_d^F} e\frac{\hbar k}{m}\frac{dk}{\pi} = 2\frac{e^2}{h}(V_d - V_s) \tag{3.14}$$

where we have used $\mu_{d/s} = \hbar^2(k_{d/s}^F)^2/2m = eV_{d/s}$ and $V_{d/s}$ is the voltage applied to the drain/source. Therefore, the above equation yields the 1D quantized conductance

$$G_{1D} = 2\frac{e^2}{h}. \tag{3.15}$$

The factor of two indicates the spin degeneracy which is included in Eq. 3.1. Note that the conductance is independent of the specific parameters of the 1D system.

Several subbands can participate in the transport (Fig. 3.3 (a)). For a small $eV_{ds} = \mu_d - \mu_s$, the conductance is determined by the number of channels that cross the Fermi levels μ_d and μ_s, the same for QHE. Therefore, one can observe conductance steps as the energy levels are lowered by gate voltage V_g and pass the Fermi level one by one, see Fig. 3.3 (b) blue solid line. On the other hand, at higher V_{ds}, the conductance plateaus with half value between two adjacent plateaus appear [83].

The conductance steps between consecutive plateaus are broadened by temperature [80] and, in the case of short channels, by tunneling (Fig. 3.3 (b) yellow dashed line).

3.3.2 Magnetic field effect

Magnetic fields lift the spin degeneracy, resulting in half conductance plateaus at multiple of e^2/h in a 1D channel. Additionally, if the field is applied perpendicular to the QW plane (i.e. along z), it affects the lateral confinement and hence have a strong orbital effect eventually leading to the formation of quantum-Hall edge states. Starting from the 2D Hamiltonian, we write a Hamiltonian for a 1D channel with a parabolic confinement under out-of-plane magnetic fields B_z:

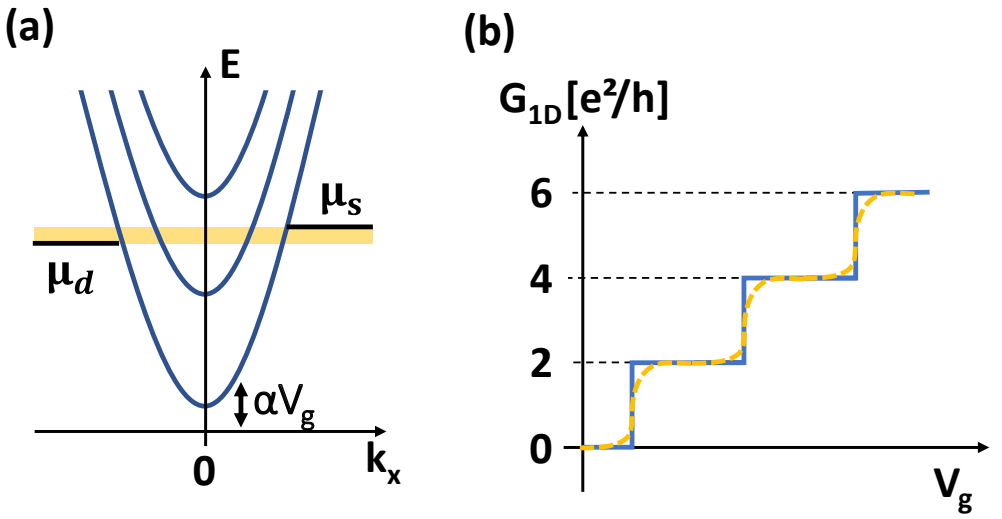

Figure 3.3: (a) Energy subbands of a quasi 1D system, where several 1D channel exist in a 1D constriction. In a simple model, each 1D subband has a parabolic energy dispersion. The energy offset can be shifted by gate voltage V_g. (b) 1D channel conductance G_{1D} as a function of V_g. Step-like conductance appears (blue solid line). Thermal energy and tunneling effect across the 1D constriction broaden the plateaus (orange dashed line).

$$\begin{aligned} H_{1D} &= \frac{\left[(p_x + eB_z y)^2 + p_y^2\right]}{2m} + \frac{m\omega_0^2 y^2}{2} + \frac{1}{2}g^*\mu_B B_z \sigma_z \\ &= \frac{p_x^2}{2m} + \left[\frac{p_y^2}{2m} + \frac{\omega_c y p_x}{m} + \frac{m\omega^2 y^2}{2}\right] + \frac{1}{2}g^*\mu_B B_z \sigma_z \\ &= \frac{p_x^2}{2m} * (1 - \frac{\omega_c^2}{\omega^2}) + \left[\frac{p_y^2}{2m} + \frac{m\omega^2}{2}(y + \frac{\omega_c p_x}{m\omega^2})^2\right] + \frac{1}{2}g^*\mu_B B_z \sigma_z \end{aligned} \quad (3.16)$$

where we have used the Landau gauge $\boldsymbol{A} = B_z y\hat{x}$, Landé g factor g^* and $\omega^2 = \omega_0^2 + \omega_c^2$. The terms enclosed by square brackets have the form of the 1D Hamiltonian of a harmonic oscillator Eq. 3.2. Therefore the energy dispersion of n^{th} subband (more precisely of its edge at $p_x = \hbar k_x = 0$) is

$$E_n^{1D}(B_z) = \hbar\omega(n + \frac{1}{2}) + \frac{1}{2}g^*\mu_B B_z. \quad (3.17)$$

The resulting subband energies as a function of B_z are shown in Fig. 3.4. They exhibit a hyperbolic dependence as opposed to the linear one expected for in-plane magnetic fields, for which orbital effects are weak. This field

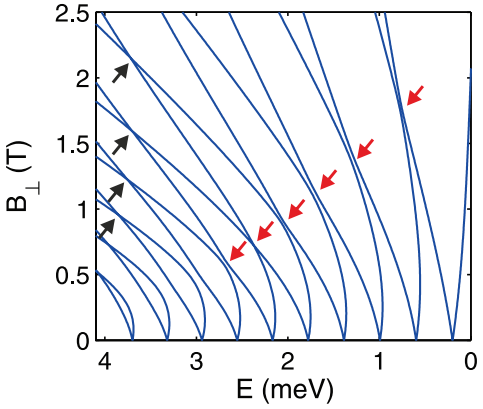

Figure 3.4: Results of a numerical simulation showing the subband energies of a 1D channel with a k-cubic RSOI as a function of perpendicular magnetic field. In practice, each blue line corresponds to the edge of a conductance plateau. Therefore, in the white areas between two adjacent lines the conductance is a multiple of e^2/h. The magnetic field splits each zero-field conductance plateau due to the Zeeman effect. Red (black) arrows emphasize anti-crossings (crossings) of subbands. This figure is reproduced from Ref. [84].

dependence of Fig. 3.4 can be experimentally probed by measuring G vs V_g and B_z because E_n^{1D} correspond to the edge of n^{th} plateau and can be controlled by gate voltage V_g. At high B_z such that $\omega_c \gg \omega_0$, H_{1D} tends to H_{LL}. As seen in the first term in Eq. 3.16, magnetic fields seem to increase the mass of the holes in the 1D channel, making the energy dispersion flatter. In the limit that $\omega_c \to \infty$, $\omega \sim \omega_c$, meaning that LLs are formed in the channel.

3.4 Single hole transport through a quantum dot

3.4.1 Constant interaction model

Electrostatic confinement in all directions can result in a small area of a 2D electron (or hole) gas surrounded by potential barrier, thereby defining a so-called quantum dot (QD). In the QD, energy is fully quantized in discrete energy levels. In addition, Coulomb interactions reflecting the repulsion among carriers with the same charge can become important. The Coulomb interaction results in an energy cost for adding an extra charge to the QD. As a result, the number of charges N confined to a QD becomes a well-defined integer. The energy levels are described by the constant interaction model in which three assumptions are made [85]. First, N can be controlled by a gate voltage V_g with constant gate coupling capacitance C_g. Second,

constant QD capacitance C_Σ. Third, the single-particle energy spectrum E_n is not affected by Coulomb interactions. Consequently, the energy levels in a QD $E^{QD}(N, V_g)$ are

$$E^{QD}(N, V_g) = \frac{(eN + C_g V_g)^2}{2C_\Sigma} + \sum E_n. \tag{3.18}$$

The first term on the right-hand side is an electrostatic energy, where $|eN|$ is the total charge of the N holes confined in the QD, and $C_g V_g$ is the charge induced by V_g. Then, the energy required to add one hole to a QD with $(N-1)$ holes, i.e. electrochemical potential $\mu(N, V_g)$, reads

$$\mu(N, V_g) = E^{QD}(N, V_g) - E^{QD}(N-1, V_g) = (N - \frac{1}{2})\frac{e^2}{C_\Sigma} + \alpha V_g + \Delta E_N \tag{3.19}$$

where $\alpha = eC_g/C_\Sigma$ is the so-called lever-arm parameter relating V_g variations to energy variations, and $\Delta E_N = E_N - E_{N-1}$ is the energy level spacing. We shall define as addition energy, E_{add}, the shift in electrochemical potential, following the addition of an extra hole to the QD, i.e.

$$E_{add} \equiv \Delta\mu = \mu(N, V_g) - \mu(N-1, V_g) = \frac{e^2}{C_\Sigma} + \Delta E_N = E_c + \Delta E_N. \tag{3.20}$$

In the above equation we have introduced the Coulomb charging energy $E_c \equiv \frac{e^2}{C_\Sigma}$. When $\Delta E_N \approx 0$ (case of a metallic dot), $\Delta\mu \approx E_c$ for all occupation numbers N.

Current transport through a QD can be measured by connecting to carrier reservoirs via tunnel barriers. At low temperature ($k_B T \ll E_c$) and low bias voltage ($eV_{ds} \ll E_c$), charges can only flow one by one, a phenomenon know as single-electron (or single-hole) tunneling. This one-by-one occurs only when the electrochemical potential of the QD, $\mu(N, V_g)$, lies in the source-drain bias window, in which case the occupation of the QD will fluctuate between $N-1$ and N. Otherwise, transport is blocked by the Coulomb charging energy, a regime known as "Coulomb blockade". In the linear regime, i.e. for $eV_{ds} \sim k_B T \ll E_c$, sweeping the gate voltage will then result in a sequence of conductance peaks (one every time $\mu_d < \mu(N, V_g) < \mu_s$, where μ_s and μ_d are the Fermi energies of the source and drain reservoir, respectively), separated by Coulomb-blockade regions of suppressed conductance (Fig. 3.5 (a)). The line width of the Coulomb peaks is dominated by largest energy scale between the thermal energy ($\sim k_B T$) and the life-time broadening due to tunnel coupling to the source and drain

reservoirs ($\hbar\Gamma$, where Γ is the sum of the tunnel rates to the source and drain reservoirs).

At large source-drain bias voltage $eV_{ds} > E_c$ the Coulomb blockade effect is lifted, and current is allowed to flow for every value of the gate voltage. A qualitative color map of the QD conductance, G_{QD}, as a function of V_{ds} and V_g is shown in Fig. 3.5 (c). It shows that Coulomb blockade occurs within diamond-shape regions in which the occupation of the QD is a constant integer number.

3.5 Conclusion

This chapter was devoted to the discussion of low-dimensional transport in a variety of different regimes, going from 2D magneto-transport to ballistic 1D conduction and 0D Coulomb blockade regime. Except for this last case, interaction effects among carriers were ignored. In fact, interaction effects are naturally expected to emerge in closed nano-scale systems such as QDs, where small numbers of charges are forced to coexist within same small volume. Charge interactions in QDs can be exploited in a variety of applications, ranging from metrology (single-electron pumps, quantum-dot thermometers) to spin qubits (here interactions not only favor the necessary confinement of electrons, but also provide an opportunity for two-qubit operations, e.g. mediated by the exchange coupling between adjacent QDs). On the other hand, interactions generally tend to vanish in open systems (2D and 1D). There exist regimes, however, where the presence of charge interactions can be subtle and, in fact, more influential than expected. It is the case of the so-called 0.7 anomaly observed in 1D quantum point contacts. This ubiquitous phenomenon consists in the emergence of a small conductance plateau at around $0.7 \times (2e^2/h)$. It can not be explained on the basis of the simple model presented in section 3.3.1. While a conclusive explanation of this phenomenon has not been reached yet, several theories suggest it could arise from local electron-electron interactions, and, possibly, Kondo physics. Finally, we have seen that the spin-orbit interaction can have different manifestations depending on the system dimensionality and transport regime. It can give rise to the WAL phenomenon in diffusive 2D transport (which is the focus of the experiment presented in Ch. 4), or produce level anti-crossings in 1D and 0D systems, as shown in Fig. 3.4 (this phenomenology was not clearly observed in this PhD thesis and it could be the subject of follow-up studies).

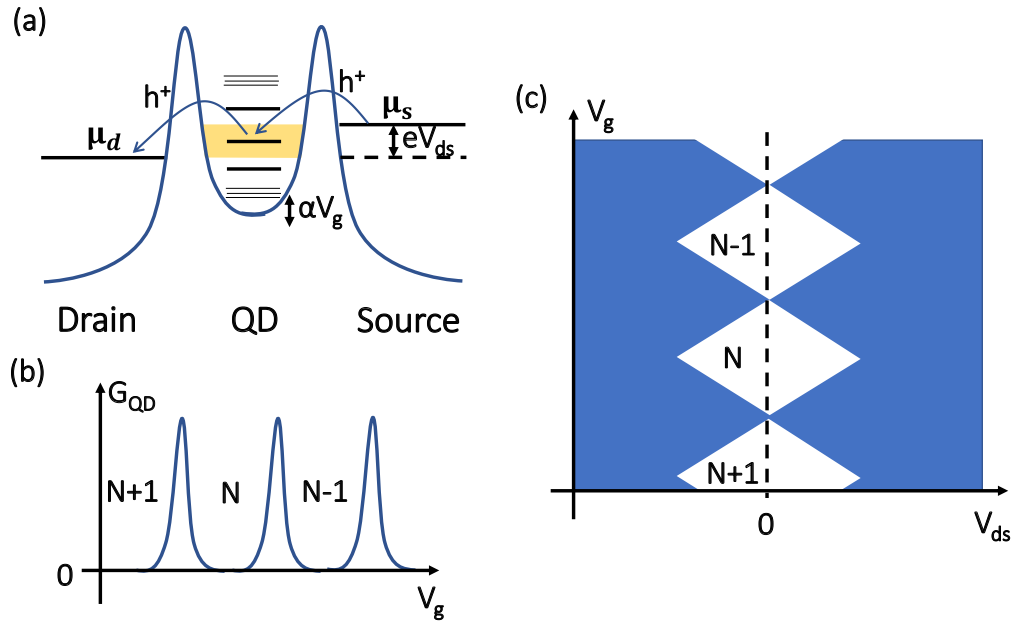

Figure 3.5: (a) Schematic energy diagram of a drain-QD-source system. The valence band is flipped for visibility. Two reservoirs (Drain and Source) are connected to a QD across tunnel barriers. Energy levels in QD is quantized by quantum confinement and Coulomb interaction. Current through the QD is allowed when a QD level (i.e. a QD electrochemical potential $\mu(N, V_g)$) lies in the bias window (yellow area) between the Fermi levels μ_D and μ_S of the reservoirs. On the contrary, when no QD level is in the bias window, no current flows (Coulomb blockade regime) and the number of holes in the QD is fixed. (b) The energy levels in the QD can be varied by a gate voltage V_g and a peak in the conductance G_{QD} appears every time a QD level passes through the bias window. (c) When the QD conductance is measured as a function of V_{ds} and V_g, a characteristic set of diamond-shape regions (white color) is observed where $G_{QD} \approx 0$. Outside these regions, Coulomb blockade is everywhere lifted leading to a finite G_{QD} (blue color).

Chapter 4

Weak anti-localization in Ge-surface heterostructure

4.1 Introduction

In this chapter, we report a magneto-transport study of a two-dimensional hole gas confined to a strained Ge quantum well grown on a relaxed $Si_{0.2}Ge_{0.8}$ virtual substrate. The conductivity of the hole gas measured as a function of a perpendicular magnetic field exhibits a zero-field peak resulting from weak anti-localization. The peak develops and becomes stronger upon increasing the hole density by means of a top gate electrode. This behavior is consistent with a Rashba-type spin-orbit coupling whose strength is proportional to the perpendicular electric field, and hence to the carrier density. In the low-density, single-subband regime, by fitting the weak anti-localization peak to an analytic model, we extract the characteristic transport time scales and a spin splitting energy $\Delta_{SO} \sim$1 meV. Tight-binding calculations show that Δ_{SO} is dominated by a cubic term in the in-plane wave vector. Finally, we observe a weak anti-localization peak also for magnetic fields parallel to the quantum well and associate this finding to an effect of intersubband scattering induced by interface defects.

4.2 Ge-surface heterostructure

The strained SiGe heterostructure was grown on a 200 mm Si(001) substrate by means of reduced pressure chemical vapor deposition (RP-CVD). Growth was realized using an industrial-type, mass-production system (ASM Epsilon 2000 RP-CVD), which is a horizontal, cold-wall, single wafer, load-lock reactor with a lamp-heated graphite susceptor in a quartz

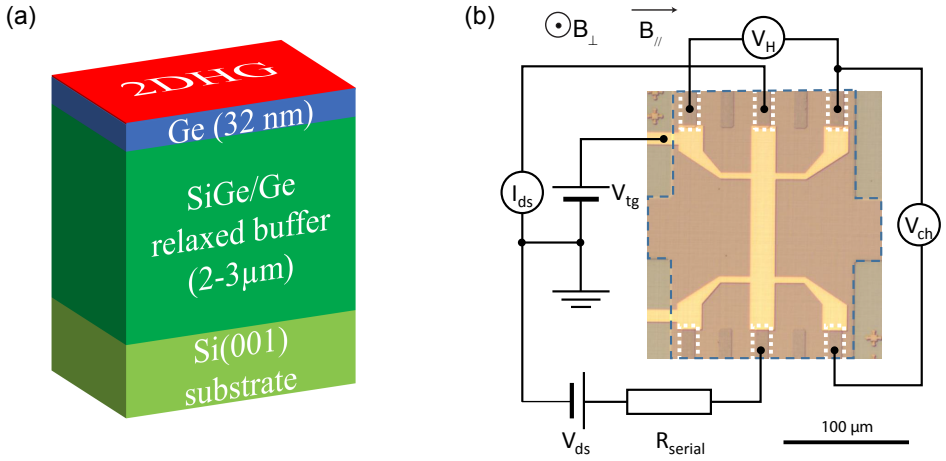

Figure 4.1: (a) Schematic of the heterostructure. (b) Optical image of the Hall bar devices. The blue line highlights the mesa and the white dotted lines the Pt contacts. We measure the transverse Hall voltage (V_H) and the longitudinal channel voltage (V_{ch}) from which we extract Hall resistivity and channel resistivity respectively. The directions of the applied fields $B_\perp$ and $B_{/\!/}$ are also indicated.

tube. RP-CVD offers the major advantage of unprecedented wafer scalability and is nowadays routinely used by leading companies in the semiconductor industry to grow epitaxial layers on Si wafers of up to 300 mm diameter. The heterostructures, shown schematically in Fig. 4.1.a, consists of a 3 µm thick reverse linearly graded, fully relaxed $Si_{0.2}Ge_{0.8}$/Ge/Si(001) virtual substrate with a 32-nm-thick strained Ge QW surface layer. This is a typical design for surface channel structures employed in modern MOSFET devices. The full structure was grown in a single process without any external treatment. The surface of the Si wafers was cleaned by an in situ thermal bake in H_2 ambient at high temperature, above 1000°C. The Ge epilayer was grown from a commercially available and widely used germane (GeH_4) gas precursor at a relatively low substrate temperature (<450°C), as it is known that the growth temperature of the compressively strained Ge epilayers has to be sufficiently low to suppress surface roughening and retain compressive strain in the epilayers. Further details of materials growth and characterization are described elsewhere [86].

4.3 Device fabrication

The studied devices have a Hall-bar geometry defined by a top-gate electrode operated in accumulation mode (Fig. 4.1.b). Due to the absence of intentional doping, the Ge QW contains no carrier at low temperature. Only by applying a sufficiently negative top-gate voltage, V_{tg}, can the accumulation of a 2DHG be induced in the Ge QW. Device fabrication involves several steps that we discuss here briefly (more details on the fabrication steps highlighted in **bold font** are given in Appendix A). After receiving the heterostructure wafers from Warwick Univ., a **sample cleaning** procedure is initially performed. Then, each wafer is cut in 2cm-by-2cm chips after coating it with photo-resist for protection. Later, the obtained chips are processed one by one. As a first step, alignment marks are defined by **photolithography** and **electron beam evaporation** of Ti/Au = 10 nm/50 nm. A relatively large (tens of microns wide), 55-nm-thick mesa structure is defined by optical lithography and **reactive ion etching** in Cl_2 plasma. Ohmic contacts are successively fabricated using optical lithography, followed by Ar etching (to remove the residual oxide and photo-resist residues) and Pt deposition in an e-beam evaporator system. Next, 30 nm of Al_2O_3 are deposited all over the chip surface using **ALD** at 250°C. At this stage, the chips are cut in 5mm-by-5mm squares to be processed later one by one. This split was done in order to enable the realization of gate structures with different geometries. For the sake of the experiments discussed in this chapter, a Hall-bar-shape top gate electrode was defined by **EBL** and deposition of Ti/Au (10nm/50nm). This thickness exceeds the height of the mesa structures.

4.4 WAL under out-of-plane magnetic field

4.4.1 Carrier density and mobility

Magneto-transport measurements were performed in a ^{3}He cryostat with a base temperature of 300 mK. In a first set of experimental runs, longitudinal (ρ_{XX}) and Hall (ρ_{XY}) resistivities were measured as a function of magnetic field, $B_\perp$, perpendicular to the 2DHG, and V_{tg}. The onset of hole accumulation was found to occur at $V_{tg} \approx -4$ V, slightly varying from one run to the other. Examples of $\rho_{XX}(B_\perp)$ and $\rho_{XY}(B_\perp)$ traces are given in Fig. 4.2.a. From Hall resistivity we extracted the hole mobility (μ) and carrier density (n_{hole}) ranging from 800 to 4100 cm^2/Vs and from 1.3 to 2.8 $\times 10^{11}$ cm^{-2}, respectively (data points from two experimental runs are

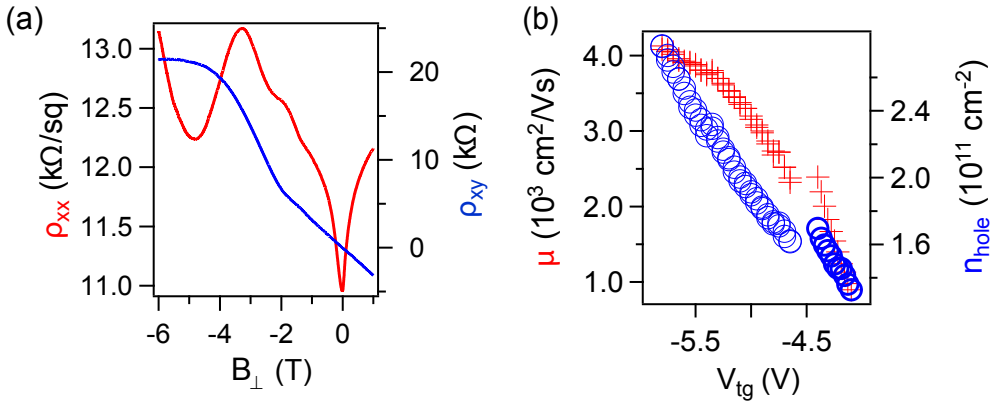

Figure 4.2: (a) Channel resistivity ρ_{XX} (red) and Hall resistivity ρ_{XY} (blue) as a function of out of plane magnetic field at V_{tg} = -4.8 V. Channel resistivity shows a dip at low field which is a signature of weak anti-localization. (b) Mobility μ (red) and carrier density n_{hole} (blue) as a function of accumulation gate voltage V_{tg}. Data points above and below $V_{tg} = -4.5V$ refer to two distinct experimental runs.

shown in Fig. 4.2.b). The mobility is much lower than the one reported in other strained Ge heterostructures [87]. This difference is likely due to the presence of charge traps at the Ge/Al_2O_3 interface.

Following basic Hall-effect characterization we now turn to a more in-depth investigation of the magneto-transport properties. In Fig. 4.2.a, the longitudinal resistivity (red trace) exhibits a pronounced dip at zero magnetic field. Such a dip is a characteristic signature of weak anti-localization (WAL), a mesoscopic phenomenon associated with spin-orbit coupling [88]. At zero magnetic field the latter leads to a suppressed enhancement of backscattering resulting in a resistivity minimum. This quantum interference effect is suppressed by a magnetic field perpendicular to the 2DHG, accounting for the observed resistivity dip at $B_\perp = 0$.

This phenomenon is further investigated in Fig. 4.3.a, where the longitudinal conductivity is now plotted as a function of $B_\perp$ and for a range of V_{tg} values, after having removed the feature-less back-ground contribution from classical Drude conductivity. As a matter of fact, $\Delta\sigma_{WAL}$ represents the quantum correction resulting from WAL. Interestingly, this data set shows that the WAL peak develops and broadens upon increasing V_{tg} and, correspondingly, the perpendicular electric field and the hole density n_{hole} in the QW. All over the n_{hole} range spanned, the 2DHG occupies the first subband only, as confirmed below by self-consistent tight-binding (TB) calculations

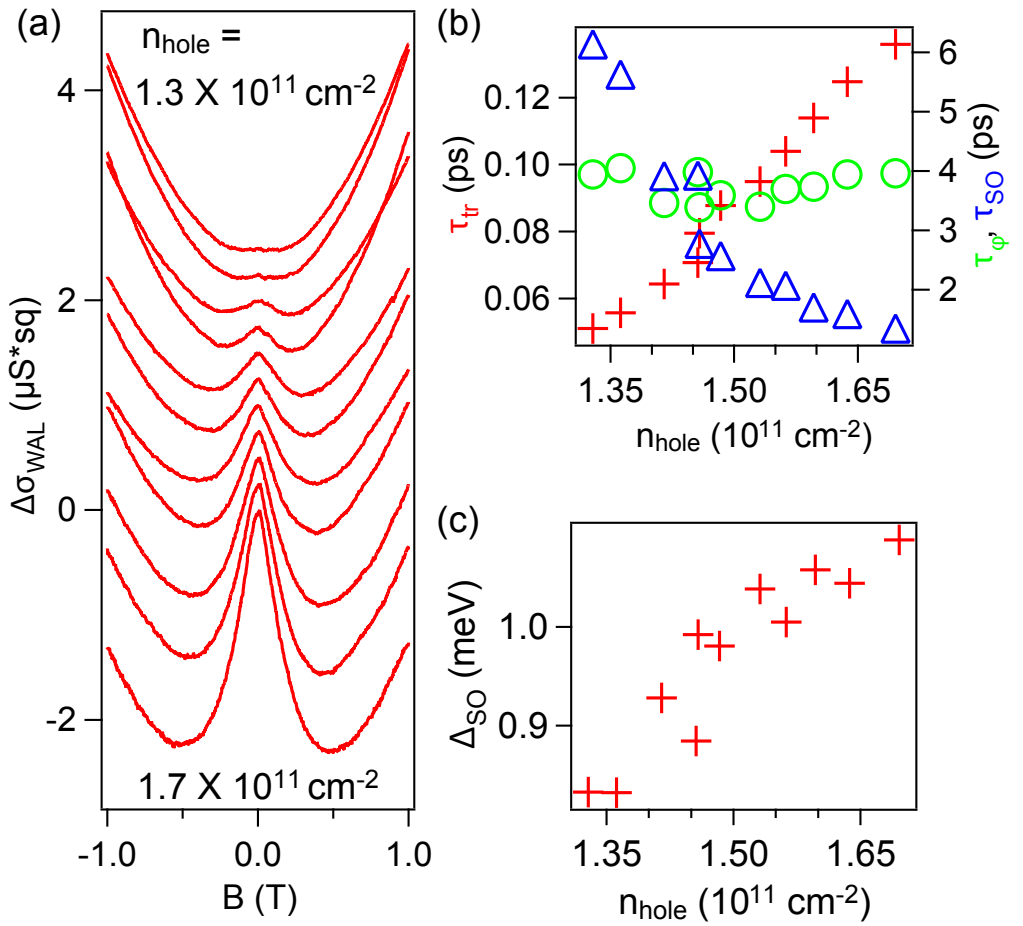

Figure 4.3: (a) Traces of the weak anti-localization contribution to the channel conductivity $\Delta\sigma_{WAL}$ as a function of $B_\perp$ for different accumulation gate voltages and carrier densities from $1.3 \times 10^{11}\,\mathrm{cm}^{-2}$ (top trace) to $1.7 \times 10^{11}\,\mathrm{cm}^{-2}$ (bottom trace, traces are offset for better visibility). The weak anti-localization peaks emerges as carrier density is increased. (b) Evolution of scattering time τ_{tr} (red crosses), phase relaxation time τ_φ (green circles) and spin relaxation time τ_{SO} (blue triangles) as a function of carrier density. (c) Evolution of the spin splitting energy Δ_{SO} as a function of carrier density.

[89].

The evolution of the WAL peak in Fig. 4.3.a suggests that the underlying spin-orbit coupling is gate tunable. We expect it to be of a Rashba-type since Dresselhaus spin-orbit coupling terms should be negligible due to the existence of bulk inversion symmetry in the Ge QW and surface roughness

[90]. The WAL peak can be fitted to the formula [82]:

$$\begin{aligned}\Delta\sigma_{WAL}(B_\perp) = \frac{e^2}{2\pi^2\hbar}\{&\Psi(\frac{1}{2}+\frac{B_\varphi}{B_\perp}+\frac{B_{SO}}{B_\perp}) \\ &+\frac{1}{2}\Psi(\frac{1}{2}+\frac{B_\varphi}{B_\perp}+2\frac{B_{SO}}{B_\perp})-\frac{1}{2}\Psi(\frac{1}{2}+\frac{B_\varphi}{B_\perp}) \\ &-\ln(\frac{B_\varphi}{B_\perp}+\frac{B_{SO}}{B_\perp})-\frac{1}{2}\ln(\frac{B_\varphi}{B_\perp}+\frac{2B_{SO}}{B_\perp})+\frac{1}{2}\ln(\frac{B_\varphi}{B_\perp})\}\end{aligned} \quad (4.1)$$

where $\Psi(X)$ is the digamma function, B_φ is the phase coherence field and B_{SO} is the characteristic field associated with the Rashba spin orbit coupling. From the fitting parameters B_φ and B_{SO} we can extract the phase coherence time τ_φ and the spin relaxation time τ_{so} with $\tau_i = m^*/4\pi\hbar\mu n_{hole}B_i$, i being either φ or SO. We note that the large width of the observed WAL peak is consistent with the relatively small values obtained for the scattering time ($\tau_{tr} = m^*\mu/e$).

4.4.2 Spin relaxation mechanisms

These values, as well as those for τ_φ, τ_{SO} are displayed as a function of carrier density in Fig. 4.3.b. The evolution of these characteristic time scales with respect to n_{hole} provides a hint on the underlying mechanism for spin relaxation. If spin relaxation was due to impurity scattering (Elliot-Yafet mechanism [91, 92]), then τ_{SO} should increase with τ_{tr} and decrease with the carrier density ($\tau_{so} \propto \tau_{tr}/n_{hole}^2$). This does not correspond to the observed trend. On the other hand, if spin relaxation occurred in between scattering events, due to spin-orbit-induced rotation (Dyakonov-Perel mechanism [93]), the spin relaxation time should decrease with τ_{tr} and with the spin splitting energy Δ_{SO} ($\tau_{so} \propto 1/(\tau_{tr} \times \Delta_{SO}^2)$). Our experimental finding is consistent with this second scenario, which allows us to deduce the spin splitting energy, $\Delta_{SO} \sim \hbar(2\tau_{so}\tau_{tr})^{-1/2}$, and its dependence on n_{hole} (see Fig. 4.3.c). The obtained values of Δ_{SO} are around 1 meV, i.e. a few times larger but still comparable to those reported for similar heterostructures and different experimental methods [94, 75, 95].

4.4.3 Self-consistent tight binding calculation

Fig. 4.4.a shows the valence-band profile calculated for $n_{hole} = 1.5 \times 10^{11}\,\mathrm{cm}^{-2}$, as well as a representation of the first two hole subbands. From the in-plane dispersion of the first subband (not shown), we obtain an in-plane effective mass $m^* = 0.07m_0$, where m_0 is the bare electron mass. This

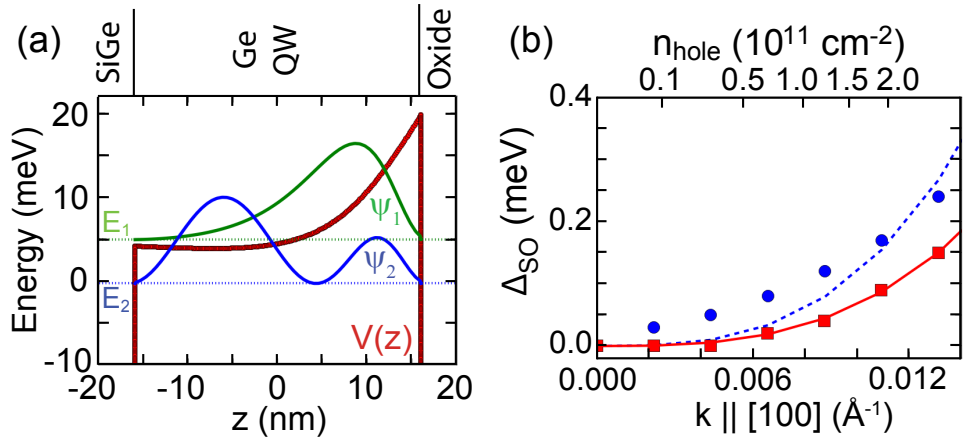

Figure 4.4: (a) Valence band diagram and squared wave functions of the first two hole subbands calculated for $n_{hole} = 1.5 \times 10^{11}\,\mathrm{cm}^{-2}$. The Fermi energy is $E_F = 0$. (b) Spin splitting energy calculated with a TB model, with and without interface roughness (squares and circles) and fits to $\Delta_{SO} = \alpha_3 E_\perp k_{/\!/}^3$ (solid and dotted lines, respectively). To simulate interface roughness we used a Gaussian auto-correlation function model, with root-mean-square fluctuation $\Delta = 0.2$ nm and correlation length $\Lambda = 1.0$ nm. In this case, the fit reproduces well the TB calculation with $\alpha_3 E_\perp \approx 73$ eVÅ^3 and $\alpha_3 \approx 5 \times 10^5\, e\,$Å^4.

value is slightly smaller, yet close, to those reported in earlier studies on buried Ge QWs [95, 94, 96, 97].

In our strained-Ge QW system, where the 2DHG has a predominantly heavy-hole character, we expect the Rashba spin-orbit coupling to be dominated by a cubic term in the in-plane momentum, $k_{/\!/}$, as also reported in earlier studies [94, 75, 95]. Fig. 4.4.b shows a self-consistent TB calculation of $\Delta_{SO}(k_{/\!/})$ in a 32-nm thick Ge film saturated by hydrogen atoms [89]. We note that the linear $\propto k_{/\!/}$ dependence at small $k_{/\!/}$ is quickly overcome by a $\propto k_{/\!/}^3$ dependence. Interestingly, our calculation shows that for a rough, lower symmetry film, the linear component is almost suppressed (it oscillates rapidly with film thickness and is averaged down to ~ 0 by surface roughness). The calculated values of Δ_{SO} appear to be an order of magnitude lower than the experimental values reported in Fig. 4.3.c. This discrepancy may be ascribed to the simplified description of the surface in the TB calculation, the magnitude of Δ_{SO} being very sensitive to boundary conditions.

These TB calculations were done by Zaiping ZENG who belonged to

University Grenoble Alpes and INAC-MEM, CEA.

4.5 WAL under in-plane magnetic field

4.5.1 Fitting of in-plane-field WAL

To further investigate the nature of the zero-field conductivity enhancement, magneto-transport measurements were performed also with the magnetic field applied in the plane of the 2DHG, as indicated in Fig. 4.5. To first order, an in-plane magnetic field is not expected to break the WAL effect because it produces no flux through the time-reversed back-scattering trajectories. Contrary to this expectation, the longitudinal conductivity measured as a function of the in-plane magnetic field, $B_{/\!/}$, does exhibit a clear zero-field peak with a characteristic half width at half maximum of ~ 0.7 T, i.e. several times larger than in the case of perpendicular field.

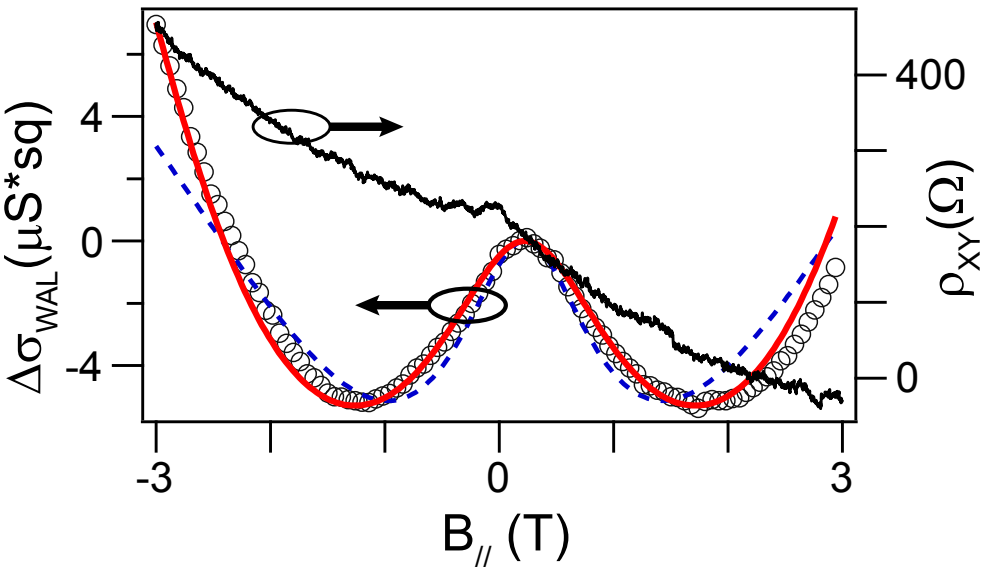

Figure 4.5: Black trace: Hall resistivity ρ_{XY} as a function of in plane magnetic field at V_{tg} = -5.8 V. The small dependence on field results from a small perpendicular field component. We estimate an angle of only 2° between $B_{/\!/}$ and the chip plane. Black circles: measured quantum correction to channel conductivity $\Delta\sigma_{WAL}$ revealing a weak anti-localization peak. The blue dashed line and the red solid line are fits to the model from Minkov *et al.* [98] without and with the addition of a $B_{/\!/}^6$ term respectively.

We can rule out the possibility of a misalignment of the magnetic field with respect to the plane of the 2DHG. In fact, from a simultaneous measurement of the Hall resistivity, also shown in Fig. 4.5, we estimate a misalignment of 2°. Therefore, the out-of-plane component of the applied field is far too small to explain the observed WAL peak.

Instead, following Minkov *et al.* [98], the effect can be ascribed to an effective finite thickness of the 2DHG, and the WAL peak in magnetoconductivity can be expressed as:

$$\Delta\sigma_{WAL}(B_{/\!/}) = \frac{e^2}{4\pi^2\hbar}\left[2\ln\left(\frac{B_\varphi + B_{SO} + \Delta_r}{B_\varphi + B_{SO}}\right) + \ln\left(\frac{B_\varphi + 2B_{SO} + \Delta_r}{B_\varphi + 2B_{SO}}\right) - \ln\left(\frac{B_\varphi + \Delta_r + \Delta_s}{B_\varphi}\right) + S\left(\frac{B_\varphi + \Delta_r}{B_{SO}}\right) - S\left(\frac{B_\varphi}{B_{SO}}\right)\right] \quad (4.2)$$

where Δ_r and Δ_s are $B_{/\!/}$-dependent corrections to B_φ taking into account the effect of surface roughness and Zeeman splitting, respectively. Following Ref. [98], we assume $\Delta_r = rB_{/\!/}^2$ and $\Delta_s = sB_{/\!/}^2$. The $S(x)$ function in Eq. (4.2) can be explicitly written as:

$$S(x) = \frac{8}{\sqrt{7+16x}}\left[\arctan\left(\frac{\sqrt{7+16x}}{1-2x}\right) - \pi\Theta(1-2x)\right] \quad (4.3)$$

where Θ is the Heaviside step function. For the effective fields B_{SO} and B_φ we take the values extracted from the previously discussed magnetotransport measurements in perpendicular magnetic field, for the same carrier density, i.e. $B_{SO} = 170$ mT and $B_\varphi = 19$ mT.

The dotted blue line in Fig. 4.5 is a fit to Eq. (4.2) using the proportionality factors r and s as fitting parameters. The fit shows only moderate agreement with the data. An improved fit can be obtained by introducing in the expression of Δ_r a second orbital term proportional to $B_{/\!/}^6$, i.e. $\Delta_r = r \times B_{/\!/}^2 + q \times B_{/\!/}^6$, with the additional fitting parameter q. This second term describes $B_{/\!/}$-induced time-reversal symmetry breaking via the virtual occupation of higher energy subbands [99–101]. The new fit, shown by a solid red line in Fig. 4.5, is in remarkably good agreement with the experimental data set over the entire $B_{/\!/}$ range. Following Ref. [100], the value of the fit parameter q can be related to the effective thickness d of the 2DHG, i.e. $d \sim (q\Phi_0^5/4\pi^2 n_{hole}^2)^{1/14}$. We find a realistic $d \sim 14$ nm, which can be regarded as a sanity check for the model used.

In principle, other pieces of information and physical quantities could be deduced from the fitting. However, the adopted analytic model is not sufficiently sophisticated to allow for quantitatively accurate conclusions. According to Minkov *et al.* [98], the fit parameter r is proportional to the product of $L_r h_r^2$, where h_r and L_r are the root-mean-square amplitude and the in-plane correlation length of the interface roughness, respectively. It may be tempting to extract some information about the surface roughness from the value of r resulting from the fit ($r = 5 \times 10^{-3}$ T^{-1}), yielding $L_r h_r^2 = 1.3 \times 10^{-25}\ m^3$. Assuming $h_r \sim 0.5$ nm (which is a reasonable guess), $L_r \sim 500$ nm. This value seems much larger than typical correlation lengths for an oxide/semiconductor interface roughness. The origin of this doubtful outcome is not so surprising if we consider that intersubband scattering is most likely dominated by charged interface defects rather than surface roughness as in the experiment of Minkov *et al.* [98]. In conclusion, while the model used to fit our in-plane magneto-conductivity data can capture the underlying physical picture, its use should not be stretched to obtain unreliable quantitative information.

4.6 Conclusion

Magneto-transport measurements of a 2DHG confined to a compressively strained Ge QW on the surface of a relaxed $Si_{0.2}Ge_{0.8}$ virtual substrate were discussed in this chapter. The 2DHG is formed by gate-induced hole accumulation up to carrier densities of the order of 10^{11} cm^{-2}. The hole mobility is highly reduced as compared to similar heterostructures where the QW is buried well below the surface. This can be explained by a high density of charge traps at the Ge/Al_2O_3 interface, as expected from the known poor quality of Ge native oxide. There exist possible solutions to increase interface quality [102], which could be explored in forthcoming studies.

A WAL peak is observed in the longitudinal magneto-conductivity at different V_{tg} and the characteristic times τ_{so} and τ_{φ} are estimated from the peak fitting assuming cubic Rashba SOI. The dependence of the τ_{tr} and τ_{so} on the carrier density implies a Dyakonov-Perel spin relaxation mechanism, owing to which the spin-splitting energy at zero field Δ_{SO} is calculated to be $\sim$1 meV. These characteristic times and the spin-splitting energy are consistent with values measured in buried Ge QWs [94, 95, 75]. Finally, it is found that WAL can as well be suppressed by an in-plane magnetic field, reflecting the finite thickness of the 2DHG and a contribution from Zeeman effect, surface roughness, and virtual inter-subband scattering processes.

This work was published in *Applied Physics Letters* [54].

Chapter 5

One-dimensional wire in buried Ge/SiGe heterostructure

5.1 Introduction

In this chapter, we report experimental evidence of ballistic hole transport in one-dimensional quantum wires (1d wires) gate-defined in a strained SiGe/Ge/SiGe quantum well. At zero magnetic field, we observe conductance plateaus at integer multiples of $2e^2/h$. At finite magnetic field, the splitting of these plateaus by Zeeman effect reveals largely anisotropic g-factors, with absolute values below 1 in the quantum-well plane, and exceeding 10 out of plane. This g-factor anisotropy is consistent with a heavy-hole character of the propagating valence-band states, in line with a predominant confinement in the growth direction. Remarkably, we observe quantized ballistic conductance in device channels up to 600 nm long. These findings mark an important step towards the realization of novel devices for applications in quantum spintronics.

5.2 Device fabrication

The devices were fabricated from a nominally undoped heterostructure consisting of a pseudomorphically strained, 22-nm thick Ge QW confined by $Si_{0.2}Ge_{0.8}$ barriers, i.e. a relaxed $Si_{0.2}Ge_{0.8}$ buffer layer below, and a 72-nm-thick $Si_{0.2}Ge_{0.8}$ layer above, capped by 2 nm of low-temperature-grown Si. The heterostructure was grown by reduced pressure chemical vapor deposition on a Si(001) wafer (See Ref. [103] and details therein). With an expected Ge/SiGe valence-band offset of 150 meV, a quantum well thickness of 22 nm results in a prominent size quantization leading to the formation

of two-dimensional subbands with well-separated energies (energy spacing of 10 - 20 meV). At the same time, a thickness of 22 nm is large enough to ensure a strong confinement of the heavy-hole ground-state subband, which remains close to the valence band edge.

At low temperature, the Ge QW is carrier free, and hence insulating, due to the intentional absence of doping. A two-dimensional hole gas with a mobility of $1.7 \times 10^5\,\mathrm{cm}^2/\mathrm{V\,s}$ and a hole density of $\sim 10^{11}\,\mathrm{cm}^{-2}$ can be electrostatically induced by means of a negatively biased top gate electrode.

The device layout consists of a large (tens of microns wide) mesa structure defined by **photolithography** and **reactive ion etching** with Cl_2 gas. The dry etching process is calibrated to remove both the SiGe overlayer and the Ge quantum well. This is done to prevent gate leakage caused by threading dislocations produced during the wedge bonding of the gate pads (which are positioned around the mesa structure). Two platinum contact pads, to be used as source and drain electrodes, are fabricated on opposite sides of the mesa. Platinum deposition is carried out after dry-etch removal of the SiGe overlayer followed by a two-step surface cleaning process to eliminate the native oxide (wet HF etching followed by Ar plasma bombardment in the e-beam evaporator). We obtain contact resistances of the order of few kΩ. An Al_2O_3 30-nm thick gate oxide layer is deposited by **ALD** at 250 C°. Ti/Au top-gate electrodes are finally defined using **electron beam lithography** and **electron beam evaporation**: a central gate extending over the mesa is designed to induce the accumulation of a conducting hole channel between the source to the drain contact; two side gates, to be operated in depletion mode, create a tunable 1D constriction in the channel oriented along the [100] direction. We have varied the geometry of the side gates in order to explore gate-defined 1D hole wires with different lengths. Here we present experimental data for two devices, one with a short ($\sim$ 100 nm) and one with a long ($\sim$ 600 nm) constriction (see Figs. 5.2 (a) and (b), respectively).

5.3 Heterostructure characterization

The details of the heterostructure used in this chapter are given in Fig. 5.1 (a) [104, 105]. To characterize the basic electronic properties of this heterostructure, gated Hall-bar devices (Fig. 5.1 (b)) were fabricated and measured at 0.3 K. Representative measurements of longitudinal resistivity, ρ_{xx}, and Hall resistivity, ρ_{xy}, are shown in Fig. 5.1 (c). Shubnikov-de Haas (SdH) oscillations and quantum Hall plateaus are observed in ρ_{xx} and ρ_{xy}, , respectively. The two-dimensional hole density, n_s, and the hole mobility,

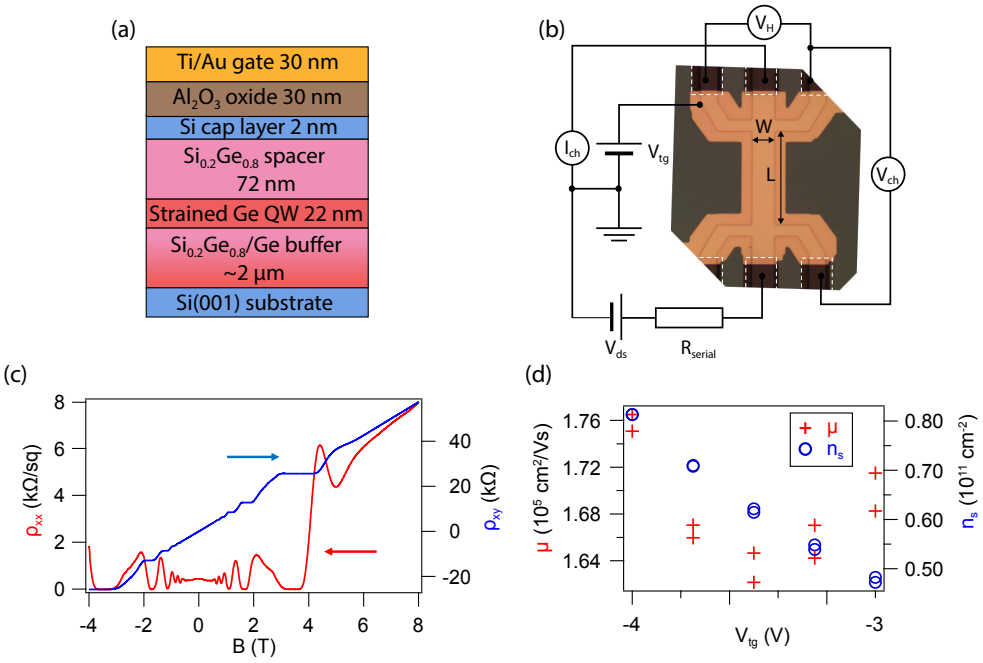

Figure 5.1: (a) Schematic diagram of $Ge/Si_{0.2}Ge_{0.8}$ heterostructure with top gate. (b) Optical image of a gated Hall bar structure. White broken lines indicate six ohmic contacts. A top gate (yellow) overlaps each ohmic contacts and mesa structure. The mesa structure with a channel (L = 80 µm and W = 20 µm) is seen through the top gate. The channel direction is $[\bar{1}10]$. A serial resistance R_{serial} = 1 MΩ is connected to the channel. Constant bias voltage is applied and when the channel resistance is much lower than the R_{serial} a constant current flows. The current through the channel I_{ds}, longitudinal voltage V_{ch} and Hall voltage V_H are measured at 300 mK as a function of gate voltage V_{tg} or out-of-plane magnetic field B and converted to longitudinal sheet resistivity $\rho_{xx} = V_{ch}/I_{ds} * W/L$ and Hall resistivity $\rho_{xy} = V_H/I_{ds}$. (c) Typical results of ρ_{xx} and ρ_{xy} vs B for V_{ds} = 100 mV and V_{tg} = -4 V. Clear longitudinal resistivity oscillation (Shubnikov–de Haas effect) and Hall resistivity plateaus (quantum Hall effect) are observed (red and blue lines, respectively). At B = 3 T, the filling factor $\nu = 1$. Around B = 5 T, $\nu = 2/3$. (d) Hall density n_s and hole mobility μ vs V_{tg}. n_s is estimated from (classical) Hall effect in small magnetic fields and mobility μ is calculated for the relation $\mu = (en_s\rho_{xx})^{-1}$ at $B = 0$, where e is the electron charge.

μ, are plotted as a function of V_{tg} in Fig. 5.1 (d). In the shown V_{tg} range, n_s depends linearly on V_{tg}, reaching the largest value of 0.8×10^{11} cm^{-2} at the most negative V_{tg}. This is close to maximal hole density that could be achieved. In fact, by going to more negative V_{tg}, i.e. $V_{tg} < -4$ V, we encountered two types of problems: the accumulation of a parasite hole gas at the interface with the gate oxide [106, 107], and gate leakage.

5.4 Linear transport and non-linear transport

All magnetotransport measurements were done at 270 mK in a ^{3}He cryostat equipped with a superconducting magnet. Figure 5.2 (c) shows a data set for a device, labelled D1, nominally identical to the one shown in Fig. 5.2 (a). The differential conductance, G, measured at dc source-drain bias voltage $V_{ds} = 0$, is plotted as a function of V_{sg} for magnetic fields, $\vec{B}$, perpendicular to the QW plane and varying from 0 to 0.5 T. In our experiment, G was directly measured using standard lock-in detection with a bias-voltage modulation $\delta V_{sd} = 10\,\mu$V at 36.666 Hz. In addition, G was numerically corrected to remove the contribution from all series resistances (~ 20 kΩ), i.e. the resistances of the measurement circuit, the source and drain contacts, and the two-dimensional hole gas.

G exhibits clear quantized plateaus in steps of $2e^2/h$, where e is the electron charge and h is the Plank constant. This finding is consistent with the results of a recently published independent work carried out on a similar SiGe heterostructure [56]. Applying an out-of-plane magnetic field lifts the spin degeneracy of the 1D subbands, resulting in plateaus at multiples of e^2/h. These plateaus underpin the formation of spin-polarized subbands. They emerge at relatively small magnetic fields, of the order of a few hundred mT, denoting a large out-of-plane g-factor as expected in the case of a predominant HH character.

We measured several devices with side-gate lengths, L_g, ranging from 100 nm (as in Fig. 5.2 (a)) to 900 nm. The $G(V_{sg})$ measurements shown in Fig. 5.2(d) were taken on a device with $L_g \approx 600$ nm, labelled as D2 and nominally identical to the one shown in Fig. 5.2(b). Remarkably, these measurements demonstrate that clear conductance quantization can be observed also in relatively long channels largely exceeding 100 nm. Increasing the channel length should result in an appreciable sharpening of the conductance steps, reflecting a reduced probability of tunneling across the electrostatically induced potential barrier [108]. In our experiment,

however, this effect is barely visible because the conductance step width is dominated by the thermal broadening of the Fermi distribution function in the leads.

We note that a shoulder at $G \sim 0.7 \times 2e^2/h$ is visible in the $B = 0$ traces of both Fig. 5.2 (c) and (d). This feature, which is highlighted in the respective insets, corresponds to the so-called 0.7 anomaly. Discovered and widely studied in quantum point contacts defined in high-mobility two-dimensional electron systems [109–114], and more recently observed also in semiconductor nanowires [115, 116], the interpretation of this phenomenon remains somewhat debated [117–121].

To further confirm the 1D nature of the observed conductance quantization, we present in Figs. 5.3 (a)-(c) waterfall plots of the non-linear $G(V_{ds})$ at three different perpendicular magnetic fields ($B = 0$, 0.3, and 0.5 T, respectively) for device D1. Clear bunching of the $G(V_{ds})$ is observed around $V_{ds} = 0$ for gate voltages corresponding to the quantized conductance plateaus of Fig. 5.2(c). With magnetic field applied, the first plateau at $G = e^2/h$ begins to appear at $B = 0.3$ T and is fully formed at $B = 0.5$ T. At $B = 0$, a zero-bias dI/dV peak can seen in correspondence of the 0.7 structure, in line with previous observations [112].

5.5 Magnetic field dependence

The well-resolved spin splitting of the 1D subbands enables a quantitative study of the hole g-factors. To investigate the g-factor anisotropy, we applied $\vec{B}$ not only along the z axis, perpendicular to the substrate plane, but also along the in-plane directions x and y, indicated in Figure 5.2 (a). To change the $\vec{B}$ direction, the sample had to be warmed up, rotated, and cooled down multiple times. Thermal cycling did not modify significantly the device behavior, except for the value of threshold voltage on the channel gate for the activation of hole conduction in the Ge QW (this voltage is sensitive to variations in the static charges on the sample surface).

Figures 5.4 (a), (b) and (c) show the B-evolution of the trans-conductance dG/dV_{sg} as a function of V_{sg}, with $\vec{B}$ applied along x, y and z, respectively. The data refer to device D1. In these color maps, the blue regions, where dG/dV_{sg} is largely suppressed, correspond to the plateaus of quantized conductance. On the other hand, the red ridges of enhanced dG/dV_{sg} correspond to the conductance steps between consecutive plateaus, which occur every time the edge of a 1D subband crosses the Fermi energy of the leads. At finite B, the red ridges split, following the emergence of new conductance plateaus at odd-integer multiples of e^2/h. Upon increasing B, the splitting

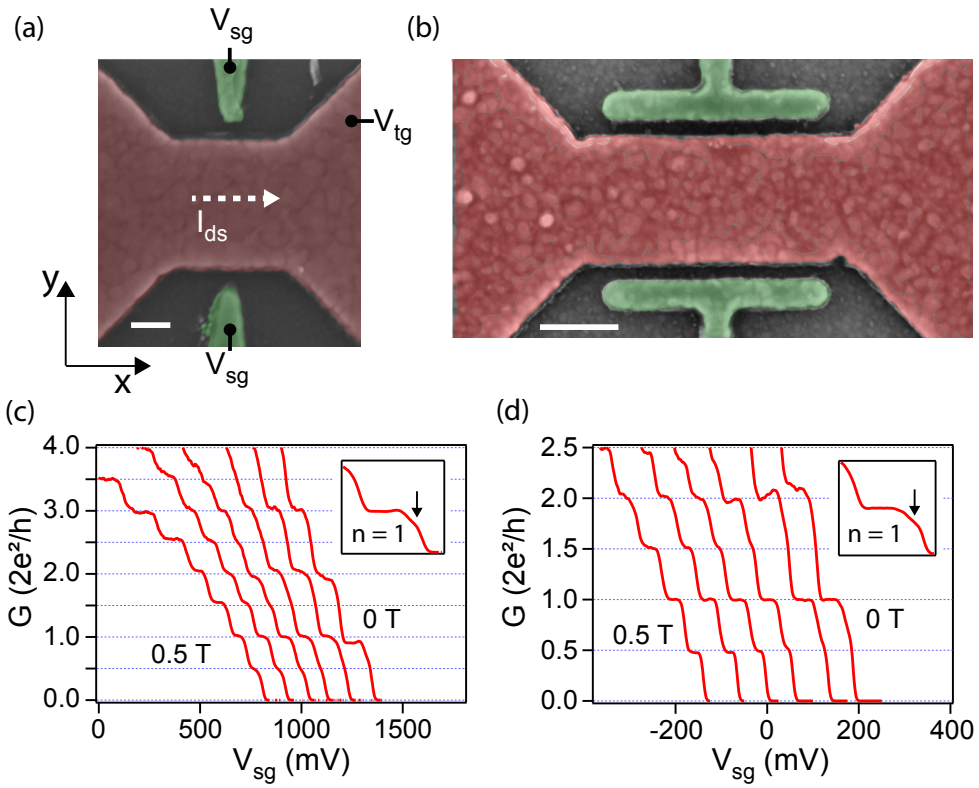

Figure 5.2: (a) and (b) False color scanning electron micro-graphs of representative devices. Scale bars: 100 nm (a) and 200 nm (b). Gate voltages $V_{tg} < 0$ and $V_{sg} > 0$ are applied to the channel gate (colorized in red) and the two side gates (colorized in green), respectively. Current I_{ds} flows in Ge QW under the channel gate along the x direction. To enable that, the channel gate extends all the way to the source/drain contact pads, which are located about 15 μm away from nanowire constriction, i.e. outside of the view field in (a) and (b). (c) and (d) Measurements of zero-bias conductance G as a function of V_{sg} at different perpendicular magnetic fields, B_z, from 0 to 0.5 T (step: 0.1 T). Data in (c) ((d)) refer to device D1 (D2), which is nominally identical to the one shown in (a) ((b)). In both cases we observe clear conductance quantization and the lifting of spin degeneracy at finite field. Conductance has been rescaled to remove the contribution of a series resistance R_S slightly varying with B_z between 22 and 24 kΩ. The different traces are laterally offset for clarity. Insets: Zoom-in of the 0.7 anomaly (indicated by an arrow) at zero magnetic field.

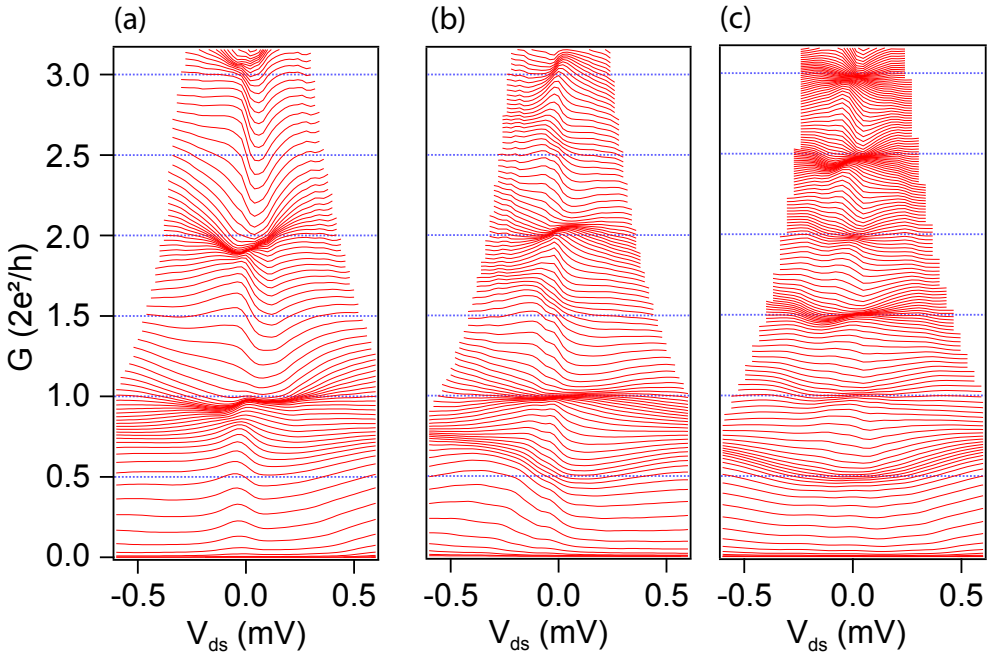

Figure 5.3: Waterfall plots of differential conductance, G, as a function of source-drain bias, V_{ds}, at different values of side-gate voltage V_{sg} (gate step: 5 mV). The three plots were taken on device D1 at different out-of-plane magnetic fields: (a) 0 T, (b) 0.3 T and (c) 0.5 T. The spanned V_{ds} range varies with V_{sg}, and hence with G. This follows from the procedure used to take into account the effect of the series resistance, R_S. In this procedure, we assumed R_S to be monotonically increasing with the current I_{sd} flowing across the device. This assumption was motivated by the need to account for non-linearities in the series resistance coming primarily from the source/drain contacts to the two-dimensional hole gas. At $V_{sd} = 0$, R_S is a constant all over the spanned V_{sg} range. At finite V_{sd}, R_S varies with V_{sg} due to the V_{sg} dependence of G. As a result, the corrected V_{ds} range tends to decrease when lowering V_{sg}, and hence increasing G.

in V_{sg} increases proportionally to the Zeeman energy $E_{Z,n} = |E_{n,\uparrow} - E_{n,\downarrow}|$, where $E_{n,\sigma}$ is the energy of the 1D subband with spin polarization σ and orbital index n.

For an in-plane B, either along x or y, the splitting becomes clearly visible only above approximately 2 T. As a result, the explored B range extends up to 6 T. For a perpendicular field, the Zeeman splitting is clearly more pronounced being visible already around 0.2 T. This apparent dis-

crepancy reveals a pronounced g-factor anisotropy, with a g-factor along the z-axis, g_z, much larger than the in-plane g-factors, g_x and g_y. Such a strong anisotropy is expected in the case of two-dimensional hole states with dominant HH character, corroborating the hypothesis of a dominant confinement in the z direction, which is imposed by the QW heterostructure.

Besides causing the Zeeman splitting of the 1D subbands, the applied $\vec{B}$ has an effect on the orbital degree freedom of the hole states. The effect is relatively weak in the case of an in-plane B because the magnetic length, inversely proportional to $\sqrt{B}$, gets as small as the QW thickness only for the highest B values spanned in Figs. 5.4(a) and 5.4(b). On the contrary, the relatively weak lateral confinement imposed by the side gates leaves room for a pronounced B-induced orbital shift. This manifests in Fig. 5.4 (c) as an apparent bending of the dG/dV_{sg} ridges towards more negative gate voltages.

5.5.1 Estimation of Zeeman splitting

In this section we illustrate the procedure to measure Zeeman energy splittings. The color plot in Fig. 5.5 is a representative example of a dG/dV_{sg} as a function of V_{ds} and V_{sg} at $B_z = 0.4$ T. The magnetic field is large enough to lift spin degeneracy. The diamond-shape blue regions centered around $V_{ds} = 0$ V correspond to conductance plateaus at integer multiples of e^2/h. White/red lines bordering the diamonds define the edges of the plateaus. These lines are not always clearly visible. Dashed lines have been drawn to highlight their position. These lines correspond to aligning the energy of a subband edge with the Fermi energy of either the source or the drain lead. As a result, the apexes of the diamonds, defined by the crossings of consecutive dashed lines, are located at a source-drain bias voltage equal to the energy spacing between consecutive subband edges. The horizontal half-widths of the odd diamonds provide a direct quantitative measurement of the Zeeman energies $E_{Z,n}$, as illustrated in Fig. 5.5. The measurement accuracy can be conservatively estimated by varying the slope of the dashed lines until it becomes apparent that they no longer follow the dG/dV_{sg} ridges. Because the dG/dV_{sg} ridges happen to be generally broad and sometimes even hard to identify, we end up with rather large measurement uncertainties.

Besides providing access to the Zeeman splitting energies, the stability diagram of Fig. 5.5 can be used to extract the gate lever-arm parameter, α, which is the proportionality factor relating a gate voltage variation to the corresponding shift in the electrochemical potential in the 1D wire. In

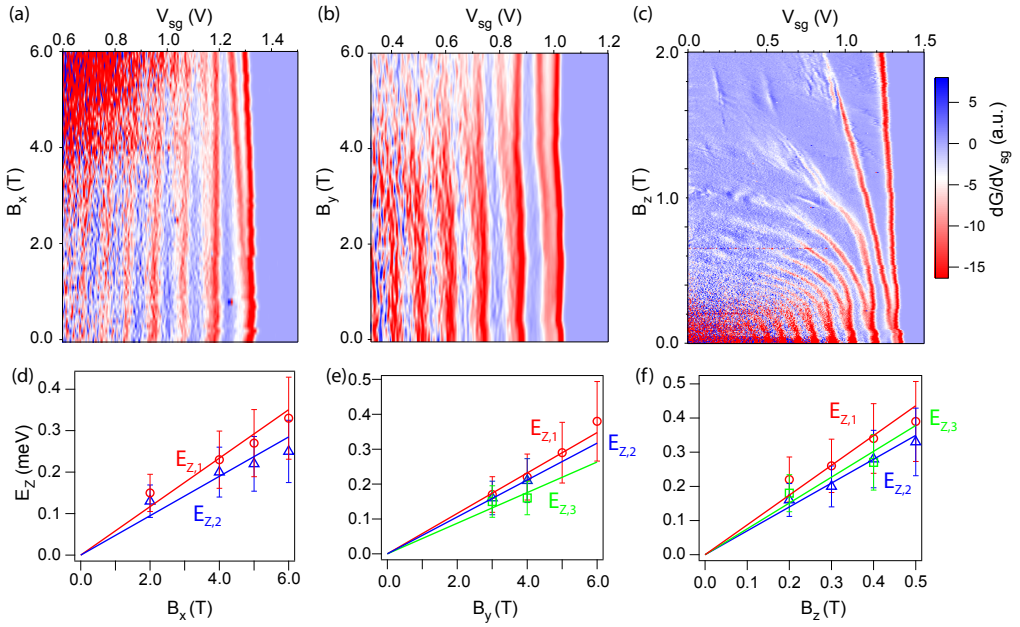

Figure 5.4: (a)-(c) Numerical derivative of G with respect to V_{sg} as a function of V_{sg} and magnetic field applied along the x (a), y (b) and z (c) directions (data from device D1). (d)-(f) Zeeman splittings $E_{Z,n} = |E_{n,\uparrow} - E_{n,\downarrow}|$ as a function of magnetic field along the x (d), y (e) and z (f) directions. Red, blue, and green open symbols correspond to the first, second, and third spin-split subbands, respectively. The g factors for each subband are obtained from the slope of the linear fits to the Zeeman relation $E_{Z,n}(B)$ (solid lines). The results are given in Table 5.1.

practice, for the n-th orbital subband α is obtained from the ratio between $E_{Z,n}$ and the height (measured along the V_{sg} axis) of the 2n−1 diamond. We find that α decreases noticeably with n and, to a lower extent, it varies with $\vec{B}$. For the case of Fig. 5.5 we find $\alpha \approx 5 \times 10^{-3} eV/V$ for n = 1, $\alpha \approx 3.3 \times 10^{-3} eV/V$ for n=2, and $\alpha \approx 2.3 \times 10^{-3} eV/V$ for n = 3.

In the limit of vanishing $\vec{B}$, the odd diamonds shrink and disappear while the even diamonds grow. At $B = 0$, the 2n diamond has a horizontal half-width set by the energy spacing $\Delta_{n,n+1}$ between the n-th and the (n+1)-th orbital subband. We measure $\Delta_{1,2} \approx 0.65$ meV and $\Delta_{2,3} \approx 0.5$ meV.

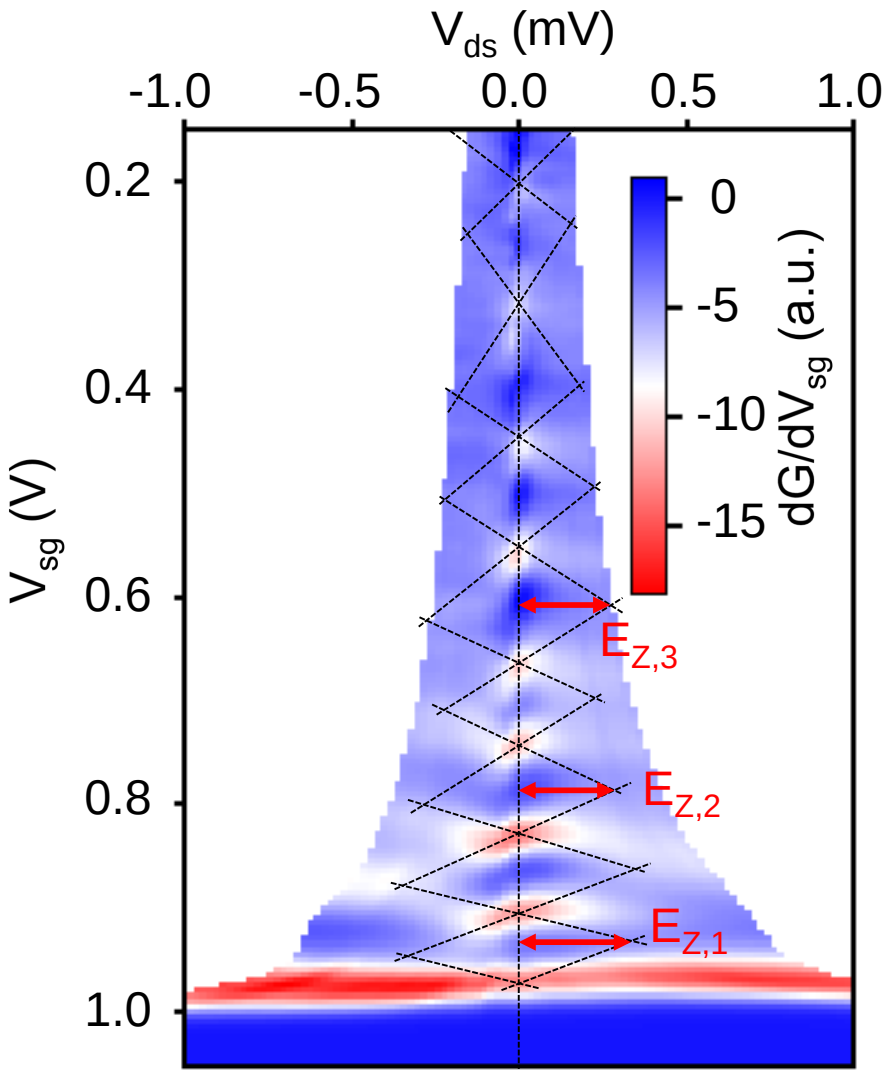

Figure 5.5: Color plot of dG/dV_{sg} of as a function of V_{sg} and V_{ds} at $B_z = 0.4$ T. Energy separations between two spin-resolved subbands are estimated from a half the distance of two points where two conductance edges cross (red solid arrow).

5.5.2 Anisotropic g factor of Ge 1D-wire

In order to quantitatively estimate the observed Zeeman splittings, and the corresponding g-factors, we performed bias-spectroscopy measurements of dG/dV_{sg} as a function of V_{ds} and V_{sg} at different magnetic fields.

Figures 5.4 (d), (e), and (f) present the estimated $E_{\mathrm{Z},n}$ values as a function of B, for the first few subbands, and for the three B directions. Linear fitting to $E_{\mathrm{Z},n} = g_n \mu_{\mathrm{B}} B$ yields the Landé g-factors, $g_{x,n}$, $g_{y,n}$, and $g_{z,n}$ for the three perpendicular directions. The extracted g-factors for the device D1 are listed in Table 5.1. We have included also the $g_{z,n}$ values obtained from another device (D3) with $L_g = 100$ nm.

For device D1 (D3), the perpendicular g-factor ranges between 12.0 (10.4) and 15.0 (12.7), while the in-plane one is much smaller, varying between 0.76 and 1.00, with no significant difference between x and y directions. A large in-plane/out-of-plane anisotropy in the g-factors is consistent with the hypothesis of a dominant HH character. In fact, in the limit of vanishing thickness, the lowest subbands of a Ge QW should approach pure HHs with $g_x \approx g_y \approx 0$ and $g_z = 6\kappa + 27q/2 = 21.27$, where κ and q are the Luttinger parameters ($\kappa = 3.41$ and $q = 0.06$ for Ge).

In the investigated SiGe QW heterostructure, the HH nature of the first 2D subbands is enhanced by the presence of a biaxial compressive strain in the Ge QW, increasing by ~ 40 meV the energy splitting with the first light-hole (LH) subbands [95]. The creation of a 1D constriction does not introduce a significant HH-LH mixing because confinement remains dominated by the QW along the growth axis (z). From a measured energy spacing of around 0.65 meV between the first and the second 1D subband, we estimate that the hole wavefunctions of the first subband have a lateral width (along y) of approximately 80 nm, which is an order of magnitude larger than the wavefunction extension along z.

The results summarized in Table 5.1 suggest a slight tendency of the g-factors to decrease with the subband index. This trend is consistent with the results of earlier experiments with both electron [122, 115] and hole [123–125] quantum point contacts. A possible explanation is that the exchange interaction increases the g-factor in the low-density limit [110, 126]. Yet hole g-factors in quantum point contacts depend also on a complex interplay of spin-orbit coupling, applied magnetic field, and electrostatic potential landscape [127, 68]. Acquiring a deep understanding of the g-factors reported here would require more extensive and sophisticated experiments together with a nontrivial theoretical analysis, which goes well beyond the scope of the present work.

Table 5.1: This table summarizes the results of g-factor measurements on device D1 and D3. These g-factors are obtained from the slope of the linear fits in Fig. 5.4 (d)-(f)) and Fig. 5.7 (c).

		g_1	g_2	g_3
D1	B_x	1.00 ± 0.15	0.82 ± 0.12	-
	B_y	1.00 ± 0.15	0.91 ± 0.19	0.76 ± 0.16
	B_z	15.0 ± 2.3	12.0 ± 1.8	13.0 ± 2.8
D3	B_z	12.7 ± 2.2	11.8 ± 1.8	10.4 ± 1.6

5.5.3 Carrier density in the 1D-wire device

The carrier density in the 2DHG can be approximately deduced from the resistance of the two-terminal 1D-wire device R. Under high out-of-plane magnetic fields B_z, the magnetic confinement becomes dominant over the electric confinement ($\omega_0 \ll \omega_c$) and the edge channels are formed even in 1D-wire. These edge channels are 1D by nature and the conductance is quantized in units of e^2/h for the edge channels as well as in electrically confined narrow channel. As in the case of the quantum-Hall resistance $R = h/(e^2\nu) = B/(en_s)$, hence the barycenters of the plateaus in R are expected to fall on a straight line going through the origin whose slope is $1/en_s$.

The magnetic-field dependence of a 1D-wire resistance R is shown in Fig. 5.6 after correction for the series resistance. The data is taken from a line cut of Fig. 5.4 (c) at $V_{sg} = 0$.

The resulting carrier density is $n_s = (0.93 \pm 0.1) \times 10^{11}\,\mathrm{cm}^{-2}$. This density is basically the same as the sheet density measured in a Hall-bar device.

5.6 Data from device D3

Figure 5.7 shows a set of data from a third device (D3) made from the same heterostructure. This device has the same gate layout as D1 as shown in Fig. 5.2 (a). It was measured with only one orientation of the applied magnetic field, perpendicular to the device plane (z-axis). The procedure to correct for the series resistances, and the data analysis was the same as for the previous devices. The results are qualitatively and quantitatively similar to those from device D1.

5.7 Conclusion

In conclusion, we have demonstrated ballistic hole transports in 1D quantum wires gate-defined in a $Ge/Si_{0.2}Ge_{0.8}$ heterostructure. Conductance quantization is observed in channels up to 600 nm long. By investigating the Zeeman splitting of the quantized conductance steps we find that out-of-plane g-factors are an order of magnitude larger than the in-plane ones, denoting a pronounced HH character. This can be ascribed to the dominant confinement along the growth axis and to the compressive biaxial strain in the Ge QW. The observation of ballistic 1D hole transport in remarkably long channels and large out-of-plane g-factors holds special promise for the development of devices with spin-related functionality. In principle, the fabrication of these devices could be implemented in

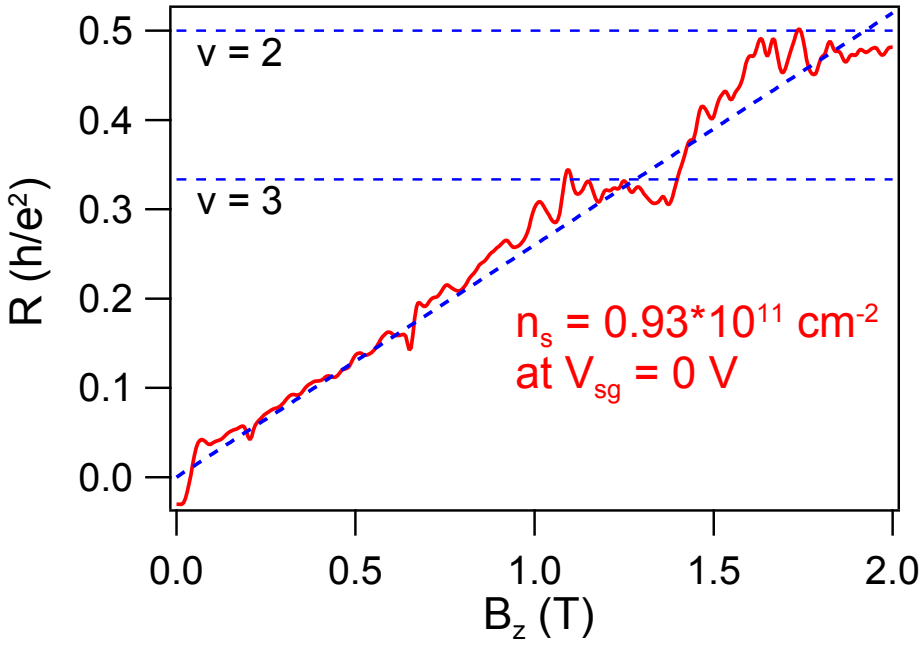

Figure 5.6: 1D-wire resistant R as a function of perpendicular magnetic field. The data set is taken from Fig. 5.4 for $V_{sg} = 0$ and it includes correction for the series resistances. (a four-point smoothing is also applied). The visible resistance plateaus and the Landau-level filling factors ν are indicated by horizontal dashed lines. From the slope of the line crossing the mid point of the resistance plateaus we deduce a 2D carrier density $n_s = (0.93 \pm 0.1) \times 10^{11}\,\mathrm{cm}^{-2}$.

an industry-standard fab line with the possibility of monolithic integration with conventional silicon electronics.

This work was submitted for publication. A preprint is available on arXiv (arXiv:1804.04674) [128].

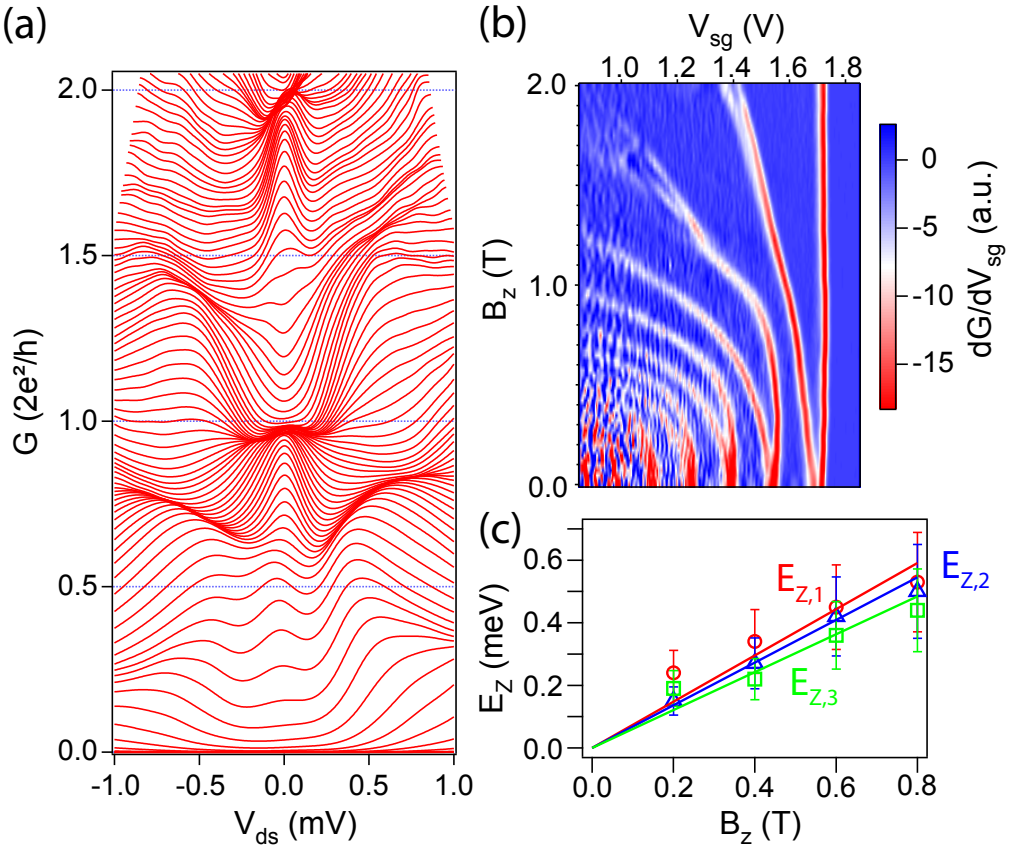

Figure 5.7: Experimental data for device D3. (a) Differential conductance G as a function of V_{ds} at different V_{sg} and $B_z = 0$, (b) Linear transconductance dG/dV_{sg} as a function of V_{sg} and B_z, and (c) E_z vs B_z. Large out-of-plane g factors are observed as in device D1 (see Table 5.1).

Chapter 6

Single quantum dot in buried Ge/SiGe heterostructure

6.1 Introduction

Spins in quantum dots are good candidates for the realization of quantum computers. Recently, it has been observed that the coherence of an electron spin bound to a phosphorus atom in isotopically-purified silicon lasts for a remarkably long time ($T_2^* = 2.4$ ms [129]). Shorter, yet still conveniently long, coherence times were reported for electron spins in quantum dots based on isotopically-purified Si [25]. A recent work by the Tarucha group obtained $T_2^* = 20$ μs [21] in a Si/SiGe heterostructure grown using a ^{28}Si source. In this case, the long spin coherence, enhanced by isotopic purification, was combined with fast electrically-driven spin control, thanks to the artificial SOI arising from a local micromagnet. This results in a large quality factor $Q = T_2^*/\tau_{op} \approx 10^3$ (τ_{op} is the π-rotation time), which exceeds the threshold for quantum error correction. A heavy-hole spin in a Ge QD is also supposed to be a good candidate for qubit implementation. Heavy holes combine long spin coherence time (enhanced by the p-like orbitals of HHs) and strong SOI enabling fast spin manipulation with electric fields.

In the literature, a HH spin manipulation in a III-V-group self-assembled QD has been reported [130, 65, 64, 131]. In particular, utilizing in-plane fields to suppress the HH-LH mixing which enhances the hyperfine coupling and reduces coherence time [64], it is demonstrated that a strained InGaAs QD has $T_2^* = 70$ ns, which is an order of magnitude longer than that of electrons in the same QDs [131].

In this chapter, we realized QD structures in the same buried Ge QW heterostructure as the one used for the 1D wire of the previous chapter.

Two types of gate structures were implemented to form single QD devices. The first one is a single-layer gate (SLG) layout, in which all of the surface gates are simultaneously fabricated in a single metal deposition step. This approach is the same as the one used for the realization of the 1D-wire devices discussed in the previous chapter. In the second approach, the QD devices are realized with a double-layer gate (DLG) layout consisting of two layers of overlapping gates If the first approach is less demanding in terms of fabrication, the second one should offer better tunability.

6.2 Single-layer single quantum dot

First, we realized and tested SLG devices by modifying the 1D-wire design of the previous chapter as shown in Fig. 6.1 (a) and Fig. 6.2 (a). The fabrication procedure is basically the same as the described in Ch. 5. The SLG devices have a top gate (colorized in red) to accumulate holes in a wire oriented along x. Three side gates (colorized in green) are defined next to the top-gate. Voltages V_L and V_R applied to the side gates form and control two tunnel barriers leading to confinement of holes also along the x axis. The voltage V_C on the central plunger gate tunes the electrochemical potential of the QD. The transport properties two devices where measured at 0.3 K in a ^{3}He cryostat. The drain-source current, I_{ds}, was measured as a function of the gate voltages and DC bias voltage V_{ds}. The differential conductance was measured by standard lock-in technique using a voltage modulation of $10\,\mu V$ at 36.666 Hz. Contrary to the case of the 1D wires, the series resistance, of the order of $1 \sim 10$ kΩ, was typically negligible as compared to the QD resistance (> 1MΩ).

The first SLG device (SLG1) has a simple wire structure (Fig. 6.1 (a)). Note that the width $\sim$ 100 nm is narrower than the one of the 1D wires presented in Ch. 5 ($\sim$ 300 nm). As a consequence, larger top-gate voltages are required to accumulate holes. On the other hand, the narrower profile should result in a smaller QD with larger charging energy and larger level spacing. The differential conductance G at zero DC bias voltage (linear regime) shows peaks as a function of V_C at $V_{tg} = -2.1$ V, $V_R = 0.4$ V, and $V_L = 1.87$ V (Fig. 6.1 (b)). These peaks correspond to Coulomb-blockade oscillations. This Coulomb-blockade regime is confirmed by measurements of G as a function of V_g and V_{ds} (Fig. 6.1 (c)). As expected, the Coulomb-blockade regions have the characteristic diamond shape. In fact, only one Coulomb diamond with strongly suppressed G can be clearly identified. This can be explained by the fact that the plunger gate has a strong effect on the tunnel barriers. The corresponding tunnel couplings appear to in-

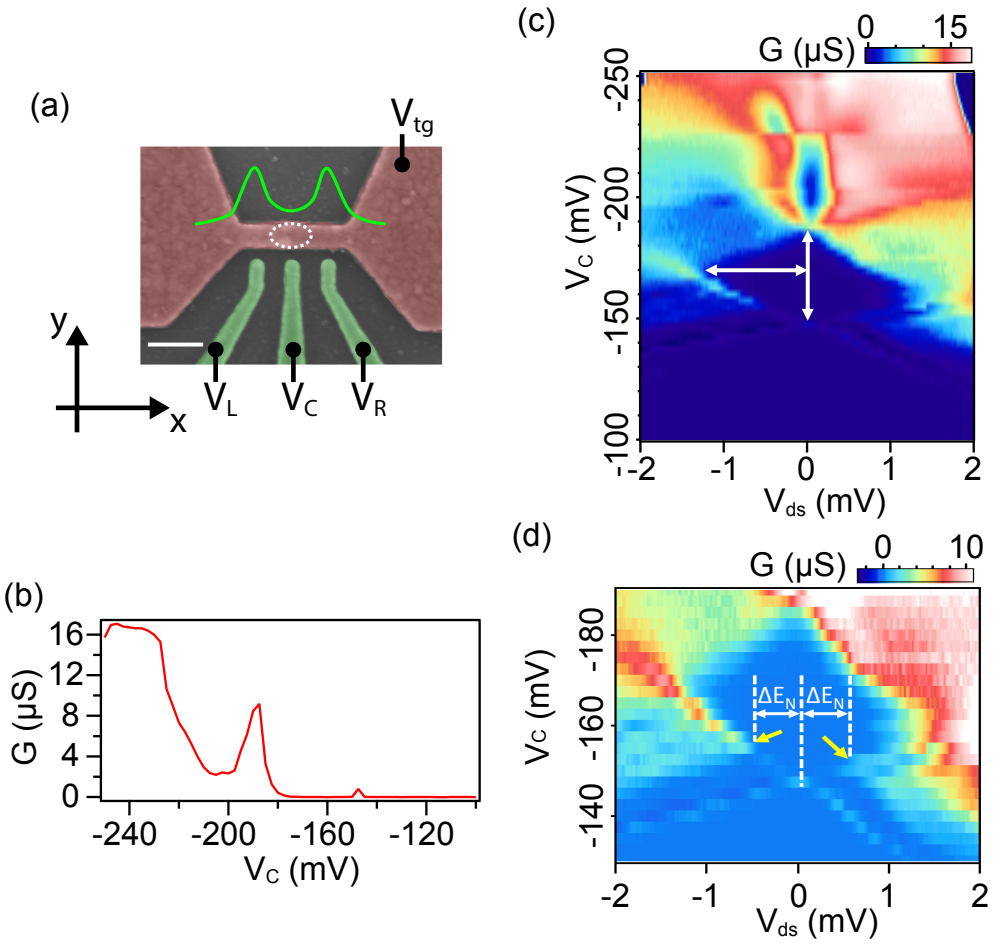

Figure 6.1: (a) False-color SEM image of device SLG1. Scale bar: 200 nm. Holes are accumulated below the top gate (red) following the application of a negative voltage $V_{tg} < 0$. Voltages V_L, V_C, and V_R are applied to the finger gates (green) in order to create and control the tunnel barriers and to tune the electrochemical potential in the QD. The green solid line depicts the expected qualitative energy diagram. The white dashed line highlights the expected location of the QD. (b) Zero-bias differential conductance G vs V_C. (c) G vs V_C and V_{ds} for $V_{tg} = -2.1$ V, $V_R = 0.4$ V, and $V_L = 1.87$ V. The horizontal arrow measures the addition energy. The vertical arrow measures e/C_G. (d) Zoom-in of the date plot in (c); the yellow arrows denote conductance ridges associated with the onset of tunneling via an excited state of the quantum dot with excitation energy $\Delta E_N \approx 0.6$ meV.

crease rapidly as V_C varies from -100 mV to -250 mV, becoming comparable to the charging energy and, therefore, washing out the Coulomb blockade effect. By analyzing the clearly visible Coulomb diamond, we can extract important information on the QD. The half width of the diamond, ΔV_{sd}, measured along the V_{ds} axis (white horizontal arrow in Fig. 6.1 (c)) gives the addition energy, i.e. $E_{add} = e\Delta V_{ds} = 1.35$ meV. This coincides with the charging E_c possibly augmented by the energy level spacing in the QD. The width ΔV_C of the Coulomb diamond along the V_C axis, i.e. the gate distance between the two Coulomb peaks of Fig. 6.1 (b), gives the plunger-gate capacitance $C_G = e/\Delta V_C$. Finally, we can estimate the gate lever-arm parameter $\alpha = E_{add}/\Delta V_C = 0.04$ eV/V, which converts the gate voltage into energy.

A zoom-in of Fig. 6.1 (c) is shown in Fig. 6.1 (d). The color scale has been adjusted to highlight the presence of additional lines parallel to the diamond edges. These lines, indicated by yellow arrows, correspond to the onset of tunneling through excited levels of the QD. Their position gives an energy level spacing $\Delta E_N \approx 0.6$ meV, as illustrated in Fig. 6.1 (d). With an expected in-plane hole effective mass of 0.07, the obtained level spacing would correspond to a QD size of roughly 100 nm.

The application of a magnetic field would induce the Zeeman splitting of the QD states, giving access to the hole g-factors, and possibly revealing SOI effects on the QD energy levels. However, this possibility could not be investigated due to the poor charge stability of the device. A clear charge switching event can be seen in Fig. 6.1 (c) at $V_C = -225$ mV. Repeated charge switching events prevented the possibility to perform more systematic studies.

In the second SLG device (SLG2) (Fig. 6.2 (a)), the top gate has a wider middle region which is intended to enhance confinement in the central portion of the wire and reduce the effect of the plunger gate on the tunnel barriers. This seems indeed confirmed by the observation of a larger number of Coulomb diamonds, as shown in Fig. 6.2 (b). From this measurement, we estimate $E_{add} \sim E_c \sim 1.0$ meV and $\alpha = 0.074$ eV/V. The fact that α is larger than in device SLG1 is due to the stronger capacitive coupling of the QD to the plunger gate electrode. Unfortunately, as in the case of SLG1, the charge stability of this second device turned out to be rather poor preventing any further study. Following these results, we decided to explore an alternative fabrication approach as discussed below.

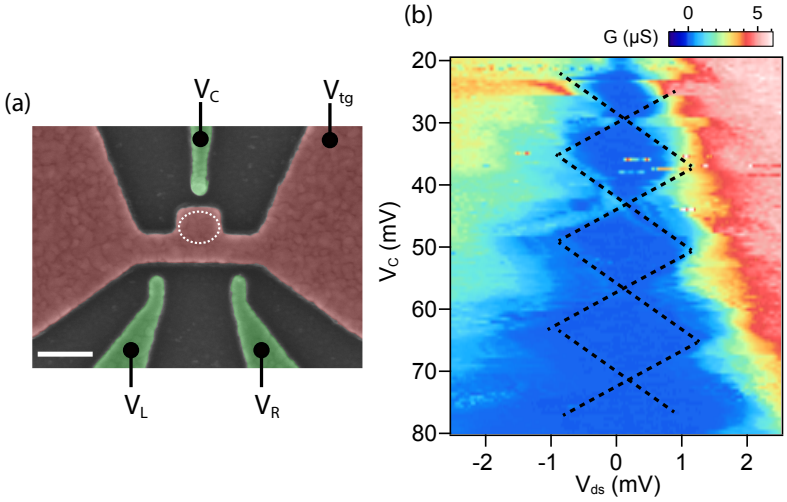

Figure 6.2: (a) False-color SEM image of device SLG2. Scale bar: 200 nm. The expected location of the QD is indicated by a white dashed line. (b) G vs V_{ds} and V_C at $V_{tg} = -680$ mV and $V_L = V_R = 1.86$ V. The Coulomb diamonds are highlighted by black dashed lines.

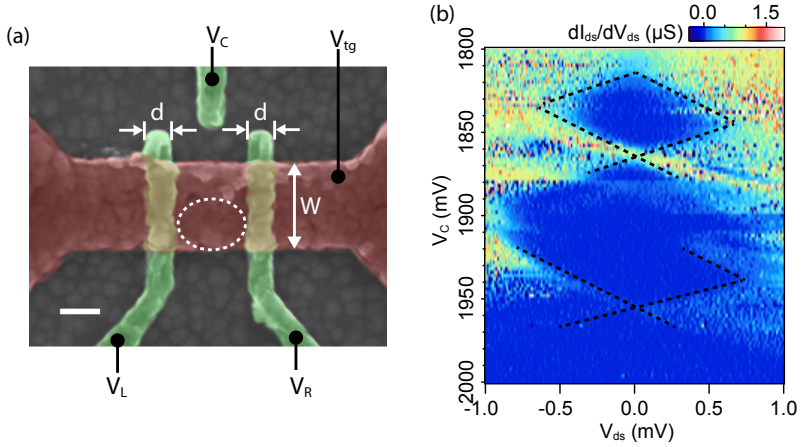

Figure 6.3: (a) False-color SEM image of a DLG device. Scale bar: 100 nm. The device has two barrier gates and a plunger gate (all colorized in green), as well as an accumulation top gate (red). The latter overlaps with the barrier gates. The oxide layer covering the barrier gates prevents inter-gate leakage. The QD position is schematically represented by a white dashed line. Several devices with different gate widths d and W were measured. (b) G vs V_{ds} and V_C at $V_{tg} = -315$ mV and $V_L = V_R = 370$ mV. This data refers to a device with $W = 150$ nm and $d = 80$ nm (see image in (a)).

6.3 Double-layer single quantum dot

In this section we present transport measurements on a DLG device. The DLG fabrication scheme was developed with the purpose to further reduce cross-coupling effects and obtain a more efficient and independent tunability of the characteristic QD parameters. Figure 6.3 (a) shows the scanning electron micrograph of a DLG QD device. The plunger and the barrier gate (colorized in green) were fabricated first. To this aim, e-beam lithography was used, followed by Al deposition. Then, following Angus *et al.* [132], the barrier gates were oxidized by annealing on a hot plate at 180 °C for 10 min. (This Al oxidation technique creates an Al_2O_3 layer over the metal gates making the deposition of an insulating layer unnecessary.) The following step consisted in the definition of the top gate (colorized in red), again by e-beam lithography and Al deposition. We verified the absence of leakage between the barrier gates and the top gate.

We fabricated DLG devices such as the one shown in Fig. 6.3 (a), varying the barrier-gate width, d, and the top-gate width, W. The distance between the barrier gates was set equal to W. Figure 6.3 (b) shows a $G(V_{ds},V_C)$ measurement taken on a DLG device with (d, W) = (80 nm, 150 nm) at 300 mK. The barrier gate voltages V_L and V_R are much smaller than those used in the previous devices, which is a consequence of the much stronger capacitive coupling. The observed Coulomb diamonds are irregular, denoting the formation of unintentional QDs, and the charge noise is high. From the upper diamond in Fig. 6.3 (b), the charging energy and the α factor are estimated to be $E_c \sim 650$ μV and $\alpha = 0.0134$ eV/V. Contrary to our expectation, V_C has a significant effect on the tunnel barriers.

Before depositing the gate oxide , the samples were cleaned with HF. We used HF 1% for SLQDs and HF 2% for the DLQDs. We did that with the idea that we could obtain a cleaner surface before gate deposition, and hence an eventually lower charge noise level. Unfortunately, charge switching did not improve and all devices turned out to be noisy. On the other hand, we measured different threshold voltages: $V_{tg} = -2.1$ V for SLG1, $V_{tg} = -0.68$ V for SLG2, and $V_{tg} = -0.315$ V for the DLG device. In fact, all DLG devices showed a low threshold voltage, which may be an indirect evidence of a cleaner dielectric/heterostructure interface.

6.4 Conclusion

In conclusion, we succeeded in the realization of the first QD devices based on Ge/SiGe heterostructure. This is a first step towards the real-

ization of largely integrated qubit systems with HH spins in Ge QDs. To make these QD devices, we followed two approaches: single-layer gates and double-layer gates (simple fabrication and higher tunability, respectively). However, significant charge switching was found in both types of devices preventing in-depth investigation of the QD electronic properties. In the prospect of developing quantum dots for spin qubits, the priority is now to reduce charge noise. Switching could be suppressed by improving the interface quality. This could be achieved by reducing the time delay between HF cleaning and ALD deposition of the dielectric. So far the HF cleaning and the ALD process could not be carried out in the same cleanroom, and the transfer from one cleanroom to the other took about 15 minutes. In principle, this delay may not be critical since our heterostructure is capped by a Si layer, and HF should passivate the surface with Si-H terminations that could survive for more than 15 min. Additional studies are necessary to clarify this issue.

Chapter 7

Conclusion

7.1 Summary

In this PhD thesis, I have presented experimental research on hole transport in low-dimensional systems fabricated from Ge/$Si_{0.2}Ge_{0.8}$ heterostructures. This so-far barely explored material was investigated in view of its potential applications in quantum spintronics and quantum computing hardware. Key properties of SiGe heterostructures are large spin-orbit interaction associated with valence band states, a small in-plane effective mass, anisotropic g-factors, reduced hyperfine interaction resulting from the p-wave symmetry of hole Bloch functions, and the ability for forming low-resistive contacts with superconducting metals, which should open the way to the realization of hybrid superconductor-semiconductor structures and, eventually, Majorana fermion devices for topological quantum computing.

An important part of my PhD work was devoted to developing the fabrication recipes for the realization of Ge-based nanoelectronic devices. At first, I focused on relatively large devices, which I used to test basic electronic properties and to test and benchmark the fabrication processes (mesa etching, contact definition, deposition of dielectric layers, metal gates, etc.). I started by designing optical masks for photolithography. Next, I developed the dry etching protocols, which I then applied to the definition of mesa structures and ohmic contacts. Contact resistances were also measured before and after ALD, which clarified that during the ALD the contacts were annealed, resulting in improved contact resistances. Finally, we optimized conditions for electron-beam lithography depending on the metals to be deposited. These fabrication tests enables us to perform unprecedented studies of low-dimensional structures based on Ge.

The basic electronic properties of the Ge heterostructures were initially

characterized by Hall measurements. I explored and evaluated two types of heterostructures: one where the Ge QW is on the surface and one where it is buried in the heterostructure, 70 nm below the surface. In spite of their reduced mobility due to surface scattering, surface-Ge heterostructures have the advantage of being more easily accessible to superconducting contacts. In addition, they enable the the realization of MOS-type structures where large vertical electric fields can be applied resulting in strong Rashba spin-orbit coupling. From the measurements of the Hall-bar devices made from surface-Ge heterostructures, I observed a magneto-conductivity peak at zero magnetic field, which is due to the weak anti-localization (WAL) effect. I analyzed the peak with Iordanskii-Lyanda Geller-Pikus theory for the k-cubic Rashba spin orbit interaction (which is expected for HHs) [82] and, thereby, obtained spin relaxation time, phase relaxation time and spin splitting energy at zero magnetic field. The spin splitting energy is estimated to be ~ 1 meV and such a large spin splitting is an order of magnitude greater than the one calculated from tight-binding simulations, an effect that can be ascribed to the atomic structure of the Ge/Al_2O_3 interface. The simulations also demonstrate that the interface roughness between the Ge QW and the gate oxide kills k-linear Rashba spin-orbit interaction owing to the induced symmetry breaking in the QW.

Following this instructive study, I redirected my interest from surface-Ge heterostructures to buried-Ge ones. This was motivated by the massive gain in mobility, which is a key parameter in the prospect of realizing quantum electronic devices in which the motion of holes is not affected by disorder. In fact, the studied surface-Ge heterostructure exhibited a mobility of at most ~ 4000 cm^2/Vs at 300 mK and for densities of about 2×10^{11} cm^2/Vs. In undoped buried Ge-QW heterostructures, mobility as high as 1.8×10^5 cm^2/Vs could be achieved at the same temperature 300 mK and three times lower carrier density.

I introduced some steps of e-beam lithography in order to fabricate the fine metal gate structures necessary to electrostatically define quantum-wire and quantum-dot devices. The quantum-wire devices were designed with varying channel lengths in order to explore the characteristic length scale for ballistic conduction. I was able to measure ballistic one-dimensional transport in Ge channels as long as ~ 600 nm. This result is encouraging in the prospect of realizing one-dimensional devices such as those needed for the emergence of Majorana fermions. I also investigated the hole g-factor anisotropy in Ge one-dimensional wires. Magneto-transport measurements gave out-of-plane g-factors up to 15 and in-plane g-factors below 1. This anisotropy is expected for HHs in the two-dimensional limit, therefore indicating that first hole subbands have a dominant HH character.

Finally, I began to explore the possibility to realize also zero-dimensional structures, namely hole quantum dots, in view of their possible use as spin qubits. To this aim, I modified the gate design used to define one-dimensional nanowires. I was able to observe clear Coulomb blockade oscillations, which are characteristic signatures of single-hole tunneling.

7.2 Perspectives

To conclude, I would like to discuss the possible prospects of my research work. The experiments carried out on the surface-Ge QW heterostructure have demonstrated the existence of a strong Rashba spin-orbit interaction. This conclusion may apply also to the buried-Ge QW heterostructures where remarkable one-dimensional ballistic transport could be observed. This question does not have an answer at the moment. In principle, weak anti-localization measurements similar to those presented in Chapter 4 could be carried out on buried-Ge heterostructures. However, this did not seem so straightforward. I performed a few attempts in this direction but no weak-antilocalization features could be clearly observed, most likely due to an excessive noise level. I believe there could be room for improvement though, and it may be worth pursuing further experimental efforts. My experiments in buried Ge quantum wires revealed a pronounced heavy-hole character of the one-dimensional subbands. In the prospect of realizing helical one-dimensional systems, a significant mixing between heavy- and light-hole components would be necessary. This may be engineered in different ways, e.g. by laterally squeezing the one-dimensional wire, or by introducing a tensile strain in the Ge well. Ge-based nanowire structures (in particular, Ge/Si core/shell nanowires) where proposed as a promising platform for the realization of Majorana devices. To this aim, electrostatically defined Ge wires hosting one-dimensional helical states should be coupled to superconducting metals providing a sufficiently strong superconducting proximity effect. Aluminium-based Josephson field-effect transistors made from a SiGe heterostructure with a buried Ge QW were very recently reported by Hendrickx *et al.* [58], a research team at the Delft University of Technology. In that work, Al was deposited on the surface of the heterostructure and contact to the Ge QW, located 22 nm below the surface, was achieved as a result of the Al diffusion during the ALD process for the deposition of the gate oxide. These results represent an encouraging demonstration of principle towards hybrid semiconductor-superconductor devices based on high-mobility SiGe heterostructures (e.g. gatemons [133, 134] or, eventually, topological superconducting qubits [49, 45]). Towards the end

of my PhD I was able to test a few device designs for the realization of Ge-based quantum-dot devices. The results are encouraging and pave the way to further developments in the direction of more complex device structures. Spin qubits are the main target application. In this perspective, the Rashba spin-orbit interaction existing in Ge QWs could be exploited for electric-field-driven spin manipulation [6, 135].

Measuring the spin-orbit interaction strength in QDs should be easier than in 1D channels [6, 136]. Electric-dipole spin resonance can be casted into a g-matrix formalism and measuring Rabi and Larmor frequencies for a set magnetic field directions can provide important insight on the underlying spin-orbit mechanism [135]. Spin rotation frequencies of several hundred MHz can be expected in Ge nanostructures[36, 137]. In a recent experiment performed on quantum dots confined in self-assembled Ge hut nanowires, Rabi frequencies as high as 40 MHz were obtained [18]. Similar types of experiments could be envisioned in double quantum dots fabricated from buried-Ge heterostructures. To enable this, however, a critical step is to improve the charge stability of the devices, well beyond the level achieved so far. Based on the tests I could perform in a limited amount of available time, and on the encouraging results reported by Hendrickx *et al.* [58], I am quite confident that a sufficiently high charge stability can be achieved, by optimizing the gate dielectric and the heterostructure (composition and thickness of the different layers, including the capping layer). This would open ample possibilities of development towards spin qubit devices and quantum spintronic devices in general.

Appendix A

Device fabrication

We presented in previous chapters the basic fabrication procedures for many Ge devices presented in this thesis. The details of the techniques are developed in this appendix. General information about each fabrication step is given at first, followed by specific fabrication recipe for each device. All the processes are performed at lower than 400°C in order not to relax the strain in the Ge QW.

A.1 Fabrication techniques

Sample cleaning/Lift-off/HF cleaning

To ensure the cleanness of the sample surface is crucial in the fabrication of semiconductor device. Impurities at the surface trap charges which screen electric field from gate and cause noises and hysteresis in conductance-gate voltage characteristics. The way how we clean our samples is explained as follows.

A sample is put in a beaker filled with acetone and cleaned by ultrasonication for 5 min. Afterwards, it is repeated with new beakers filled with acetone and IPA in this order respectively. After drying sample with N_2 gun, the sample is baked on a hot plate set to be at a temperature higher than 100 °C for 5 min. The last step is important because residual IPA prevents photo-resist from stacking on sample.

Lift-off, removing metal on patterned resist, is also done in the same way except that, instead of ultra sound, pipette is sometimes used to avoid breaking nanostructures on the sample. That is indicated by "(pipette)" in the recipes below. In addition, before starting the lift-off, the sample is left in acetone overnight, which makes it easier to peel metal to be removed.

Moreover, putting the sample into hot acetone at 40°C for one hour helps lift-off of nano-size structure.

HF cleaning is done to remove native oxide on the surface before ohmic contact and gate oxide deposition. A sample is dipped into a beaker filled with HF and de-ionized water (DIW) for several minutes, in this order respectively, which is repeated twice. This HF cleaning must improve the interface quality but unfortunately it is necessary to transfer a cleaned sample to another clean room to deposit gate oxide. To keep it clean, we use a bottle with DIW to bring samples. This point must be considered to improve our device.

Photolithography

Photolithography is one of most-frequently used techniques in semiconductor device fabrication. By use of this technique, one can pattern designs (usually) to be etched or metalized on a chip. The idea for the patterning is based on the nature of the materials called photo-resist, which change its own resistance against acid after applying ultraviolet (UV). One can cover sample with the photo-resist and put a glass board with patterned metal (photo-mask) over the sample. When UV is applied to it, UV can pass through the no-metal part of the glass while the other part block the UV, which turns out that the resist masked by the pattern is exposed. By dipping the sample into the acid suitable for the photo-resist after the exposure, the photo-resist patterned defined by the mask is obtained. The polarity of the resist is determined by the type of the resist (the exposed part of a "positive" resist can be removed while non-exposed part of a "negative" resist is).

The procedures for our photolithography are as follows. The sample is coated with photo-resist by means of spin-coater. A positive photo-resist AZ1512HS is normally used. The sample is fixed with vacuum and rotated at 4000 rpm for 60 s as soon as possible after covering it with resist droplets. After baking it at 100 °C for 90 s (prebake), UV exposure is done with a mask aligner MJB4 (SUSS MicroTec). Exposure time is 25 s normally but it depends on the size of pattern. AZ developer diluted with DIW (1:1) is used for the development. The development is stopped by dipping sample in DIW, followed by rinsing with running DIW for 5 min. Normally, development time is 30 s but, when a lot of resist is developed (for example, mesa pattern needs to cover small area compared with the chip surface), the time is extended up to $\sim$15 s.

Other photo-resists are sometimes used. A negative resist AZ2070 used (only) for mesa of Ge-surface Hall bar device. In addition, a positive photo-resist UV5, which has a better resolution and thinner thickness than AZ1512HS, is also used to make fine structures (< 10 μm). In this case, deep UC (DUV) is used instead. The exposure time, the baking time and development time for both resist are different than the ones of AZ1512HS. UV5 requires baking after exposure (postbake) as well. The details are written in the recipes below.

Electron beam evaporation

Electron beam evaporation was used to metalize our sample. Electron beam is applied to a target metal and the surface temperature at the incident point increases. When the temperature reaches the boiling point, the metal begins to be evaporated. In the combination with photolithography, one can obtain a patterned metal by evaporating metal on the sample with patterned resist. This is because the photo-resist can be removed by acetone and therefore only the metal directly on the sample surface remain.

Ar etching, or ion milling, sometimes proceeds the evaporation to remove the resist residue on the sample surface where photo-resist has been removed. We did the Ar etching and used neutralized Ar to avoid charging the oxide before fine gate deposition.

Reactive ion etching

Etching of the sample surface is possible using reactive ion etching (RIE), a common dry etching technique. In this PhD work, an inductively coupled plasma (ICP) RIE setup was used in all dry etching processes (Oxford Instruments Plasma System 100 ICP-RIE). In this machine, a DC bias voltage is applied to the stage underneath the sample forcing the plasma to move perpendicular to the sample surface, and hence leading to an anisotropic (quasi-vertical) etching. This contrasts with wet-etching processes, which offer limited control on the directionality of the etching.

For the etching of SiGe, we used Cl_2, N_2 and O_2 gases. The etching rate for $Si_{0.2}Ge_{0.8}$ was initially measured and optimized. We developed recipes for the etching of the mesa structures as well as for the etching of Ohmic-contact regions prior to metal (Pt) deposition. The latter etching process was necessary in order to have the metal deposited directly on the

Ge quantum-well layer. In this case, O_2 was not employed to avoid the oxidation of Ge, which is supposed to prevent good ohmic contacts.

- **Mesa etching**: Etching rate for $Si_{0.2}Ge_{0.8}$ is 42 nm/min. The flow rate of $Cl_2/N_2/O_2$ is 50/25/10 sccm. Pressure in chamber is 25 mTorr. Stage temperature is 20 °C. RF/ICP power is 20/50 W.

- **Ohmic etching**: Etching rate for $Si_{0.2}Ge_{0.8}$ is 19 nm/min. The flow rate of $Cl_2/N_2/O_2$ is 25/12/0 sccm. Pressure in chamber is 25 mTorr. Stage temperature is 20 °C. RF/ICP power is 10/25 W.

ALD

Atomic layer deposition (ALD) technique is, as obvious from its name, used to deposit materials (in our case dielectrics) with atomically precise control, i.e. one atomic layer after the other. The deposition mechanism can be explained as follows: first, a precursor (*e.g.*, H_2O) is filled into a sample chamber and absorbed on the surface of the sample; then, after purging the water vapor, a second precursor (*e.g.*, trimethylaluminium (TMA)) is supplied; reaction with the H_2O molecules adsorbed on the sample surface results in the formation of a monoloayer of Al_2O_3. This cycle is repeated until the desired dielectric thickness is reached. During this process, the sample is heated by a hot plate (at 250°C , in our case). This leads to an unintentional, yet helpful, annealing of the ohmic contacts. ALD was performed in a Cambridge Nanotech Fiji F200 system.

Before ALD, HF cleaning has been done to remove native oxide on the sample surface. However, since the HF cleaning is not allowed for us in the clean room where ALD machine is located, we have done it in another clean room and transferred the sample from one to the other, keeping it in DIW. DIW cleaning is done just before the gate oxide deposition to remove the particles since the sample is supposed to be contaminated.

EBL

Electron beams can be used for lithography with higher resolution than UV because of its smaller wavelength and thereby the sub-100 nm structure is easily achievable. In our research, Poly(methyl methacrylate) (PMMA) is chosen as the EB resist because of its cleanness compared with ZEP520A (Nippon Zeon Co.). PMMA with the various concentrations have different thickness: PMMA4%950K 200nm, PMMA2%950K 80nm and PMMA4%200K 80nm. The choice of resist is decided from the point of view of resolution and thickness. When one makes a difficult lift-off, *e.g.*, lift-off for aluminium, a

thick resist or a double layer resist is helpful. PMMA with MMA (thickness: 500nm) is also used for lift-off of very thick metal ($\sim$ 200nm). We have utilized JEOL JBX 6300 FS for all the devices with fine gates.

A.2 Gated Hall bar device made from Ge-surface hetetrostructure

Alignment mark deposition

Chip cleaning:
Acetone 5min twice, IPA 5min, Baking 120°C 5min
Resist coating:
AZ1512HS 4000rpm 60s, Prebake 100°C 90s
Photolithography:
25s
Development:
AZ developer 1:1 45s, DIW 15s, Running DIW 5min
EB evaporation:
Ti/Au 10/50nm
Lift off:
Acetone 5min twice, IPA 5min, Baking 120°C 5min

Mesa formation

Chip cleaning:
Acetone 5min twice, IPA 5min, Baking 120°C 5min
Resist coating:
AZ2070 3500rpm 60s, Prebake 100°C 90s
Photolithography:
35s, Postbake 110°C 60s
Development:
MF26 120s, DIW 15s, Running DIW 5min
Dry etching:
Recipe for mesa
Chip cleaning:
Acetone 5min twice, IPA 5min, Baking 120°C 5min

Ohmic contact deposition

Chip cleaning:
Acetone 5min twice, IPA 5min, Baking 120°C 5min
Resist coating:
AZ1512HS 4000rpm 60s, Prebake 100°C 90s
Photolithography:
35s
Development:
AZ developer 1:1 45s, DIW 15s, Running DIW 5min
EB evaporation:
Ar etching 250V 30s, Pt 60nm
Lift off:
Acetone 5min twice, IPA 5min, Baking 120°C 5min

Gate oxide deposition

HF cleaning:
(HF 1% 1min, DIW 1min) twice (Transfer the chip to another clean room.)
ALD:
Al_2O_3 (TMA) 250°C 30nm (Thermal deposition)

Top gate deposition

Chip cleaning:
Acetone 5min twice, IPA 5min, Baking 120°C 5min
Resist coating:
PMMA 950K 4% 4000rpm 60s, Prebake 180°C 5min
EB lithography:
100keV 1nA 1000μC/cm^2
Development:
MIBK:IPA 1:3 45s, IPA 30s
EB evaporation:
Ar etching 250V 30s, Ti/Au 10/50nm
Lift off:
Acetone 5min twice, IPA 5min

A.3 Gated Hall bar device made from buried Ge/SiGe hetetrostructure

Alignment mark deposition

Chip cleaning:
Acetone 5min twice, IPA 5min, Baking 120°C 5min
Resist coating:
AZ1512HS 4000rpm 60s, Prebake 100°C 90s
Photolithography:
25s
Development:
AZ developer 1:1 30s, DIW 15s, Running DIW 5min
EB evaporation:
Ti/Au 10/50nm
Lift off:
Acetone 5min twice, IPA 5min, Baking 120°C 5min

Mesa formation

Chip cleaning:
Acetone 5min twice, IPA 5min, Baking 120°C 5min
Resist coating:
AZ1512HS 4000rpm 60s, Prebake 100°C 90s
Photolithography:
25s
Development:
AZ developer 1:1 45s, DIW 15s, Running DIW 5min
Dry etching:
Recipe for mesa 150s
Chip cleaning:
Acetone 5min twice, IPA 5min, Baking 180°C 5min

Ohmic contact deposition

Chip cleaning:
Acetone 5min twice, IPA 5min, Baking 120°C 5min
Resist coating:
AZ1512HS 4000rpm 60s, Prebake 100°C 90s
Photolithography:
25s

Development:
AZ developer 1:1 30s, DIW 15s, Running DIW 5min
Dry etching:
Recipe for contact 77s, DIW cleaning 30s
EB evaporation:
Ar etching 250V 24s, Pt 77nm
Lift off:
Acetone 5min twice, IPA 5min, Baking 120°C 5min

Gate oxide deposition

HF cleaning:
(HF 1% 1min, DIW 1min) twice (Transfer the chip to another clean room.)
ALD:
Al_2O_3 (TMA) 250°C 30nm (Thermal deposition)

Top gate deposition

Chip cleaning:
Acetone 5min twice, IPA 5min, Baking 120°C 5min
Resist coating:
AZ1512HS 4000rpm 60s, Prebake 100°C 90s
Photolithography:
35s
Development:
AZ developer 1:1 30s, DIW 15s, Running DIW 5min
EB evaporation:
Ar etching 250V 24s, Ti/Au 10/50nm
Lift off:
Acetone 5min twice, IPA 5min

A.4 QPC device made from buried Ge/SiGe hetetrostructure

Alignment mark deposition

Chip cleaning:
Acetone 5min twice, IPA 5min, Baking 120°C 5min

Resist coating:
AZ1512HS 4000rpm 60s, Prebake 100°C 90s
Photolithography:
25s
Development:
AZ developer 1:1 35s, DIW 15s, Running DIW 5min
EB evaporation:
Cr/Au 10/50nm
Lift off:
Acetone overnight, Acetone 5min twice, IPA 5min, Baking 120°C 5min

Mesa formation

Chip cleaning:
Acetone 5min twice, IPA 5min, Baking 120°C 5min
Resist coating:
AZ1512HS 4000rpm 60s, Prebake 100°C 90s
Photolithography:
25s
Development:
AZ developer 1:1 45s, DIW 15s, Running DIW 5min
Dry etching:
Recipe for mesa 5min
Chip cleaning:
Acetone 5min twice, IPA 5min, Baking 180°C 5min

Ohmic contact deposition

Resist coating:
AZ1512HS 4000rpm 60s, Prebake 100°C 90s
Photolithography:
25s
Development:
AZ developer 1:1 30s, DIW 15s, Running DIW 5min
Dry etching:
Recipe for contact 77s/77s DIW cleaning 30s
HF cleaning:
(HF 1% 1min, DIW 1min) twice
EB evaporation:
Ar etching 250V 30s, Pt 77nm

Lift off:
Acetone 5min twice, IPA 5min, Baking 120°C 5min

Gate oxide deposition

HF cleaning:
(HF 1% 1min, DIW 1min) twice (Transfer the chip in water to another clean room.)
ALD:
Al_2O_3 (TMA) 250°C 30nm (Plasma deposition)

Deposition of fine gates in first layer

Chip cleaning:
Acetone 5min twice, IPA 5min, Baking 180°C 5min
Resist coating:
PMMA4%950K 4000rpm 60s, Prebake 180°C 5min
EB lithography:
100keV, 500pA, 1350μC/cm^2
Development:
MIBK:IPA=1:3 30s, IPA 60s
EB evaporation:
Ar etching 240V 1min (0°), Ti/Au 10/25nm
Lift off:
Acetone overnight and 40 °C 1hour, Acetone 5min(pipette) twice, IPA 5min(pipette), Baking 180°C 5min

Deposition of fine gates in second layer

Resist coating:
PMMA/MMA617-8 4000rpm 60s, Prebake 200°C 5min, Cooling down RT 5min, PMMA4%950K 4000rpm 60s, Prebake 180°C 5min
EB lithography:
100keV, 500pA, 1500μC/cm^2
Development:
MIBK:IPA=1:3 60s, IPA 30s
EB evaporation:
Ar etching 250V 1min, Pt 200nm
Lift off:
Acetone overnight and 40 °C 1hour, Acetone 5min(pipette), Acetone 5min, IPA 5min, Baking 120°C 2min

A.5 QD device made from buried Ge/SiGe hetetrostructure

Alignment mark deposition

Chip cleaning:
Acetone 5min twice, IPA 5min, Baking 120°C 5min
Resist coating:
AZ1512HS 4000rpm 60s, Prebake 100°C 90s
Photolithography:
25s
Development:
AZ developer 1:1 30s, DIW 15s, Running DIW 5min
EB evaporation:
Cr/Au 10/50nm
Lift off:
Acetone 5min twice, IPA 5min, Baking 120°C 5min

Mesa formation

Chip cleaning:
Acetone 5min twice, IPA 5min, Baking 120°C 5min
Resist coating:
AZ1512HS 4000rpm 60s, Prebake 100°C 90s
Photolithography:
45s
Development:
AZ developer 1:1 45s, DIW 15s, Running DIW 5min
Dry etching:
Recipe for mesa 5min
Chip cleaning:
Acetone 5min twice, IPA 5min, Baking 180°C 5min

Ohmic contact deposition

Chip cleaning:
Acetone 5min twice, IPA 5min, Baking 120°C 5min
Resist coating:
AZ1512HS 4000rpm 60s, Prebake 100°C 90s
Photolithography:
25s

Development:
AZ developer 1:1 30s, DIW 15s, Running DIW 5min
Dry etching:
Recipe for contact 77s/77s
HF cleaning:
(HF 2% 2min, DIW 2min) twice
EB evaporation:
Ar etching 250V 30s, Pt 50nm
Lift off:
Acetone overnight and 40 °C 1hour, Acetone 5min, IPA 5min, Baking 120°C 5min

Gate oxide deposition

HF cleaning:
(HF 2% 2min, DIW 2min) twice (Transfer the chip in water to another clean room.)
Chip cleaning:
DIW 5min
ALD:
Al_2O_3 (TMA) 250°C 30nm (Plasma deposition)

Metal patch deposition

Chip cleaning:
Acetone 5min twice, IPA 5min, Baking 180°C 5min
Resist coating:
UV5 4000rpm 60s, Prebake 130°C 90s
Photolithography:
1.3s (DUV), Postbake 130°C 60s
Development:
AZ326MF 37s, DIW 15s, Running DIW 5min
EB evaporation:
Ar etching 240V 30s (0°), Ti/Au 5/10nm
Lift off:
Acetone overnight and 40 °C 1hour, Acetone 5min(pipette) twice, IPA 5min, Baking 120°C 5min

Gate pad deposition

Chip cleaning:
Acetone 5min twice, IPA 5min, Baking 180°C 5min
Resist coating:
AZ1512HS 4000rpm 60s, Prebake 100°C 90s
Photolithography:
30s (vacuum contact)
Development:
AZ developer 1:1 30s, DIW 15s, Running DIW 5min
EB evaporation:
Ti/Au 10/200nm
Lift off:
Acetone overnight and 40 °C 1hour, Acetone 5min(pipette) twice, IPA 5min(pipette), Baking 120°C 5min

Deposition of fine gates in first layer

Chip cleaning:
Acetone 5min twice, IPA 5min, Baking 180°C 5min
Resist coating:
PMMA4%200K 4000rpm 60s, Prebake 180°C 5min, Cooling down RT 5min, PMMA2%950K 4000rpm 60s, Prebake 180°C 5min
EB lithography:
100keV, 500pA, 1600μC/cm^2
Development:
MIBK:IPA=1:3 30s, IPA 60s
EB evaporation:
Ar etching 240V 30s (0°), Al 50nm
Lift off:
Acetone overnight and 40 °C 1hour, Acetone 5min(pipette) twice, IPA 5min(pipette), Baking 180°C 10min

Deposition of fine gates in second layer

Resist coating:
PMMA4%200K 4000rpm 60s, Prebake 180°C 5min, Cooling down RT 5min, PMMA2%950K 4000rpm 60s, Prebake 180°C 5min
EB lithography:
100keV, 500pA, 1600μC/cm^2

Development:
MIBK:IPA=1:3 30s, IPA 60s

EB evaporation:
Ar etching 240V 30s (0°), Al 60nm

Lift off:
Acetone overnight and 40 °C 1hour, Acetone 5min(pipette) twice, IPA 5min(pipette)

Appendix B

List of matrix products of total angular momentum operators ($J = 3/2$)

$$J_x = \begin{pmatrix} 0 & \frac{\sqrt{3}}{2} & 0 & 0 \\ \frac{\sqrt{3}}{2} & 0 & 1 & 0 \\ 0 & 1 & 0 & \frac{\sqrt{3}}{2} \\ 0 & 0 & \frac{\sqrt{3}}{2} & 0 \end{pmatrix}, \quad J_y = \begin{pmatrix} 0 & -i\frac{\sqrt{3}}{2} & 0 & 0 \\ i\frac{\sqrt{3}}{2} & 0 & -i & 0 \\ 0 & i & 0 & -i\frac{\sqrt{3}}{2} \\ 0 & 0 & i\frac{\sqrt{3}}{2} & 0 \end{pmatrix}, \tag{B.1}$$
$$J_z = \begin{pmatrix} \frac{3}{2} & 0 & 0 & 0 \\ 0 & \frac{1}{2} & 0 & 0 \\ 0 & 0 & -\frac{1}{2} & 0 \\ 0 & 0 & 0 & -\frac{3}{2} \end{pmatrix},$$

$$J_x^2 = \begin{pmatrix} \frac{3}{4} & 0 & \frac{\sqrt{3}}{2} & 0 \\ 0 & \frac{7}{4} & 0 & \frac{\sqrt{3}}{2} \\ \frac{\sqrt{3}}{2} & 0 & \frac{7}{4} & 0 \\ 0 & \frac{\sqrt{3}}{2} & 0 & \frac{3}{4} \end{pmatrix}, \quad J_y^2 = \begin{pmatrix} \frac{3}{4} & 0 & -\frac{\sqrt{3}}{2} & 0 \\ 0 & \frac{7}{4} & 0 & -\frac{\sqrt{3}}{2} \\ -\frac{\sqrt{3}}{2} & 0 & \frac{7}{4} & 0 \\ 0 & -\frac{\sqrt{3}}{2} & 0 & \frac{3}{4} \end{pmatrix}, \tag{B.2}$$
$$J_z^2 = \begin{pmatrix} \frac{9}{4} & 0 & 0 & 0 \\ 0 & \frac{1}{4} & 0 & 0 \\ 0 & 0 & \frac{1}{4} & 0 \\ 0 & 0 & 0 & \frac{9}{4} \end{pmatrix}$$

$$J_xJ_y = \begin{pmatrix} i\frac{3}{4} & 0 & -i\frac{\sqrt{3}}{2} & 0 \\ 0 & \frac{i}{4} & 0 & -i\frac{\sqrt{3}}{2} \\ i\frac{\sqrt{3}}{2} & 0 & \frac{-i}{4} & 0 \\ 0 & i\frac{\sqrt{3}}{2} & 0 & -i\frac{3}{4} \end{pmatrix}, \; J_yJ_z = \begin{pmatrix} 0 & -i\frac{\sqrt{3}}{4} & 0 & 0 \\ i\frac{3\sqrt{3}}{4} & 0 & \frac{i}{2} & 0 \\ 0 & \frac{i}{2} & 0 & i\frac{3\sqrt{3}}{4} \\ 0 & 0 & -i\frac{\sqrt{3}}{4} & 0 \end{pmatrix},$$
$$J_zJ_x = \begin{pmatrix} 0 & \frac{3\sqrt{3}}{4} & 0 & 0 \\ \frac{\sqrt{3}}{4} & 0 & \frac{1}{2} & 0 \\ 0 & -\frac{1}{2} & 0 & -\frac{\sqrt{3}}{4} \\ 0 & 0 & -\frac{3\sqrt{3}}{4} & 0 \end{pmatrix} \tag{B.3}$$

$$\{J_xJ_y\} = \frac{i\sqrt{3}}{2}\begin{pmatrix} 0 & 0 & -1 & 0 \\ 0 & 0 & 0 & -1 \\ 1 & 0 & 0 & 0 \\ 0 & 1 & 0 & 0 \end{pmatrix}, \; \{J_yJ_z\} = \frac{i\sqrt{3}}{2}\begin{pmatrix} 0 & -1 & 0 & 0 \\ 1 & 0 & 0 & 0 \\ 0 & 0 & 0 & 1 \\ 0 & 0 & -1 & 0 \end{pmatrix},$$
$$\{J_zJ_x\} = \frac{\sqrt{3}}{2}\begin{pmatrix} 0 & 1 & 0 & 0 \\ 1 & 0 & 0 & 0 \\ 0 & 0 & 0 & -1 \\ 0 & 0 & -1 & 0 \end{pmatrix}, \text{ where } \{AB\} = \frac{1}{2}(AB + BA) \tag{B.4}$$

$$J_x^3 = \begin{pmatrix} 0 & \frac{7\sqrt{3}}{8} & 0 & \frac{3}{4} \\ \frac{7\sqrt{3}}{8} & 0 & \frac{5}{2} & 0 \\ 0 & \frac{5}{2} & 0 & \frac{7\sqrt{3}}{8} \\ \frac{3}{4} & 0 & \frac{7\sqrt{3}}{8} & 0 \end{pmatrix}, \quad J_y^3 = \begin{pmatrix} 0 & -i\frac{7\sqrt{3}}{8} & 0 & i\frac{3}{4} \\ i\frac{7\sqrt{3}}{8} & 0 & -i\frac{5}{2} & 0 \\ 0 & i\frac{5}{2} & 0 & -i\frac{7\sqrt{3}}{8} \\ -i\frac{3}{4} & 0 & i\frac{7\sqrt{3}}{8} & 0 \end{pmatrix},$$
$$J_z^3 = \begin{pmatrix} \frac{27}{8} & 0 & 0 & 0 \\ 0 & \frac{1}{8} & 0 & 0 \\ 0 & 0 & -\frac{1}{8} & 0 \\ 0 & 0 & 0 & -\frac{27}{8} \end{pmatrix} \tag{B.5}$$

References

[1] G. E. Moore. Cramming more components onto integrated circuits, reprinted from electronics. *IEEE solid-state circuits society newsletter*, **20** 33, 2006.

[2] D. Deutsch. Quantum theory, the church–turing principle and the universal quantum computer. *Proceedings of the Royal Society of London A: Mathematical, Physical and Engineering Sciences*, **400** 97, 1985.

[3] P. W. Shor. Polynomial-time algorithms for prime factorization and discrete logarithms on a quantum computer. *SIAM Journal on Computing*, **26** 1484, 1997.

[4] L. K. Grover. A fast quantum mechanical algorithm for database search. In *Proceedings of the Twenty-eighth Annual ACM Symposium on Theory of Computing*, STOC '96, pp. 212–219. ACM, New York, NY, USA, 1996.

[5] F. H. L. Koppens, C. Buizert, K. J. Tielrooij, I. T. Vink, K. C. Nowack, T. Meunier, L. P. Kouwenhoven, and L. M. K. Vandersypen. Driven coherent oscillations of a single electron spin in a quantum dot. *Nature*, **442** 766, 2006.

[6] K. C. Nowack, F. H. L. Koppens, Y. V. Nazarov, and L. M. K. Vandersypen. Coherent control of a single electron spin with electric fields. *Science*, **318** 1430, 2007.

[7] M. Pioro-Ladrière, T. Obata, Y. Tokura, Y.-S. Shin, T. Kubo, K. Yoshida, T. Taniyama, and S. Tarucha. Electrically driven single-electron spin resonance in a slanting zeeman field. *Nature Physics*, **4** 776, 2008.

[8] D. Loss and D. P. DiVincenzo. Quantum computation with quantum dots. *Phys. Rev. A*, **57** 120, 1998.

[9] J. R. Petta, A. C. Johnson, J. M. Taylor, E. A. Laird, A. Yacoby, M. D. Lukin, C. M. Marcus, M. P. Hanson, and A. C. Gossard. Coherent manipulation of coupled electron spins in semiconductor quantum dots. *Science*, **309** 2180, 2005.

[10] D. P. DiVincenzo, D. Bacon, J. Kempe, G. Burkard, and K. B. Whaley. Universal quantum computation with the exchange interaction. *Nature*, **408** 339, 2000.

[11] L. Gaudreau, G. Granger, A. Kam, G. C. Aers, S. A. Studenikin, P. Zawadzki, M. Pioro-Ladrière, Z. R. Wasilewski, and A. S. Sachrajda. Coherent control of three-spin states in a triple quantum dot. *Nature Physics*, **8** 54, 2011.

[12] K. Ono, D. G. Austing, Y. Tokura, and S. Tarucha. Current rectification by pauli exclusion in a weakly coupled double quantum dot system. *Science*, **297** 1313, 2002.

[13] J. M. Elzerman, R. Hanson, L. H. Willems van Beveren, B. Witkamp, L. M. K. Vandersypen, and L. P. Kouwenhoven. Single-shot read-out of an individual electron spin in a quantum dot. *Nature*, **430** 431, 2004.

[14] K. D. Petersson, L. W. McFaul, M. D. Schroer, M. Jung, J. M. Taylor, A. A. Houck, and J. R. Petta. Circuit quantum electrodynamics with a spin qubit. *Nature*, **490** 380, 2012.

[15] J. I. Colless, A. C. Mahoney, J. M. Hornibrook, A. C. Doherty, H. Lu, A. C. Gossard, and D. J. Reilly. Dispersive readout of a few-electron double quantum dot with fast rf gate sensors. *Phys. Rev. Lett.*, **110** 046805, 2013.

[16] E. A. Laird, F. Pei, and L. P. Kouwenhoven. A valley-spin qubit in a carbon nanotube. *Nature Nanotechnology*, **8** 565, 2013.

[17] B. M. Maune, M. G. Borselli, B. Huang, T. D. Ladd, P. W. Deelman, K. S. Holabird, A. A. Kiselev, I. Alvarado-Rodriguez, R. S. Ross, A. E. Schmitz, M. Sokolich, C. A. Watson, M. F. Gyure, and A. T. Hunter. Coherent singlet-triplet oscillations in a silicon-based double quantum dot. *Nature*, **481** 344, 2012.

[18] H. Watzinger, J. Kukučka, L. Vukušić, F. Gao, T. Wang, F. Schäffler, J.-J. Zhang, and G. Katsaros. Ge hole spin qubit. *ArXiv e-prints*, 2018.

[19] E. Kawakami, P. Scarlino, D. R. Ward, F. R. Braakman, D. E. Savage, M. G. Lagally, M. Friesen, S. N. Coppersmith, M. A. Eriksson, and L. M. K. Vandersypen. Electrical control of a long-lived spin qubit in a si/SiGe quantum dot. *Nature Nanotechnology*, **9** 666, 2014.

[20] K. Takeda, J. Kamioka, T. Otsuka, J. Yoneda, T. Nakajima, M. R. Delbecq, S. Amaha, G. Allison, T. Kodera, S. Oda, and S. Tarucha. A fault-tolerant addressable spin qubit in a natural silicon quantum dot. *Science Advances*, **2**, 2016.

[21] J. Yoneda, K. Takeda, T. Otsuka, T. Nakajima, M. R. Delbecq, G. Allison, T. Honda, T. Kodera, S. Oda, Y. Hoshi, N. Usami, K. M. Itoh, and S. Tarucha. A quantum-dot spin qubit with coherence limited by charge noise and fidelity higher than 99.9%. *Nature Nanotechnology*, **13** 102, 2018.

[22] A. G. Fowler, M. Mariantoni, J. M. Martinis, and A. N. Cleland. Surface codes: Towards practical large-scale quantum computation. *Phys. Rev. A*, **86** 032324, 2012.

[23] L. M. K. Vandersypen, H. Bluhm, J. S. Clarke, A. S. Dzurak, R. Ishihara, A. Morello, D. J. Reilly, L. R. Schreiber, and M. Veldhorst. Interfacing spin qubits in quantum dots and donors–hot, dense, and coherent. *npj Quantum Information*, **3** 34, 2017.

[24] M. Veldhorst, H. G. J. Eenink, C. H. Yang, and A. S. Dzurak. Silicon cmos architecture for a spin-based quantum computer. *Nature Communications*, **8** 1766, 2017.

[25] M. Veldhorst, J. C. C. Hwang, C. H. Yang, A. W. Leenstra, B. de Ronde, J. P. Dehollain, J. T. Muhonen, F. E. Hudson, K. M. Itoh, A. Morello, and A. S. Dzurak. An addressable quantum dot qubit with fault-tolerant control-fidelity. *Nature Nanotechnology*, **9** 981, 2014.

[26] M. Veldhorst, C. H. Yang, J. C. C. Hwang, W. Huang, J. P. Dehollain, J. T. Muhonen, S. Simmons, A. Laucht, F. E. Hudson, K. M. Itoh, A. Morello, and A. S. Dzurak. A two-qubit logic gate in silicon. *Nature*, **526** 410, 2015.

[27] D. M. Zajac, A. J. Sigillito, M. Russ, F. Borjans, J. M. Taylor, G. Burkard, and J. R. Petta. Resonantly driven cnot gate for electron spins. *Science*, 2017.

[28] T. F. Watson, S. G. J. Philips, E. Kawakami, D. R. Ward, P. Scarlino, M. Veldhorst, D. E. Savage, M. G. Lagally, M. Friesen, S. N. Coppersmith, M. A. Eriksson, and L. M. K. Vandersypen. A programmable two-qubit quantum processor in silicon. *Nature*, **555** 633, 2018.

[29] N. Samkharadze, G. Zheng, N. Kalhor, D. Brousse, A. Sammak, U. C. Mendes, A. Blais, G. Scappucci, and L. M. K. Vandersypen. Strong spin-photon coupling in silicon. *Science*, 2018.

[30] X. Mi, M. Benito, S. Putz, D. M. Zajac, J. M. Taylor, G. Burkard, and J. R. Petta. A coherent spin-photon interface in silicon. *Nature*, **555** 599, 2018.

[31] G. Burkard and A. Imamoglu. Ultra-long-distance interaction between spin qubits. *Phys. Rev. B*, **74** 041307, 2006.

[32] F. A. Zwanenburg, A. S. Dzurak, A. Morello, M. Y. Simmons, L. C. L. Hollenberg, G. Klimeck, S. Rogge, S. N. Coppersmith, and M. A. Eriksson. Silicon quantum electronics. *Rev. Mod. Phys.*, **85** 961, 2013.

[33] C. Morrison and M. Myronov. Strained germanium for applications in spintronics. *physica status solidi (a)*, **213** 2809, 2016.

[34] C. Testelin, F. Bernardot, B. Eble, and M. Chamarro. Hole–spin dephasing time associated with hyperfine interaction in quantum dots. *Phys. Rev. B*, **79** 195440, 2009.

[35] G. Katsaros, V. N. Golovach, P. Spathis, N. Ares, M. Stoffel, F. Fournel, O. G. Schmidt, L. I. Glazman, and S. De Franceschi. Observation of spin-selective tunneling in SiGe nanocrystals. *Phys. Rev. Lett.*, **107** 246601, 2011.

[36] N. Ares, G. Katsaros, V. N. Golovach, J. J. Zhang, A. Prager, L. I. Glazman, O. G. Schmidt, and S. D. Franceschi. SiGe quantum dots for fast hole spin rabi oscillations. *Applied Physics Letters*, **103** 263113, 2013.

[37] H. Watzinger, C. Kloeffel, L. Vukušić, M. D. Rossell, V. Sessi, J. Kukučka, R. Kirchschlager, E. Lausecker, A. Truhlar, M. Glaser, A. Rastelli, A. Fuhrer, D. Loss, and G. Katsaros. Heavy-hole states in germanium hut wires. *Nano Letters*, **16** 6879, 2016.

[38] W. Lu, J. Xiang, B. P. Timko, Y. Wu, and C. M. Lieber. One-dimensional hole gas in germanium/silicon nanowire heterostructures. *Proceedings of the National Academy of Sciences of the United States of America*, **102** 10046, 2005.

[39] D. Kotekar-Patil, B.-M. Nguyen, J. Yoo, S. A. Dayeh, and S. M. Frolov. Quasiballistic quantum transport through ge/si core/shell nanowires. *Nanotechnology*, **28** 385204, 2017.

[40] J. Xiang, A. Vidan, M. Tinkham, R. M. Westervelt, and C. M. Lieber. Ge/Si nanowire mesoscopic Josephson junctions. *Nature Nanotechnology*, **1** 208, 2006.

[41] Z. Su, A. Zarassi, B.-M. Nguyen, J. Yoo, S. A. Dayeh, and S. M. Frolov. High critical magnetic field superconducting contacts to Ge/Si core/shell nanowires. *arXiv preprint arXiv:1610.03010*, 2016.

[42] Y. Hu, F. Kuemmeth, C. M. Lieber, and C. M. Marcus. Hole spin relaxation in ge-si core-shell nanowire qubits. *Nature nanotechnology*, **7** 47, 2012.

[43] A. P. Higginbotham, T. W. Larsen, J. Yao, H. Yan, C. M. Lieber, C. M. Marcus, and F. Kuemmeth. Hole spin coherence in a Ge/Si heterostructure nanowire. *Nano Letters*, **14** 3582, 2014.

[44] R. Maurand, X. Jehl, D. Kotekar-Patil, A. Corna, H. Bohuslavskyi, R. Laviéville, L. Hutin, S. Barraud, M. Vinet, and S. De Franceschi. A cmos silicon spin qubit. *Nature Communications*, **7** 13575, 2016.

[45] F. Maier, J. Klinovaja, and D. Loss. Majorana fermions in Ge/Si hole nanowires. *Phys. Rev. B*, **90** 195421, 2014.

[46] C. Kloeffel, M. Trif, and D. Loss. Strong spin-orbit interaction and helical hole states in ge/si nanowires. *Phys. Rev. B*, **84** 195314, 2011.

[47] A. Y. Kitaev. Unpaired majorana fermions in quantum wires. *Physics-Uspekhi*, **44** 131, 2001.

[48] Y. Oreg, G. Refael, and F. von Oppen. Helical liquids and majorana bound states in quantum wires. *Phys. Rev. Lett.*, **105** 177002, 2010.

[49] R. Lutchyn, E. Bakkers, L. Kouwenhoven, P. Krogstrup, C. Marcus, and Y. Oreg. Realizing majorana zero modes in superconductor-semiconductor heterostructures. *arXiv preprint arXiv:1707.04899*, 2017.

[50] V. Mourik, K. Zuo, S. M. Frolov, S. R. Plissard, E. P. A. M. Bakkers, and L. P. Kouwenhoven. Signatures of majorana fermions in hybrid superconductor-semiconductor nanowire devices. *Science*, **336** 1003, 2012.

[51] X.-J. Hao, T. Tu, G. Cao, C. Zhou, H.-O. Li, G.-C. Guo, W. Y. Fung, Z. Ji, G.-P. Guo, and W. Lu. Strong and tunable spin-orbit coupling of one-dimensional holes in Ge/Si core/shell nanowires. *Nano letters*, **10** 2956, 2010.

[52] Q. Shi, Q. Ebner, and M. Zudov. Hall field-induced resistance oscillations in a p-type ge/SiGe quantum well. *Physical Review B*, **90** 161301, 2014.

[53] M. Failla, J. Keller, G. Scalari, C. Maissen, J. Faist, C. Reichl, W. Wegscheider, O. J. Newell, D. R. Leadley, M. Myronov, and J. Lloyd-Hughes. Terahertz quantum hall effect for spin-split heavy-hole gases in strained ge quantum wells. *New Journal of Physics*, **18** 113036, 2016.

[54] R. Mizokuchi, P. Torresani, R. Maurand, Z. Zeng, Y.-M. Niquet, M. Myronov, and S. D. Franceschi. Hole weak anti-localization in a strained-Ge surface quantum well. *Applied Physics Letters*, **111** 063102, 2017.

[55] T. M. Lu, C. T. Harris, S.-H. Huang, Y. Chuang, J.-Y. Li, and C. W. Liu. Effective g factor of low-density two-dimensional holes in a ge quantum well. *Applied Physics Letters*, **111** 102108, 2017.

[56] Y. Gul, S. N. Holmes, P. J. Newton, D. J. P. Ellis, C. Morrison, M. Pepper, C. H. W. Barnes, and M. Myronov. Quantum ballistic transport in strained epitaxial germanium. *Applied Physics Letters*, **111** 233512, 2017.

[57] Y. Gul, S. N. Holmes, M. Myronov, S. Kumar, and M. Pepper. Self-organised fractional quantisation in a hole quantum wire. *Journal of Physics: Condensed Matter*, **30** 09LT01, 2018.

[58] N. Hendrickx, D. Franke, A. Sammak, M. Kouwenhoven, D. Sabbagh, L. Yeoh, R. Li, M. Tagliaferri, M. Virgilio, G. Capellini, *et al.* Gate-controlled quantum dots and superconductivity in planar germanium. *arXiv preprint arXiv:1801.08869*, 2018.

[59] Y. Y. Peter and M. Cardona. *Fundamentals of semiconductors*. Springer, 2005.

[60] R. Winkler. *Spin-orbit Coupling Effects in Two-Dimensional Electron and Hole Systems*, vol. 191. Springer Science & Business Media, 2003.

[61] J. M. Luttinger and W. Kohn. Motion of electrons and holes in perturbed periodic fields. *Phys. Rev.*, **97** 869, 1955.

[62] L. C. L. Y. Voon and M. Willatzen. *The kp method: electronic properties of semiconductors*. Springer Science & Business Media, 2009.

[63] P.-O. Löwdin. A note on the quantum-mechanical perturbation theory. *The Journal of Chemical Physics*, **19** 1396, 1951.

[64] J. H. Prechtel, A. V. Kuhlmann, J. Houel, A. Ludwig, S. R. Valentin, A. D. Wieck, and R. J. Warburton. Decoupling a hole spin qubit from the nuclear spins. *Nature Materials*, **15** 981, 2016.

[65] R. J. Warburton. Single spins in self-assembled quantum dots. *Nature Materials*, **12** 483, 2013.

[66] J. M. Luttinger. Quantum theory of cyclotron resonance in semiconductors: General theory. *Phys. Rev.*, **102** 1030, 1956.

[67] A. Baldereschi and N. O. Lipari. Spherical model of shallow acceptor states in semiconductors. *Phys. Rev. B*, **8** 2697, 1973.

[68] D. S. Miserev, A. Srinivasan, O. A. Tkachenko, V. A. Tkachenko, I. Farrer, D. A. Ritchie, A. R. Hamilton, and O. P. Sushkov. Mechanisms for strong anisotropy of in-plane g-factors in hole based quantum point contacts. *Phys. Rev. Lett.*, **119** 116803, 2017.

[69] M. Shishkin, M. Marsman, and G. Kresse. Accurate quasiparticle spectra from self-consistent gw calculations with vertex corrections. *Phys. Rev. Lett.*, **99** 246403, 2007.

[70] E. Marcellina, A. R. Hamilton, R. Winkler, and D. Culcer. Spin-orbit interactions in inversion-asymmetric two-dimensional hole systems: A variational analysis. *Phys. Rev. B*, **95** 075305, 2017.

[71] B. Rössner, B. Batlogg, H. von Känel, D. Chrastina, and G. Isella. Hole band nonparabolicity and effective mass measurement in p-SiGe/ge heterostructures. *Materials Science in Semiconductor Processing*, **9** 777 , 2006.

[72] J. Foronda, C. Morrison, J. E. Halpin, S. D. Rhead, and M. Myronov. Weak antilocalization of high mobility holes in a strained germanium quantum well heterostructure. *Journal of Physics: Condensed Matter*, **27** 022201, 2015.

[73] M. O. Nestoklon, E. L. Ivchenko, J.-M. Jancu, and P. Voisin. Electric field effect on electron spin splitting in SiGe/Si quantum wells. *Phys. Rev. B*, **77** 155328, 2008.

[74] R. Winkler, H. Noh, E. Tutuc, and M. Shayegan. Anomalous giant rashba spin splitting in two-dimensional hole systems. *Physica E: Low-dimensional Systems and Nanostructures*, **12** 428 , 2002.

[75] R. Moriya, K. Sawano, Y. Hoshi, S. Masubuchi, Y. Shiraki, A. Wild, C. Neumann, G. Abstreiter, D. Bougeard, T. Koga, and T. Machida. Cubic rashba spin-orbit interaction of a two-dimensional hole gas in a strained-Ge/SiGe quantum well. *Phys. Rev. Lett.*, **113** 086601, 2014.

[76] R. Winkler, D. Culcer, S. J. Papadakis, B. Habib, and M. Shayegan. Spin orientation of holes in quantum wells. *Semiconductor Science and Technology*, **23** 114017, 2008.

[77] T. Wimbauer, K. Oettinger, A. L. Efros, B. K. Meyer, and H. Brugger. Zeeman splitting of the excitonic recombination in $In_xGa_{1-x}As$/GaAs single quantum wells. *Phys. Rev. B*, **50** 8889, 1994.

[78] N. Ares, V. N. Golovach, G. Katsaros, M. Stoffel, F. Fournel, L. I. Glazman, O. G. Schmidt, and S. De Franceschi. Nature of tunable hole g factors in quantum dots. *Phys. Rev. Lett.*, **110** 046602, 2013.

[79] M. E. Flatté and I. Tifrea. *Manipulating quantum coherence in solid state systems*, vol. 244. Springer Science & Business Media, 2007.

[80] T. Ihn. *Semiconductor Nanostructures: Quantum states and electronic transport*. Oxford University Press, 2010.

[81] M. O. Goerbig. Quantum hall effects. *arXiv preprint arXiv:0909.1998*, 2009.

[82] S. V. Iordanskii, Y. B. Lyanda-Geller, and G. E. Pikus. Weak localization in quantum wells with spin-orbit interaction. *ZhETF Pisma Redaktsiiu*, **60** 199, 1994.

[83] L. I. Glazman and A. V. Khaetskii. Nonlinear quantum conductance of a lateral microconstraint in a heterostructure. *EPL (Europhysics Letters)*, **9** 263, 1989.

[84] F. Nichele, S. Chesi, S. Hennel, A. Wittmann, C. Gerl, W. Wegscheider, D. Loss, T. Ihn, and K. Ensslin. Characterization of spin-orbit interactions of gaas heavy holes using a quantum point contact. *Phys. Rev. Lett.*, **113** 046801, 2014.

[85] L. P. Kouwenhoven, D. G. Austing, and S. Tarucha. Few-electron quantum dots. *Reports on Progress in Physics*, **64** 701, 2001.

[86] M. Myronov, A. Dobbie, V. A. Shah, X.-C. Liu, V. H. Nguyen, and D. R. Leadley. High Quality Strained Ge Epilayers on a Si0.2Ge0.8 / Ge / Si (100) Global Strain-Tuning Platform. *Electrochemical and Solid-State Letters*, **13** H388, 2010.

[87] A. Dobbie, M. Myronov, R. J. H. Morris, A. H. A. Hassan, M. J. Prest, V. A. Shah, E. H. C. Parker, T. E. Whall, and D. R. Leadley. Ultrahigh hole mobility exceeding one million in a strained germanium quantum well. *Applied Physics Letters*, **101** 172108, 2012.

[88] W. Knap, C. Skierbiszewski, A. Zduniak, E. Litwin-Staszewska, D. Bertho, F. Kobbi, J. L. Robert, G. E. Pikus, F. G. Pikus, S. V. Iordanskii, V. Mosser, K. Zekentes, and Y. B. Lyanda-Geller. Weak antilocalization and spin precession in quantum wells. *Phys. Rev. B*, **53** 3912, 1996.

[89] Y. M. Niquet, D. Rideau, C. Tavernier, H. Jaouen, and X. Blase. Onsite matrix elements of the tight-binding hamiltonian of a strained crystal: Application to silicon, germanium, and their alloys. *Phys. Rev. B*, **79** 245201, 2009.

[90] L. E. Golub and E. L. Ivchenko. Spin splitting in symmetrical SiGe quantum wells. *Phys. Rev. B*, **69** 115333, 2004.

[91] R. J. Elliott. Theory of the effect of spin-orbit coupling on magnetic resonance in some semiconductors. *Phys. Rev.*, **96** 266, 1954.

[92] Y. Yafet. Conduction electron spin relaxation in the superconducting state. *Physics Letters A*, **98** 287 , 1983.

[93] M. Dyakonov and V. Perel. Spin relaxation of conduction electrons in noncentrosymmetric semiconductors. *Soviet Physics Solid State, Ussr*, **13** 3023, 1972.

[94] C. Morrison, P. Wiśniewski, S. D. Rhead, J. Foronda, D. R. Leadley, and M. Myronov. Observation of Rashba zero-field spin splitting in a strained germanium 2D hole gas. *Applied Physics Letters*, **105** 182401, 2014.

[95] M. Failla, M. Myronov, C. Morrison, D. R. Leadley, and J. Lloyd-Hughes. Narrow heavy-hole cyclotron resonances split by the cubic rashba spin-orbit interaction in strained germanium quantum wells. *Phys. Rev. B*, **92** 045303, 2015.

[96] M. A. Zudov, O. A. Mironov, Q. A. Ebner, P. D. Martin, Q. Shi, and D. R. Leadley. Observation of microwave-induced resistance oscillations in a high-mobility two-dimensional hole gas in a strained Ge/SiGe quantum well. *Phys. Rev. B*, **89** 125401, 2014.

[97] D. Laroche, S.-H. Huang, Y. Chuang, J.-Y. Li, C. W. Liu, and T. M. Lu. Magneto-transport analysis of an ultra-low-density two-dimensional hole gas in an undoped strained Ge/SiGe heterostructure. *Applied Physics Letters*, **108** 233504, 2016.

[98] G. M. Minkov, A. V. Germanenko, O. E. Rut, A. A. Sherstobitov, L. E. Golub, B. N. Zvonkov, and M. Willander. Weak antilocalization in quantum wells in tilted magnetic fields. *Phys. Rev. B*, **70** 155323, 2004.

[99] V. I. Fal'ko. Longitudinal magnetoresistance of ultrathin films and two-dimensional electron layers. *Journal of Physics: Condensed Matter*, **2** 3797, 1990.

[100] J. S. Meyer, A. Altland, and B. L. Altshuler. Quantum transport in parallel magnetic fields: A realization of the berry-robnik symmetry phenomenon. *Phys. Rev. Lett.*, **89** 206601, 2002.

[101] D. M. Zumbühl, J. B. Miller, C. M. Marcus, K. Campman, and A. C. Gossard. Spin-orbit coupling, antilocalization, and parallel magnetic fields in quantum dots. *Phys. Rev. Lett.*, **89** 276803, 2002.

[102] S. Shibayama, K. Kato, M. Sakashita, W. Takeuchi, O. Nakatsuka, and S. Zaima. Improvement of Al2O3/Ge interfacial properties by O2-annealing. *Thin Solid Films*, **520** 3397 , 2012.

[103] M. Myronov, C. Morrison, J. Halpin, S. Rhead, C. Casteleiro, J. Foronda, V. A. Shah, and D. Leadley. An extremely high room

temperature mobility of two-dimensional holes in a strained ge quantum well heterostructure grown by reduced pressure chemical vapor deposition. *Japanese Journal of Applied Physics*, **53** 04EH02, 2014.

[104] M. Myronov, C. Morrison, J. Halpin, S. Rhead, J. Foronda, and D. Leadley. Revealing high room and low temperatures mobilities of 2D holes in a strained Ge quantum well heterostructures grown on a standard Si(001) substrate. *Solid-State Electronics*, **110** 35, 2015.

[105] C. Morrison, C. Casteleiro, D. R. Leadley, and M. Myronov. Complex quantum transport in a modulation doped strained ge quantum well heterostructure with a high mobility 2d hole gas. *Applied Physics Letters*, **109** 102103, 2016.

[106] T. Lu, C.-H. Lee, S.-H. Huang, D. Tsui, and C. Liu. Upper limit of two-dimensional electron density in enhancement-mode si/SiGe heterostructure field-effect transistors. *Applied Physics Letters*, **99** 153510, 2011.

[107] C.-T. Huang, J.-Y. Li, K. S. Chou, and J. C. Sturm. Screening of remote charge scattering sites from the oxide/silicon interface of strained si two-dimensional electron gases by an intermediate tunable shielding electron layer. *Applied Physics Letters*, **104** 243510, 2014.

[108] M. Büttiker. Quantized transmission of a saddle-point constriction. *Phys. Rev. B*, **41** 7906, 1990.

[109] B. J. van Wees, H. van Houten, C. W. J. Beenakker, J. G. Williamson, L. P. Kouwenhoven, D. van der Marel, and C. T. Foxon. Quantized conductance of point contacts in a two-dimensional electron gas. *Phys. Rev. Lett.*, **60** 848, 1988.

[110] K. J. Thomas, J. T. Nicholls, M. Y. Simmons, M. Pepper, D. R. Mace, and D. A. Ritchie. Possible spin polarization in a one-dimensional electron gas. *Phys. Rev. Lett.*, **77** 135, 1996.

[111] A. Kristensen, H. Bruus, A. E. Hansen, J. B. Jensen, P. E. Lindelof, C. J. Marckmann, J. Nygård, C. B. Sørensen, F. Beuscher, A. Forchel, and M. Michel. Bias and temperature dependence of the 0.7 conductance anomaly in quantum point contacts. *Phys. Rev. B*, **62** 10950, 2000.

[112] S. M. Cronenwett, H. J. Lynch, D. Goldhaber-Gordon, L. P. Kouwenhoven, C. M. Marcus, K. Hirose, N. S. Wingreen, and V. Umansky.

Low-temperature fate of the 0.7 structure in a point contact: A kondo-like correlated state in an open system. *Phys. Rev. Lett.*, **88** 226805, 2002.

[113] R. Danneau, O. Klochan, W. R. Clarke, L. H. Ho, A. P. Micolich, M. Y. Simmons, A. R. Hamilton, M. Pepper, and D. A. Ritchie. 0.7 structure and zero bias anomaly in ballistic hole quantum wires. *Phys. Rev. Lett.*, **100** 016403, 2008.

[114] Y. Komijani, M. Csontos, T. Ihn, K. Ensslin, Y. Meir, D. Reuter, and A. D. Wieck. Origins of conductance anomalies in a p-type gaas quantum point contact. *Phys. Rev. B*, **87** 245406, 2013.

[115] S. Heedt, W. Prost, J. Schubert, D. Grüzmacher, and T. Schäpers. Ballistic transport and exchange interaction in inas nanowire quantum point contacts. *Nano Letters*, **16** 3116, 2016.

[116] J. Saldaña, R. Žitko, J. Cleuziou, E. Lee, V. Zannier, D. Ercolani, L. Sorba, R. Aguado, and S. De Franceschi. Supercurrent through a spin-split quasi-ballistic point contact in an inas nanowire. *arXiv preprint arXiv:1801.01855*, 2018.

[117] A. P. Micolich and U. Zülicke. Tracking the energies of one-dimensional sub-band edges in quantum point contacts using dc conductance measurements. *Journal of Physics: Condensed Matter*, **23** 362201, 2011.

[118] M. J. Iqbal, R. Levy, E. J. Koop, J. B. Dekker, J. P. de Jong, J. H. M. van der Velde, D. Reuter, A. D. Wieck, R. Aguado, Y. Meir, and C. H. van der Wal. Odd and even kondo effects from emergent localization in quantum point contacts. *Nature*, **501** 79, 2013.

[119] F. Bauer, J. Heyder, E. Schubert, D. Borowsky, D. Taubert, B. Bruognolo, D. Schuh, W. Wegscheider, J. von Delft, and S. Ludwig. Microscopic origin of the '0.7-anomaly' in quantum point contacts. *Nature*, **501** 73, 2013.

[120] B. Brun, F. Martins, S. Faniel, B. Hackens, G. Bachelier, A. Cavanna, C. Ulysse, A. Ouerghi, U. Gennser, D. Mailly, S. Huant, V. Bayot, M. Sanquer, and H. Sellier. Wigner and kondo physics in quantum point contacts revealed by scanning gate microscopy. *Nature Communications*, **5** 4290, 2014.

[121] A. Iagallo, N. Paradiso, S. Roddaro, C. Reichl, W. Wegscheider, G. Biasiol, L. Sorba, F. Beltram, and S. Heun. Scanning gate imaging of quantum point contacts and the origin of the 0.7 anomaly. *Nano Research*, **8** 948, 2015.

[122] T. P. Martin, A. Szorkovszky, A. P. Micolich, A. R. Hamilton, C. A. Marlow, H. Linke, R. P. Taylor, and L. Samuelson. Enhanced zeeman splitting in ga0.25in0.75as quantum point contacts. *Applied Physics Letters*, **93** 012105, 2008.

[123] A. J. Daneshvar, C. J. B. Ford, A. R. Hamilton, M. Y. Simmons, M. Pepper, and D. A. Ritchie. Enhanced g factors of a one-dimensional hole gas with quantized conductance. *Phys. Rev. B*, **55** R13409, 1997.

[124] R. Danneau, O. Klochan, W. R. Clarke, L. H. Ho, A. P. Micolich, M. Y. Simmons, A. R. Hamilton, M. Pepper, D. A. Ritchie, and U. Zülicke. Zeeman splitting in ballistic hole quantum wires. *Phys. Rev. Lett.*, **97** 026403, 2006.

[125] A. Srinivasan, K. L. Hudson, D. Miserev, L. A. Yeoh, O. Klochan, K. Muraki, Y. Hirayama, O. P. Sushkov, and A. R. Hamilton. Electrical control of the sign of the g factor in a gaas hole quantum point contact. *Phys. Rev. B*, **94** 041406, 2016.

[126] C.-K. Wang and K.-F. Berggren. Spin splitting of subbands in quasi-one-dimensional electron quantum channels. *Phys. Rev. B*, **54** R14257, 1996.

[127] D. S. Miserev and O. P. Sushkov. Dimensional reduction of the luttinger hamiltonian and g-factors of holes in symmetric two-dimensional semiconductor heterostructures. *Phys. Rev. B*, **95** 085431, 2017.

[128] R. Mizokuchi, R. Maurand, F. Vigneau, M. Myronov, and S. De Franceschi. Ballistic one-dimensional holes with strong g-factor anisotropy in germanium. *ArXiv e-prints*, 2018.

[129] A. Laucht, R. Kalra, S. Simmons, J. P. Dehollain, J. T. Muhonen, F. A. Mohiyaddin, S. Freer, F. E. Hudson, K. M. Itoh, D. N. Jamieson, J. C. McCallum, A. S. Dzurak, and A. Morello. A dressed spin qubit in silicon. *Nature Nanotechnology*, **12** 61, 2016.

[130] K. De Greve, P. L. McMahon, D. Press, T. D. Ladd, D. Bisping, C. Schneider, M. Kamp, L. Worschech, S. Höfling, A. Forchel, and Y. Yamamoto. Ultrafast coherent control and suppressed nuclear feedback of a single quantum dot hole qubit. *Nature Physics*, **7** 872, 2011.

[131] L. Huthmacher, R. Stockill, E. Clarke, M. Hugues, C. L. Gall, *et al.* Coherence of a dynamically decoupled quantum-dot hole spin. *arXiv preprint arXiv:1711.09169*, 2017.

[132] S. J. Angus, A. J. Ferguson, A. S. Dzurak, and R. G. Clark. Gate-defined quantum dots in intrinsic silicon. *Nano Letters*, **7** 2051, 2007.

[133] G. de Lange, B. van Heck, A. Bruno, D. J. van Woerkom, A. Geresdi, S. R. Plissard, E. P. A. M. Bakkers, A. R. Akhmerov, and L. DiCarlo. Realization of microwave quantum circuits using hybrid superconducting-semiconducting nanowire josephson elements. *Phys. Rev. Lett.*, **115** 127002, 2015.

[134] L. Casparis, T. W. Larsen, M. S. Olsen, F. Kuemmeth, P. Krogstrup, J. Nygård, K. D. Petersson, and C. M. Marcus. Gatemon benchmarking and two-qubit operations. *Phys. Rev. Lett.*, **116** 150505, 2016.

[135] A. Crippa, R. Maurand, L. Bourdet, D. Kotekar-Patil, A. Amisse, X. Jehl, M. Sanquer, R. Laviéville, H. Bohuslavskyi, L. Hutin, *et al.* Electrical spin driving by g-matrix modulation in spin-orbit qubits. *arXiv preprint arXiv:1710.08690*, 2017.

[136] R. Li, F. E. Hudson, A. S. Dzurak, and A. R. Hamilton. Pauli spin blockade of heavy holes in a silicon double quantum dot. *Nano Letters*, **15** 7314, 2015.

[137] B. Voisin, R. Maurand, S. Barraud, M. Vinet, X. Jehl, M. Sanquer, J. Renard, and S. De Franceschi. Electrical control of g-factor in a few-hole silicon nanowire mosfet. *Nano Letters*, **16** 88, 2016.